Antennas, Wave Propagation, and Localization in Wireless Body Area Networks

Chandra, Rohit

2014

Citation for published version (APA):
Chandra, R. (2014). *Antennas, Wave Propagation, and Localization in Wireless Body Area Networks.* [Doctoral Thesis (compilation), Department of Electrical and Information Technology].

Total number of authors:
1

Antennas, Wave Propagation, and Localization in Wireless Body Area Networks

Doctoral Dissertation

Rohit Chandra

LUNDS
UNIVERSITET

Lund, Sweden
2014

Department of Electrical and Information Technology
Lund University
Box 118, SE-221 00 LUND
SWEDEN

This thesis is set in Computer Modern 10pt
with the LaTeX Documentation System

Series of licentiate and doctoral theses
ISSN 1654-790X; No. 59
ISBN 978-91-7473-855-1

Printed in Sweden by *Tryckeriet i E-huset*, Lund.
January 2014.

To My Parents

Popular Science Summary

Advancement in technology has made the fabrication of miniature electronic chips that consumes less power possible. These chips can be used for wireless connectivity. This has resulted in many small and compact wireless devices that are either implantable or wearable. Examples of wearable devices are hearing aids and the more recently developed Google Glass. The pacemaker is an example of an implantable device. A medical specialist may place wireless devices like a temperature sensor, a heart-rate monitor or a blood-pressure monitor on a patient to monitor his or her vital parameters. These devices collect the health parameters and may send them to a central unit also located on the body. The central unit may then send these data to the doctor's computer using Wi-Fi or Bluetooth. Such network of the communicating wireless devices that are implantable, wearable or in a close proximity of a body is called wireless body area network (WBAN). Athletes and sportsmen can also use the WBAN for monitoring their health parameters. The WBAN have the possibility to make the users' life comfortable by giving them freedom from wires and increasing their mobility.

As these devices are small, the space for the antenna is limited. An antenna is the part of the wireless device that receives and transmits a wireless signal. The wireless communication between the devices in the WBAN takes place either through the body as in the implants or over the body as for the wearable devices. This is different from the communication between a mobile phone and a base station where the communication channel is mostly through the air. When the communication channel is through the body or over the body, the signal loss is much higher than through the air. The reason for this is that the tissues of the human body absorb and attenuate the signal radiated by the antennas. A reliable wireless link between the devices in the WBAN can be designed by having knowledge of the signal loss in the communication channel, and the use of a proper antenna. Usually it is not possible to initially test the devices on an actual human due to ethical and safety issues. Hence, to calculate the signal loss or test the antenna, a phantom is used. A phantom could be a computer model of actual human or a physical phantom mimicking the tissues. This thesis present research work done for antennas and communication channels for various applications in the wireless body area network. Phantoms have been used for the investigation. The investigated applications are binaural hearing aids, sensors placed around the body, wireless capsule endoscopy, and in-mouth devices. These are explained below.

Binaural hearing aids are a system where there is a hearing aid in both of the ears. Such system helps a user in identifying the direction of sound. The binaural hearing aids communicate wirelessly with each other for functions like adjusting the volume or changing the settings for the listening environment. In this research, small antennas suitable in size and performance were designed for hearing aids. Further, a mathematical model of the signal loss for the wireless signal from the hearing aid in one ear to the hearing aid in the other ear was developed. The model can calculate the signal loss for different head sizes. The main advantage of the model is that it is faster in calculating the loss when compared to calculating it by using computer simulations.

A mathematical model for the signal loss between the sensors/devices placed around the torso was developed. The influence of the arms on the signal loss was also included in the model. It was found that there is a temporal variation in the signal level received by the devices placed around the torso when the arms swing while walking. Using this fact, we developed an approach to analyze the arm movements while walking using three wearable wireless devices. The variation in the received signal power was found symmetric for the receivers, one placed on the left side and the other on the right side of the torso for the normal swinging of the arms. The transmitter was placed at the central back position. An asymmetric power variation was found when the left arm and the right arm moved differently while walking. A high degree of asymmetric arm movements is an early sign of Parkinson's disease. Hence, the developed approach could be useful for such an analysis.

Endoscopy is a medical diagnosis method where the interior of the gastrointestinal tract which includes the stomach and the intestine, is inspected. In conventional endoscopy, a tube with a lens is inserted through the mouth or the rectum to observe the interior of the tract. However, it is uncomfortable and do not reach the entire small intestine. These problems of the conventional endoscopy can be overcome by using wireless capsule endoscopy. A wireless capsule endoscope is a swallowable pill like device with a camera and a transmitter. The camera captures the picture as it passes through the gastrointestinal tract. The transmitter sends the picture to the sensors located on the body. However, one of the major challenges associated with the wireless capsule is that the location of the capsule cannot be identified by viewing the picture alone. The knowledge of the location is important so that if some abnormality is observed, an operation can be performed at the correct location. We developed algorithms to find the location of the capsule.

Spinal cord or brain injury may result in movement disabilities. It can result in paraplegia where lower portions of the body are paralyzed. It may also results in more severe situation called quadriplegia where both torso and limbs are paralyzed. Such patients may have to depend upon someone else for moving their wheelchair or using a computer. Fortunately, the muscles above their neck like tongue are often healthy. The in-mouth device is a wireless device placed in the mouth of such patients. The device is controlled by the movement of the tongue. The signal transmitted by the device can then control the movements of the wheelchair having a receiver. In this research work, antennas suitable in performance and size for such devices were developed.

All research work presented in this thesis is done as a part of the project Wireless Communication for Ultra-portable devices. The project is supported by a grant from Swedish Foundation for Strategic Research (SSF).

Abstract

A network of communicating wireless devices that are implantable, wearable or within close proximity of a human body is called wireless body area network (WBAN). The propagation channels for the devices in the WBAN are either through the body or over the body. This results in the attenuation and the absorption of electromagnetic waves radiated by the antenna of these devices due to the lossy tissues of the body. With a proper antenna and knowledge of the signal loss between the devices in the WBAN, a reliable wireless link can be designed. This thesis presents the investigations done for the antennas, wave propagation, and localization for various applications of these networks. The investigated applications are: (1) Binaural Hearing Aids (Paper I & Paper II), (2) Sensor placed Around the Body (Paper III & Paper IV), (3) Localization of Wireless Capsule Endoscope (Paper V), and (4) In-Mouth Devices.

Binaural hearing aids communicate with each other for synchronization such as adjustment of volume or programing for the listening environment. In Paper I, antennas suitable in size and technical performance at 2.45 GHz for in-the-ear (ITE) and in-the-canal (ITC) placement of the hearing aids are presented. The ear-to-ear link loss found from the finite-difference-time-domain (FDTD) simulations for the ITE case was 48 dB and that for the ITC case was 92 dB for the SAM head. The ITE case was further investigated on realistic heterogeneous phantoms of different age and head sizes. The link loss in the ITE case for an adult heterogeneous phantom was found to be 79 dB. It was found that the absence of the pinna (outer ear) and the lossless shell underestimates the link loss for the SAM phantom. Hence, a phantom with the lossy outer shell and the pinnas should be used for a proper estimation of the ear-to-ear link loss. In Paper II, an analytical model is presented for the ear-to-ear link loss based on the attenuation of the creeping wave over an elliptically modeled cross-section of the head. The model takes into account the dominant paths having most of the power of the creeping wave from the antenna in one ear to the antenna in the other ear and the effect of the pinnas. Simulations were done to validate the model using the ITE placement of the antenna at 2.45 GHz on heterogeneous phantoms of different age-groups and head sizes, showing a good agreement with the model. The effect of the pinnas was verified through measurements on a phantom where the pinnas fabricated by 3D-printing were included.

In Paper III, an analytical model is developed for wireless propagation around the body based on the attenuation of creeping waves over an elliptical cross-section of the torso. The model includes the effect of the arms. It was verified through FDTD simulations on a numerical phantom with various arm positions. It was shown that it is critical to include the effect of the arms as their presence might result in extreme fading dips at some sensor positions. Further, a temporal variation in the power received by sensors placed around the torso was found when the arms moved while walking. This result is used in Paper IV to develop an approach to analyze the movements of the arms while walking using three wearable wireless devices. One of the devices is a transmitter placed at the back and the other two are symmetrically placed receivers at the side that record the power variation due to the arm movements. For such a placement of sensors, the variation in the receiver will be more or less symmetrical if the arm swing normally. However, a large degree of asymmetry in the arms swing will result in an asymmetrical variation in the received power by the two receivers. This was confirmed by simulations and measurements.

Wireless capsule endoscopy (WCE) overcomes the problems of conventional endoscopy like not reaching the entire small-intestine. However, due to the lossy tissues, the localization of the capsule is a challenging task which is required in order to know the position of an abnormality captured in the endoscopy image. Paper V presents a method for the localization of an in-body RF source, as in WCE, based on microwave imaging. The electrical properties of the tissues and their distribution were found from microwave imaging at 403.5 MHz. The method was applied on synthetic data obtained after addition of the white Gaussian noise to the simulated data of a simple circular phantom, and a realistic phantom for the 2D transverse magnetic polarization. The root-mean-square of the error distance between the various actual and estimated positions was found to be within 9 mm for both the phantoms showing the capability of the algorithm to localize the capsule in the presence of noise with a good accuracy.

An in-mouth device is a tongue controlled device used by the paraplegic or quadriplegic patients to control a wheelchair or type on a computer. Although the device is not surgically implanted but the performance of its antenna is influenced by the lossy tissues of the mouth or head in a similar way as that of an implant. In this work, antennas suitable in size and performance for such devices were investigated.

Preface

This thesis is a compilation of an introduction to the research field and a summary of my contributions, together with five research papers that present the main results achieved during my PhD study. The introduction part of the thesis also includes some simulation and measurement results which are not published or submitted to any journal or conference so far. The thesis extends the understanding in the field of antennas, wave propagation, and localization for the applications in the field of wireless body area networks. The investigated applications are binaural hearing aids, sensors placed around the body, wireless capsule endoscopy, and tongue controlled in-mouth devices. The included papers are:

[1] R. Chandra, and A. J Johansson, "Miniaturized antennas for link between binaural hearing aids," in *Proc. 32nd Annu. Int. Conf. of the IEEE Engg. in Med. and Biol. Soc.*, EMBC, pp. 688-691, Aug. 2010

[2] R. Chandra, and A. J Johansson, "A Link Loss Model for the On-Body Propagation Channel for Binaural Hearing Aids," *IEEE Trans. Antennas Propagat.*, vol. 61, no. 12, pp. 6180-6190, Dec. 2013

[3] R. Chandra, and A. J Johansson, "An Analytical Link-Loss Model for On-Body Propagation Around the Body Based on Elliptical Approximation of the Torso With Arms' Influence Included," *IEEE Antennas Wireless Propagat. Lett.*, vol. 12, pp. 528-531, 2013

[4] R. Chandra, and A. J Johansson, "An approach to analyze the movements of the arms while walking using wearable wireless devices," in *Proc. 35th Ann. Int. Conf. IEEE Engg. Med. Bio. Soc.*, EMBC, pp. 3431-3434, Jul. 2013

[5] R. Chandra, A. J Johansson, M. Gustafsson, and F. Tufvesson, "A Microwave Imaging based Technique to Localize an In-body RF-Source for Biomedical Applications," Submitted to *IEEE Trans. Biomed. Engg.*, 2014

During my PhD study, I have also contributed to the following publications which are not directly included in the thesis. However, parts of some of these publications are used in the thesis introduction.

[6] H. Sjoland, J.B Anderson, C. Bryant, R. Chandra, O. Edfors, A.J Johansson, N. S. Mazloum, R. Meraji, P. Nilsson, D. Radjen, J. N. Rodrigues, S. M. Y. Sherazi, and V. Owall, "A Receiver Architecture for Devices in Wireless Body Area Networks," *IEEE Jour. Emerging Sel. Top. Circ. Sys.*, vol. 2, no. 1, pp. 82-95, Mar. 2012

[7] E. E. Lopez, A. Garcia Lopez, R. Chandra, and A. J Johansson, "3D Printed Miniaturized UWB Antenna for Wireless Body Area Network," accepted for *8th Eur. Conf. Antennas Propagat.*, EUCAP, 2014

[8] R. Chandra, A. J Johansson, and Fredrik Tufvesson, "Localization of an RF source inside the Human body for Wireless Capsule Endoscopy," in *Proc. 8th Int. Conf. Body Area Net.*, pp. 48-54, 2013

[9] A. Garcia Lopez, E. E. Lopez, R. Chandra, and A. J Johansson, "Optimization and Fabrication by 3D Printing of a Volcano Smoke Antenna for UWB Applications," in *Proc. 7th Eur. Conf. Antennas Propagat.*, EUCAP, pp. 1471-1473, Apr. 2013

[10] R. Chandra, T. Abbas, and A. J Johansson, "Directional analysis of the on-body propagation channels considering human's anatomical variations," in *Proc. 7th Int. Conf. Body Area Net.*, BodyNets, pp. 120-123, Sept. 2012

[11] R. Chandra, and A. J Johansson, "Effect of frequency, body parts and surrounding on the on-body propagation channel around the torso," in *Proc. 34th Ann. Int. Conf. IEEE Engg. Med. Bio. Soc.*, pp. 4533-4536, Aug. 2012

[12] R. Chandra, and A. J Johansson, "An elliptical analytic link loss model for wireless propagation around the human torso," in *Proc. 6th Eur. Conf. Antennas Propagat.*, pp. 3121-3124, Mar. 2012

[13] R. Chandra, and A. J Johansson, "In-mouth antenna for tongue controlled wireless devices: Characteristics and link-loss," in *Proc. 33rd Ann. Int. Conf. IEEE Engg. Med. Bio. Soc.*, EMBC, pp. 5598-5601, Sept. 2011

[14] R. Chandra, and A. J Johansson, "Influence on the ear-to-ear link loss from heterogeneous head phantom variations," in *Proc. 5th European Conf. Antennas Propagat.*, EUCAP, pp. 1612-1615, Apr. 2011

Some research results during my PhD study have also been presented as temporary documents (TDs) in the European Cooperation in Science and Technology (COST) Action IC1004:

[15] R. Chandra, and A. J Johansson, “Analytical On-Body Propagation Models for the Channel around the Body based on Attenuation of Creeping Waves over an Elliptical Surface,” *Sixth Scientific Meeting of COST Action IC1004*, TD(13)06053, Malaga, Spain, Feb. 2013

[16] R. Chandra, and A. J Johansson, “Antennas and Propagation for the Ear-to-Ear Propagation Channel for Binaural Hearing Aids,” *First Scientific Meeting of COST Action IC1004*, TD(11)01027, Lund, Sweden, Jun. 2011

The research work presented in this thesis is a part of an interdisciplinary project, “Wireless Communication for Ultra-Portable Devices” done at Department of Electrical and Information Technology, Lund University. The project is funded by Stiftelsen för Strategisk Forskning (SSF), Sweden.

Acknowledgements

Seldom anything is achieved without help, support, guidance, encouragement, love and care of other people. I am fortunate to have such people around me who have made my journey during my doctoral studies fruitful, rewarding and enjoyable.

First and foremost, I express my deepest gratitude to my supervisor Dr. Anders J Johansson, for accepting me as his PhD student, and giving me all support and guidance I needed during my study. I particularly admire his scientific way of thinking and providing new ideas. I am also grateful to my other supervisor, Dr. Fredrik Tufvesson, who is always encouraging, ready for discussions and for teaching me Channel Modeling. My sincere thanks go to Dr. Mats Gustafsson for a very fruitful collaboration in one of the projects. I am also thankful to Dr. Ove Edfors for teaching me Radio Systems and Linear Algebra for Wireless Communication. His enthusiasm for teaching and clearing any doubts is really appreciable. Many thanks are due to Dr. Buon Kiong Lau for teaching me MIMO and helping me whenever I needed help. I am also thankful to Dr. Henrik Sjöland for all the support he provided me as the project leader of the Ultra Portable Devices (UPD) for Wireless Communication of which I am a project member. I also thank Dr. Daniel Sjöberg who has always helped me whenever I approached him with some doubts in Electromagnetic theory. I thank Dr. Viktor Öwall who being the head of department has helped me in many administrative matters.

I express my gratitude to Dr. Koichi Ito for providing me opportunity to use his lab facilities at Chiba University, Japan, for performing measurements, and Ho-Yu Lin and Chia-Hsien Lin for helping me in the measurements. Thanks also go to Dr. Ronan Sauleau and Dr. Maxim Zhadobov for hosting me at IETR, Rennes, France.

I am especially grateful to my colleagues in Radio Systems group for providing a pleasant work-environment, Taimoor for being a nice friend and office-mate for almost four years, Meifang for Chinese food and cookies, Carl for attempting (unsuccessfully) to teach me pronunciation of *sju*, and *cat-talks*, Xiang for coming to my office looking for cookies and returning back disappointed (mostly), Pepe for sharing vast knowledge and experience, Ghassan for Yemeni desserts, Nafiseh for fresh Persian almonds and walnuts, Saeedeh for *gol gav zuban*, Dimitrios for his computer skills, Atif, Muris, and João for giving me company when I was working late. Special thanks are also due to two former group colleagues, Dr. Peter Hammarberg and Dr. Palmi Thor Thorbergsson.

I am thankful to Carl Bryant, Dejan, Nafiseh, Reza and Yasser for being good project members. I extend my sincere gratitude to Iman, Atif, and Taimoor for helping me with measurements, and technical discussions; Dr. Ruiyuan Tian and Marius for technical discourse and fruitful collaboration in teaching Antenna Technology labs; Carl G., Zach, Ivaylo and Atif for proofreading parts of the thesis. I thank all colleagues, present and former, at the department for providing a pleasant environment, and friendly conversations during *fika* and lunch. I am privileged to have friendly discourse with all and won't be naming all in fear of missing out anyone but my gratitude extends to all of you.

Thanks to all the administrative and finance staffs of the department and especially to Pia for guiding me whenever I was lost. I thank Lars, Martin, Josef, and Robert for technical support.

I would like to thank Swedish Foundation for Strategic Research (SSF) for funding the UPD project which made my stay in Sweden financially possible.

Special thanks go to two Indian families in Lund who have never let me miss Indian food and included me as their family member. Thanks a bunch, Rimpu-Namita and Sandeep-Shikha (and little Goral). I am also thankful to all my other Indian friends in Lund/Malmö for the Indian hangouts and festival celebrations. I thank all my IIT Roorkee friends especially the *DuDeS* who have always encouraged me and were ready to have Google hangouts, and Amit for proofreading part of my thesis. Thanks to Josie, Robina, and Marta for being my beginning friends in Lund, and to housemate Francesca for providing pleasant environment at home, to good friends Eglė and Vidmantas for encouragement, *fika* and activities. Thanks to all my friends who, one or the other way, have helped me during my PhD journey.

Thanks to all my family members for support, encouragement, love, and care. A special mention is necessary for my sister Shilpi *di* and her husband Arvind *jijaji*. Last, but not least, I woudn't have made till here without endless care, love, encouragement and sacrifices of my father, Dr. Umesh Chandra and my mother, Smt. Sushma Chandra. Thank you *Maa* and *Papa*.

Rohit Chandra
Lund, 3rd February, 2014

List of Acronyms and Abbreviations

2D Two Dimension

3D Three Dimension

AOA Angle-of-Arrival

ASIC Application Specific Integrated Circuit

BAN Body Area Network

BER Bit Error Rate

BSN Body Sensor Network

BTE Behind-the-Ear

BW Bandwidth

CAD Computer Aided Design

CIC Completely-In-Canal

CT Computed Tomography

ECG Electrocardiography

EEG Electroencephalography

EIRP Effective Isotropic Radiate Power

EM Electromagnetic

ETSI European Telecommunication Standards Institute

FCC Federal Communications Commission

FDTD Finite-Difference-Time-Domain

GI Gastro-Intestinal

HBC Human Body Communication

IEEE Institute of Electrical and Electronics Engineers

ISM Industrial Scientific Medical

ITC In-the-Canal

ITE In-the-Ear

LL Link Loss

LOS Line-of-Sight

MBAN Medical Body Area Network

MEDS Medical Data Service

MICS Medical Implant Communication Service

MPC Multi-Path Component

MRI Magnetic Resonance Imaging

MedRadio Medical Device Radio communications Service

NB Narrow Band

NFMI Near Field Magnetic Induction

NLOS Non Line-of-Sight

PEC Perfect Electric Conductor

PHY Physical Layer

RF Radio Frequency

RFID Radio Frequency Identification

RMS Root Mean Square

RMSE Root Mean Square Error

RSSI Received Signal Strength Indicator

RX/Rx Receiver

SAM Standard Anthropomorphic Model

SAR Specific Absorption Rate

SAW Surface Acoustic Wave

SMA Sub-Miniature version A

SNR Signal-to-Noise Ratio

TM Transverse Magentic

TOSM Through Open Short Match

TX/Tx Transmitter

UHF Ultra High Frequency

UPML Uniaxial Perfectly Matched Layer

UWB Ultra-Wide Band

VNA Vector Network Analyzer

WBAN Wireless Body Area Network

WCE Wireless Capsule Endoscopy

WMTS Wireless Medical Telemetry Service

WPAN Wireless Personal Area Network

Contents

Part I

Overview of the Research Field

Chapter 1

Wireless Body Area Network

1.1 Introduction

Advancements in the integrated circuit technology, resulting in miniaturization of the electronics and use of the ultra-low power wireless technology, have enabled many compact wireless devices or sensors which are wearable or implantable. Smart watches, hearing aids, body temperature sensors, and more recently announced Google Glass are such compact ultra-low power wearable devices. Pacemakers, retinal prosthesis, and cochlear implants are examples of the implantable devices. As these examples suggest, the users of these devices are both patients as well as healthy people. These devices have made the life of patients comfortable by increasing their mobility. Moreover, as the world population is aging as presented in the UN report [1], there is a growing need for constant monitoring of the health of elderly people. Hence, these devices and sensors are increasingly being used for such purpose [2], [3]. Additionally, sportsmen and athletes monitor their vital health parameters like blood pressure, temperature etc. using wearable devices [4]. Two or more such devices close to the body or implanted may communicate with each other, or with a central control unit, forming together a network called a wireless body area network (WBAN). Some other terms which are commonly used for the WBAN are body sensor network (BSN) or body-centric wireless communication. The focus of the research field discussed in the thesis is antennas, wave propagation and localization for the devices in various applications of the WBAN. In many applications of body centric communication such as in a pacemaker, the battery should last the device life time, making the ultra-low power consumption a necessity [5]. As these devices are either close to the human body or implanted inside the body, the overall size of the device including the size of the antenna should be small. Moreover, the power of the electromagnetic (EM) waves radiated by these devices should be within a safe level. Further, the communication between these devices takes place through the body or over the body and hence the propagation channel needs to be investigated and the signal loss has to be estimated. The lossy and heterogeneous tissues of the human body also makes the localization of an implanted RF-source a challenging task. Localization of an implanted RF-source is needed in applications like wireless capsule endoscopy. Therefore, antennas, wave propagation, and localization plays a critical role for the devices in the WBANs.

1.2 Wireless Body Area Networks

A Wireless Body Area Network (WBAN) consists of several wireless nodes or sensors located on the body and/or implanted which may communicate with each other and/or with an external base-station. The WBAN evolved from the Wireless Personal Area Network (WPAN) with the need for the communication between the devices located on the body or within its immediate proximity. Though the typical communication range of the devices in the WBAN is within a meter, an internet or a cellular network connection can be used as a gateway to connect various networks with the WBAN [6]. For example, sensors for recording vital signs of a heart patient can alert the hospital or a doctor through internet or a cellular network by measuring the changes in the vital sign about a possible heart attack. Fig. 1.1 shows some of the typical devices/sensors in a WBAN system.

As mentioned earlier, the WBAN technology can be used for both medical as well as non-medical applications. Some of the non-medical applications of the WBAN include video sharing, data file transfer, sports, monitoring and tracking, and entertainment applications as in gaming and social networking [7].

1.2.1 Scenarios

WBAN applications can be divided into different scenarios depending on the communication needs and requirements. These can be classified as: (1) on-body to off-body (2) on-body to on-body (3) in-body to on-body and/or off-body (4) body to body. Each of these scenarios uses a different channel and have a different set of requirements for the antenna, the transmitted power and other communication parameters of the device [8]. For example, for the on-body to

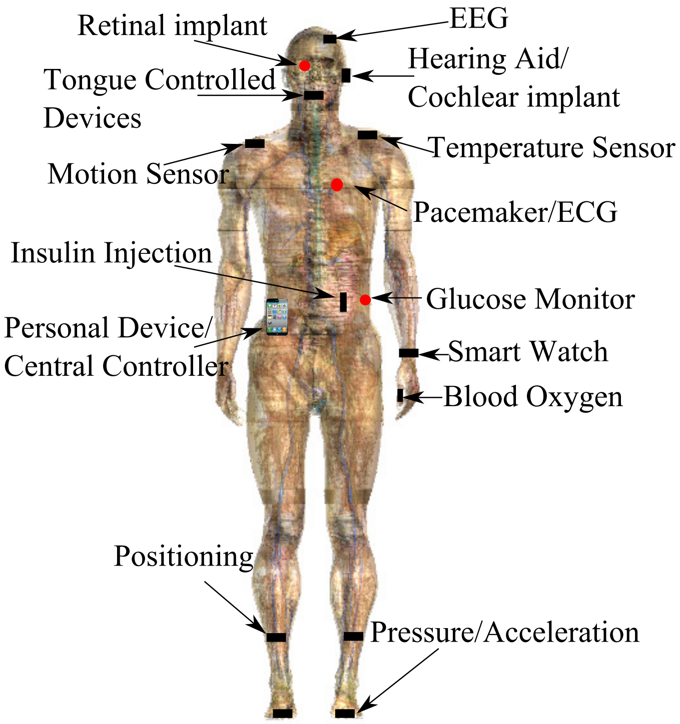

Figure 1.1: Typical devices in Wireless Body Area Network [5]. A rectangle represent an on-body/wearable device and a circle represent an implantable device.

on-body case, the devices communicating with each other are located on the body and hence uses an on-body channel which have higher attenuation than on-body to off-body scenarios where the propagation channel is mainly in free space. These scenarios are described in the following sections.

On-Body to Off-Body

These scenarios consist of the wearable sensors communicating to external devices and vice-versa as shown in Fig. 1.2. These are similar to a cellular phone network where the mobile stations located in the immediate proximity of the humans communicate with the base station. A typical WBAN use-case would be a scenario where a patient is lying on a hospital bed monitored by the wearable sensors. These sensors send the data to an external computer placed in the same room through a wireless link. The data could be then analyzed in a real time or later by a specialist.

An antenna for on-body to off-body WBAN scenarios should radiate away from the body. It should not radiate towards the body or along the body. Fabric based antennas or textile antennas discussed in [9]-[11] have been developed for such purposes. Since, the WBAN devices usually communicate with the external devices in a hospital room, the communication channel for these scenarios is a typical indoor communication channel.

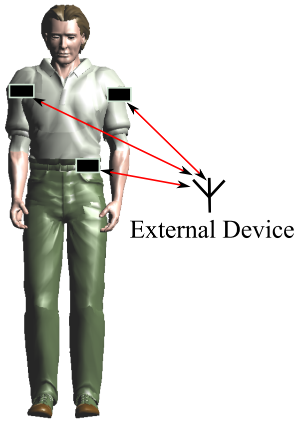

Figure 1.2: On-Body to Off-Body Scenario

On-Body to On-Body

In on-body to on-body scenarios, the body-worn devices placed at different locations around the body or along the body communicate with each other as shown in Fig. 1.3. A hearing aid placed in each of the ears in a binaural system, communicating with each other is another example of such a scenario [12]. Additional example is that of a glucose sensor and an insulin pump placed at the waist, where the glucose sensor senses the level of the insulin and communicates wirelessly to the pump which inject the insulin as in the Meditronic continuous glucose monitoring system [13].

General requirements for the on-body communication devices is that they should be small and lightweight, and consumes low power [8]. Some of the on-body devices may also require support for a high data rate. The on-body to on-body communication uses the body surface as the communication channel which has higher attenuation than free space for the same communication distance. The attenuation is even higher for the devices located on the opposite side of the body as in the binaural hearing aids system [5], [12]. Hence, a good understanding of the propagation mechanism and the attenuation of electromagnetic waves on the body surface is a requirement for the design of a reliable link. Many papers have shown that the creeping wave phenomenon is the mechanism for the wave propagation around the body surface [14]-[19]. In terms of the antenna requirement, it is shown that the antenna should be perpendicularly polarized with respect to the body for low attenuation [19]. Moreover, the antenna should radiate along the body surface and radiation away or towards the body should be minimum [19], [20]. The on-body to on-

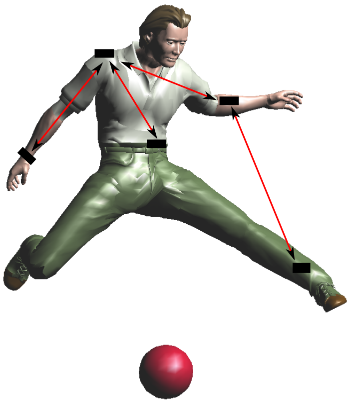

Figure 1.3: On-Body to On-Body Scenario

body scenarios may also involve a link through free space as between a device located on the hand and another on the foot (see Fig. 1.3).

In-Body to On-Body and/or Off-Body

Miniaturization of the electronic circuits has made the possibility of many devices to be implanted inside the body. Two of the most successful implant devices are heart pacemakers, and cochlear implants. Many new possibilities for the implants are also being researched and developed, e.g., retinal prosthesis [21], [22]. Apart from implanting, there is also a possibility of placing devices inside the body which are not technically implanted but swallowed as in wireless capsule endoscopy (WCE) [23], or placed in-mouth as in tongue controlled devices for quadriplegic patients [24], [25]. Once the devices are placed inside the body, different operating parameters of the implant may have to be changed or the diagnostic data has to be read out using external devices. These external devices may be located on the body as in the WCE for receiving the images from within the body, transmitted by the capsule. Such a scenario is an example of in-body to on-body communication system. In some cases, the implant could receive/transmit data from an external device not located on the body. An example could be of a pacemaker that transmits the data to an external receiver. Such a scenario is an example of an in-body to off-body communication as shown in Fig. 1.4.

The communication channel for the in-body to on/off-body scenarios in-

Figure 1.4: In-Body to On/Off Body Scenario where the circle represents an implant and the rectangle an on-body device.

Figure 1.5: Body to Body Scenario

cludes the body as a communication medium. The human body consists of lossy tissues and hence for in-body to on/off-body systems, the attenuation might be higher than on-body to on-body for some cases at the same frequency. Moreover, for the implants the power consumption should be ultra-low as changing the battery may require an operation. The implant devices should be very small and compact which places a stringent requirement on the size of the antenna. Further, the antenna should be optimized for its performance as it is surrounded by a lossy medium.

Body to Body

The body to body scenarios are similar to those of the body to off-body scenarios, except that the communication takes between the wearable or implanted devices on different people as shown in Fig. 1.5 and discussed in [26]-[28]. An example of this scenario is a case when a person meets another person and their business card is exchanged through their on-body devices. The human body itself is the shadowing object for such communication when the person walks away from the other person [26]. Hence, a proper characterization of the channel is must for the design of a reliable link.

1.2.2 WBAN Frequency Bands

The operational frequency band for the WBANs should be chosen properly taking into the account several factors like the desirable application, the antenna size, and the attenuation to name few. A low frequency band has low attenuation of the signal but at the same time has relatively large antenna size. Moreover, the available bandwidth is low resulting in a lower data rate. A choice of a high frequency band will result in small antenna size and high bandwidth but on the downside, it will have high attenuation. Generally, in the WBAN applications the devices are compact and small, resulting in a limited size for the antenna. So at low frequencies the antenna becomes an inefficient radiator, and at high frequency tissue absorption losses dominate [5]. For on-body devices, 2.45 GHz ISM band is a suitable option as it offers a good trade-off between these aspects. Further, it offers 80 MHz of license-free bandwidth worldwide [5]. For the implants the $402-405$ MHz is one of the suitable bands as the attenuation in the tissues is low and the size of the antenna is small because of the high permittivity of the medium in which it is implanted [29]. The analytical expression for the attenuation of the EM wave in the tissue is shown in (1.10) and that for the wavelength in the medium in (1.1). Other frequency bands for which the applications of the WBAN are being developed or researched are $3.1-10.6$ GHz ultra-wideband (UWB) due to inherit benefits of the UWB band such as security, low interference, and high data rate [30]-[33], and 60 GHz due to high security and large bandwidth [34]-[37].

1.2.3 WBAN Communication Standards

There exists many communication standards which are being used for different scenarios of the WBAN discussed in the previous sections. Some of these standards have particular frequency band suitable for a particular type of scenario. As discussed in Section 1.2.2, the use of high frequency for implants would result in high attenuation due to the tissue absorption. Hence, a standard with low frequency band is desirable. This section discusses the communication standards being currently used for the different WBANs.

Medical Implant Communication Service (MICS)

The Medical Implant Communication Service (MICS) is a standard established by the Federal Communications Commission (FCC) [38] in 1999 for communication with medical implants. However, now it is incorporated within MedRadio spectrum by the FCC. In Europe, the MICS standard is still followed and is standardized by the European Telecommunications Standards Institute (ETSI) [39] in [40]. The ETSI standard lists the two principle use of the MICS: (a) communication between an implant and an external device and (b) communication between different implants within the same body. The frequency band for the MICS is $402-405$ MHz with the maximum emission bandwidth to be occupied is 300 kHz. This maximum bandwidth is for the complete session i.e. including both the up-link and the down-link bandwidth. Thus, to achieve the maximum data rate within the MICS band, a half-duplex solution is recommended [29]. Moreover, the 300 kHz bandwidth is an emission limit i.e. the power at the band edges has to be 20 dB below the maximum level of the modulated power. The maximum transmit power is 25 μW Equivalent Isotropic Radiated Power (EIRP).

Medical Device Radio communications Service (MedRadio)

In 2009, the Federal Communications Commission (FCC), created the Medical Device Radio communications Service (MedRadio) in $401-406$ MHz range to be used for diagnostic and therapeutic purposes in implanted medical devices as well as devices worn on a body [41]. Other frequency bands used for MedRadio are $413-419$ MHz, $426-432$ MHz, $438-444$ MHz, and $451-457$ MHz. The MedRadio band is licensed by rule that means an individual license is not required to operate the MedRadio Device. Moreover, the FCC states the rule regarding the eligibility for operating the MedRadio Device. Only authorized health care providers, and manufacturer of the MedRadio devices and their representatives are authorized to operate such devices. Further, the MedRadio devices are authorized on a secondary status and must not cause harmful interference to devices that are authorized on a primary basis. They should accept interference from the devices authorized on a primary basis [42].

It should be noted that the creation of the $401-406$ MHz MedRadio Service incorporated the MICS spectrum of $402-405$ MHz created by the FCC and rules have not been changed for this MICS band. The additional band is used for the body-worn devices which was not the case for the MICS band as it was exclusively used for the implant communication. The ETSI still uses the term MICS and the additional $401-402$ MHz and $405-406$ MHz band is petitioned as Medical Data Service (MEDS) in U.S.A. [43]. The authorized bandwidth for the different MedRadio bands are: 100 kHz for $401-401.85$ MHz, 150 kHz for $401.85-402$ MHz, 300 kHz for $402-405$ MHz, 100 kHz for $405-406$ MHz, and 6 MHz for all other bands.

Wireless Medical Telemetry Service (WMTS)

The Wireless Medical Telemetry Service is used for remote monitoring of a patient's health. These devices measure the patient's vital signs and other health parameters, and transmit the data via radio link to a remote location, as to a healthcare person. For example, the wireless cardiac monitors which may be used to monitor a patient following surgery can use the WMTS standard. The frequency band assigned by the FCC are $608-614$ MHz, $1395-1400$ MHz, and 1427 – 1432 MHz. It should be noted that this standard is only used in USA. The FCC service rules for the WMTS are defined in [44]. Similar to the MedRadio band, only authorized health care providers are eligible to operate the WMTS device and that only within a health care facility. Further, the WMTS devices that operate within 20 cm of the user's body has to demonstrate compliance with the FCC's radio-frequency (RF) radiation exposure guidelines [45].

IEEE 802.15.6 Standard

The IEEE 802 approved a task group called IEEE 802.15.6 in December 2007 for the standardization of the WBAN. The purpose of this task group was to define new physical (PHY) and medium access control (MAC) layers for the WBAN [7]. Three PHY layers, Narrowband (NB), Ultra-Wideband (UWB) and Human Body Communication (HBC) have been defined, whose selection depends upon the WBAN application requirements. On the top of the PHY, MAC layer is defined to control the channel. The NB PHY uses either of the following bands: 402 – 405 MHz (MICS), 420 – 450 MHz, 863 – 870 MHz, 902 – 928 MHz, 950 – 956 MHz, 2360 – 2400 MHz, and 2400 – 2483.5 MHz (the 2.45 GHz industrial, scientific and medical, ISM, radio band). The standard also defines the type of the data packet component, the modulation scheme, the symbol rate, the code rate, and the information data rate for each of the bands [46]. The UWB PHY operates in low band and high band divided into channels of 499.2 MHz bandwidth each. The low band UWB PHY has three channels with mandatory channel number two with the central frequency of 3993.6 MHz and high band has 8 channels (Channel number 4 to 11) with the mandatory 7th channel with the central frequency of 7987.2 MHz. A UWB WBAN device should support at least one of the two mandatory channels. The UWB WBAN can be used for the application requiring high data rate which may go up to 10 Mbps. The third PHY layer, HBC operates at much lower frequency bands centered at 16 MHz and 27 MHz with the bandwidth of 4 MHz.

1.2.4 Medical Body Area Network

FCC finalized the rules for Medical Body Area Networks (MBANs) which are effective from October, 2012 [47]. A MBAN is a network of multiple body-worn wireless transmitters that measures and transmits physiological parameters or perform therapeutic functions. FCC approved 2360 – 2400 MHz frequency band dedicated for these networks on a secondary basis. As part of the MBAN spectrum is already used for other purposes like flight testing, an MBAN device should operate only over relatively short distances with low power to co-exist in the spectrum with minimal interference. Many rules that are applicable for body-worn devices in the Medradio band is also applicable for MBAN devices. For example, similar to the MedRadio band, the MBAN band is licensed by rule and only authorized health care professional, manufacturer or their representative, can operate an MBAN device. An MBAN device can be used both indoors and outdoors, however, for the indoor use $2360 - 2390$ MHz band should be used. Maximum of 5 MHz bandwidth is specified for an MBAN device. Furthermore, an MBAN device is limited to transmit maximum 1 mW EIRP measured in a 1 MHz bandwidth in the $2360 - 2390$ MHz and maximum 20 mW EIRP measured in a 5 MHz bandwidth in the $2390 - 2400$ MHz band.

1.3 Antennas and Propagation for WBAN

1.3.1 Antennas

On-body Antenna

An on-body antenna is part of wireless wearable devices used for various non-invasive applications. In [48], we presented antennas for hearing aids in a binaural system where the communication takes place through the waves creeping over the head surface. In [9], an on-body textile antenna for firefighters has been presented for 2.45 GHz ISM band. A textile antenna array for emerging millimeter wave body centric communication is presented in [36]. Textile antennas use fabric similar to cloth and hence could be ‘hidden’ inside it. This makes such antennas cosmetically appealing as they preserve the users’ integrity. Apart from being compact and cosmetically appealing, the on-body antennas are required to have proper radiation pattern and polarization. In [19], an on-body antenna for body surface communication is presented. It is discussed that if an antenna is for the on-body to on-body communication, the off-body and in-body radiation from the antenna should be minimized, and it should radiate along the body surface. The reason for this is that the on-body to on-body communication takes place through the EM waves which travel over the body surface. Further, for such applications, the polarization of the antenna should be perpendicular w.r.t. the body surface, as the perpendicular component of the electric field attenuates lesser than the tangential component for EM waves traveling over the body surface [17]. A more detailed discussion regarding the attenuation of perpendicular and tangential components of the field is done in Section 1.3.3.

Implant Antenna

The definition of the antenna in an implanted device communicating with an external device is not just limited to the radiating or the receiving part of the device. In free space, the basic definition of the extent of the antenna would just include the radiating or the receiving part of the device. However, in an implant case, the characteristics of the antenna are influenced by the surrounding tissues, the place of implant, body shape and size, and the implant itself [8], [29]. Hence, characteristics of an implant antenna can be defined as the sum of the characteristics of the antenna, implant, and the body. Thus, the extent of the antenna is not just limited to the antenna itself rather it includes the complete body. In [49], design, simulation, and characterization of low profile implanted antennas like a spiral micro-strip antenna and a planar inverted-F antenna for the MICS band is presented. A dual band (MedRadio and 2.45 GHz ISM) miniature conformal antenna for implantable telemetry applications is presented in [50]. A review of various implanted patch antennas is presented in [51]. A compact folded dipole antenna operating in the $0.951-0.956$ GHz ultra-high frequency band (UHF) and to be used for implanting in the arm is presented in [52].

The size of an antenna depends upon the frequency of operation or the wavelength. Usually, the size of the antenna is inversely proportional to the frequency (or directly proportional to the wavelength of the operation). The high permittivity of the body tissues has an advantage in reducing the size of the antenna as the wavelength is shorter in a medium with high relative permittivity. The wavelength in a medium is given by:

$$\lambda_{medium} = \frac{\lambda_{free\_space}}{\mathrm{Re}\left[\sqrt{\varepsilon_r - j\frac{\sigma_e}{\omega\varepsilon_0}}\right]}, \tag{1.1}$$

where λ_{free_space} is the wavelength in the free space, ε_r is the relative permittivity of the medium, σ_e is the conductivity of the medium, $\omega = 2\pi f$, f being the frequency, and ε_0 is the permittivity of the free space. For example, at the central frequency of the MICS band, i.e. 403.5 MHz, the free space wavelength is 74.30 cm. However, in muscle tissue with an $\varepsilon_r = 57.1$ and $\sigma_e = 0.8$ S/m (see Table 1.1), the wavelength is 9.42 cm which is an 87% reduction in the wavelength compared to the free space.

Another effect that a medium has is that it will influence the near-field of the antenna, as well as the wave propagation. Usually, the implanted antenna is inside a lossless insulation for reducing the losses in the near-field [53]. Here, the theory of the antenna inside a lossy medium as discussed in [29], [54] is outlined. The lossless insulation is assumed to be a sphere (for mathematical simplicity) of volume V and radius a. Outside this sphere the electric field is expressed as [54]:

$$\vec{E}((\vec{r})) = \sum_{l=1}^{\infty} \sum_{m=0}^{l} \sum_{\tau=1}^{2} a_{\tau ml(even)} \vec{u}_{\tau ml(even)}(\vec{r}) + a_{\tau ml}(odd) \vec{u}_{\tau ml(odd)}(\vec{r}), \quad (1.2)$$

where every term in the sum is an outwardly propagating spherical wave, called a partial wave $\vec{u}_{\tau ml}(\vec{r})$ with amplitudes $a_{\tau ml}$. Any suitable radiation pattern can be obtained by a suitable set of $a_{\tau ml}$ achieved by designing the currents in the volume V. The angular variation of the field depends on the l-value. For an antenna with a maximum index l_{max}, the directivity D is bounded by [54]

$$D \leq l_{max}(l_{max} + 2) \quad (1.3)$$

which implies that for a high directivity antenna l-value should be large. However, the near field grows rapidly with l, resulting in high magnetic and electric field stored in the near-zone. This stored energy is linked to reactive power flow in a free space which does not contribute to the radiating power from the antenna. The result of this is large non-radiating current which dissipates as heat due to ohmic loss in the antenna. However, in a lossy medium the reactive fields are not purely reactive due to the complex wavenumber k and will lose energy in the near field of the antenna also as an ohmic loss. Hence, in a lossy medium the power accepted by an antenna is given as [29]:

$$P_{accepted} = P_{ohm} + P_{near\_field} + P_0 e^{-2\mathrm{Im}(ka)}. \quad (1.4)$$

The radiated power $P_0 e^{-2\mathrm{Im}(ka)}$ is independent of l-value whereas the other two term increases with it. Hence, for an antenna in a lossy medium, l-value should be as low as possible for a higher radiation efficiency as the efficiency of any antenna is defined as:

$$\eta_{eff} = \frac{P_{output}}{P_{accepted}}. \quad (1.5)$$

The minimum value for the l-value is 1 which is that of the dipole antennas. The possible dipole types are electric dipole, magnetic dipole or the combination of the two. The electrical antenna is a poor radiator in a lossy medium due to strong electric near-field resulting in higher loss as compared to magnetic antennas. For a case when the antenna is confined in a lossless insulation of radius a inside an infinite lossy medium, analytical expression for the radiation efficiency of the magnetic and electric antenna can be calculated as [54]:

$$\eta_{eff}|_{magnetic} = -\frac{\mathrm{Re}\{\eta\}}{\mathrm{Re}\left\{j|k|^2 a^2 \eta h_l(ka) \left(h_l'(ka) + \frac{1}{ka} h_l(ka)\right)^*\right\}} \quad (1.6)$$

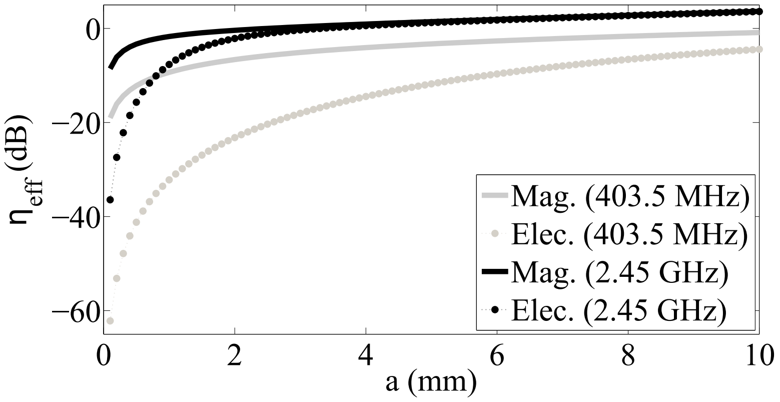

Figure 1.6: Efficiency of the electrical and the magnetic dipole antenna with different radius of the spherical insulation at 403.5 MHz and 2.45 GHz.

$$\eta_{eff}|_{electrical} = \frac{\mathrm{Re}\{\eta\}}{\mathrm{Re}\left\{j|k|^2 a^2 \eta h_l^*(ka)\left(h_l'(ka) + \frac{1}{ka}h_l(ka)\right)\right\}} \tag{1.7}$$

where $l = 1$ for the magnetic dipole or the electric dipole antenna, η is the wave impedance of the medium, and $h_l(kr) = h_l^2(kr)$ is the spherical Hankel function of the second kind. The power gain of the antenna, G, is defined as the product of directivity (D) and the antenna efficiency (η_{eff}) as $G = D\eta_{eff}$. The plots for different radius of the spherical insulation for the muscle tissue at 2.45 GHz and 403.5 MHz for the magnetic and electric dipole antenna are shown in Fig. 1.6. These plots clearly shows that the magnetic dipole antenna is more radiation efficient than the electric dipole antenna with thin insulations. A small hertzian dipole is an example of a electric dipole antenna and a small loop antenna is an example of a magnetic dipole antenna. These antennas are theoretical antennas and do not resonate by themselves. In practice usually self-resonating antennas are used for low mismatch loss. These antennas are usually a combination of both electric and magnetic antennas as both the magnetic and electric component of the fields radiate [8].

1.3.2 Specific Absorption Rate

One of the health issues related with the wireless implanted device or the on-body device is the absorption of the radiated EM energy by the surrounding lossy tissues of the body. This may result in whole-body heat stress and excessive localized heating, damaging the tissues. In order to prevent this, the rate at which the energy is absorbed by the tissues should be restricted so that the inbuilt thermo-regulatory mechanism of the body helps in normalizing the temperature [55]. Specific Absorption Rate (SAR) is the mass-normalized rate at which EM energy is absorbed by the tissue at a specific location. SAR is an important biologically effective quantity used in protection guidelines dealing with EM energy exposure. It is related with the electric field as:

$$SAR = \frac{\sigma_e}{\rho}|\mathbf{E}|^{\mathbf{2}} \tag{1.8}$$

where ρ is the tissue density [kg/m^3] and $|\mathbf{E}|^{\mathbf{2}}$ is the root-mean-square (RMS) magnitude of the electric field. Many scientific regulatory bodies have calculated the safety level of the power absorbed by the tissues. The regulated spatial peak SAR limitation in Europe is 2 W/Kg averaged over 10 g of tissue [56] and in USA, it is 1.6 W/Kg averaged over 1 g of tissue [57]. These limitations on the SAR value, limit the maximum power that can be accepted to the antenna.

The spatial peak SAR value averaged over 1 g of tissues for the in-the-ear hearing aid antenna (discussed in Paper I) is shown for the transversal plane having the peak SAR for the Duke phantom (phantoms are discussed in Section 1.4) in Fig. 1.7. The SAR was calculated from finite-difference-time-domain (FDTD) simulations. The spatial peak SAR averaged over 1 g of tissue was 107.7 W/kg for 1 W of source power. The location of the peak value can be seen around the ear canal. This is close to the position where the antenna was placed. Hence, the maximum power that can be accepted by the antenna for being compliant with 1.6 W/Kg limitation is 1.6/107.7 = 14.9 mW. On the other hand, the calculated peak value for 10 g averaging was 33.1 W/Kg for 1 W of source power. Hence, to be compliant with 2 W/Kg limitation, the accepted power of the antenna should be within 60.4 mW. Most of the wireless devices compliant with the limitation of 1.6 W/Kg averaged over 1 g will be within the limitation of 2 W/Kg averaged over 10 g of the tissues.

1.3.3 Propagation Aspects for the WBAN

This section discusses the propagation aspects in the WBAN scenarios. As discussed in Section 1.2.1, the propagation between the wearable devices usually take place through the on-body channel. For few cases the propagation might be through free space as shown in Fig. 1.3. For such cases, free space propagation mechanism is applicable except for the fact that the antenna performance would be influenced by the body and the movements of the body parts might result in the shadowing of the signal.

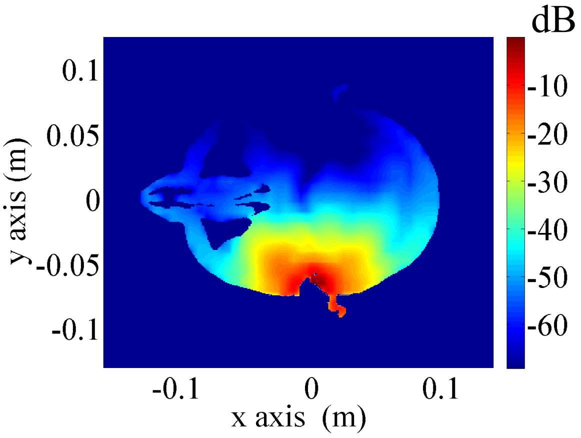

Figure 1.7: The spatial peak SAR averaged over 1 g of the tissues for the in-the-ear hearing aids antenna for the Duke phantom. For plotting in dB, normalization is done with the peak SAR value of 107.7 W/Kg. The input source power is 1 W. The location of the peak value can be seen around the ear canal. This is close to the position where the antenna was placed.

Cases where the devices are located around the body where the curvature is great or along the body where the curvature is minimal should be properly characterized due to high attenuation. The propagation between the devices located around the body takes place through creeping waves. A creeping wave is the wave that is diffracted around the curvature of the body that shadows the receive antenna from the transmit antenna. When the devices are located along the body where the curvature in minimal between the transmit antenna and the receive antenna, surface wave is a dominant propagation mode [18]. A surface wave is a wave that is guided by the body surface due to permittivity difference between the body surface and free space. These are illustrated through FDTD simulations done over a homogeneous cylindrical phantom of height 50 cm and radius 15 cm with $\varepsilon_r = 50$ and $\sigma_e = 1.7$ S/m at 2.45 GHz. More discussion about the phantom is done in Section 1.4. The creeping wave phenomenon is shown in Fig. 1.8(a) for a perpendicularly (w.r.t the body surface) placed small dipole antenna and in Fig. 1.8(b) for a tangentially placed antenna. The bending of the wavefront along the curvature of the phantom can be seen. Fig. 1.8(c) and Fig. 1.8(d) shows the surface wave propagation for along the body cases, for a perpendicularly and tangentially placed small dipole antenna, respectively. The tangential component of the electric field for the creeping wave as well as the surface wave attenuates more than the perpendicular component. This is shown in Fig. 1.9 where the magnitude of the perpendicular and tangential component of the electric field is plotted for around the body and along the body propagation at 2.45 GHz. This shows that an antenna for the on-body to on-body communication should be perpendicularly polarized with respect to the body surface. The link-loss for around the body propagation for different applications is analytically derived in the included papers (Paper II and Paper III).

The communication between two implants takes place through the human body as a propagation medium. When the waves propagate from the antenna of an implanted device, apart from the usual path-loss, the waves attenuate due to absorption in the lossy tissues and reflection at different tissue boundaries. It is challenging to characterize the loss due to different tissue thickness in different people. A simple way is to treat the human body with homogeneous electrical properties. In such a case the path-loss between the two implanted antennas can be written with the extended Friis formula as [58]:

$$(PL)_{lossy\_medium} = -20\log_{10}\left(\frac{\lambda_{eff}}{4\pi R}e^{-\alpha R}\right) \tag{1.9}$$

where $\alpha = |Im[k]|$, $\lambda_{eff} = \frac{2\pi}{Re[k]}$ is the effective wavelength in a lossy medium with k being the complex wave-number in the lossy medium, and R is the distance between the transmitting and receiving antennas.

To observe the field propagation inside the body, a simulation was done by placing a small dipole antenna inside a phantom having different tissues at the level of the waist at 403.5 MHz and 2.45 GHz. Fig. 1.10 shows the RMS magnitude of the electric field at the two frequencies. The source power for both frequencies is normalized to 1 W. As discussed earlier, the attenuation at 2.45 GHz is higher than 403.5 MHz. The ripples in the plots are the result of reflection at different tissue interfaces when the EM wave passes through them. At higher frequency, the thickness of the different tissues becomes comparable to the wavelength. Hence, the ripples are more prominent at 2.45 GHz.

1.4 Phantoms

An implant or an on-body antenna has to be characterized and tested before actual implementation in a realistic scenario. However, due to safety and ethical reasons, often it is not possible to initially test their performance on/in a real human subject. Even at the design and the optimization stage of the antenna in simulation software, it should be surrounded by the lossy tissues for a more realistic scenario. Moreover, to investigate the interaction of the EM waves with

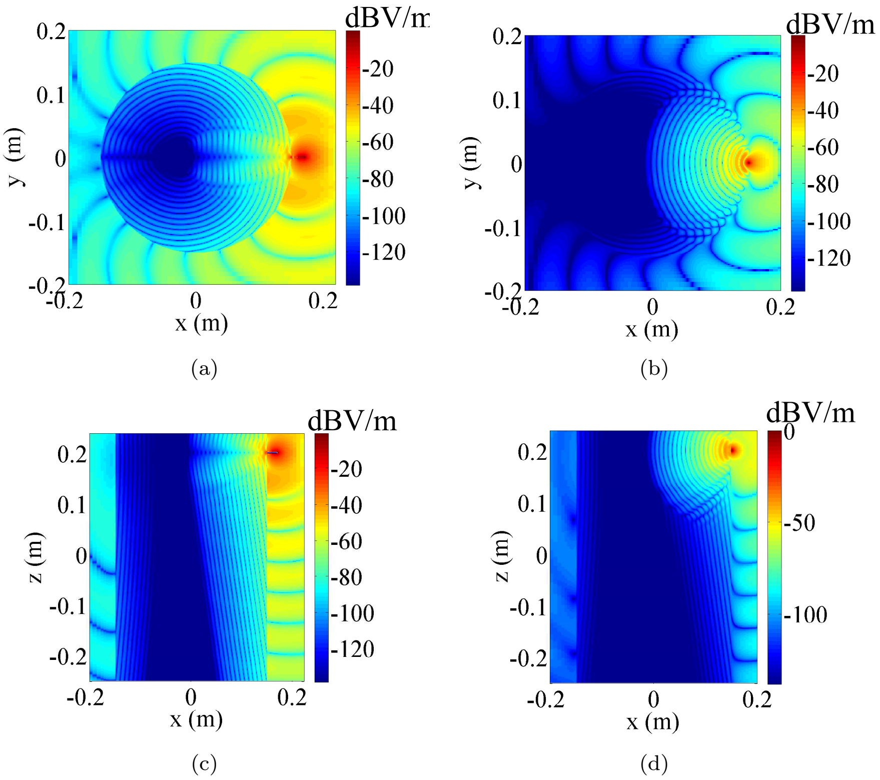

(a)

(b)

(c)

(d)

Figure 1.8: Magnitude of the electric field for the propagation over the body for (a) the creeping wave for around the body propagation for a perpendicularly placed dipole antenna (b) the creeping wave for around the body propagation for a tangentially placed dipole antenna (c) the surface wave for along the body propagation for a perpendicularly placed dipole antenna and (d) the surface wave for along the body propagation for a tangentially placed dipole antenna.

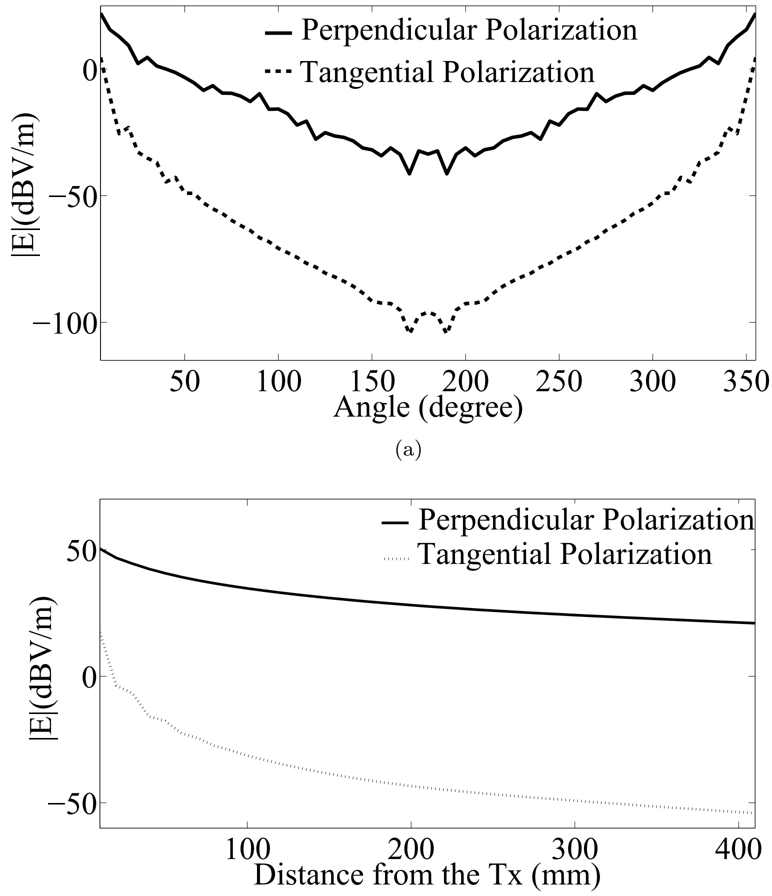

(a)

(b)

Figure 1.9: Magnitude of the tangentially polarized electric field vs. magnitude of the perpendicularly polarized electric field for (a) around the body propagation (b) for along the body propagation

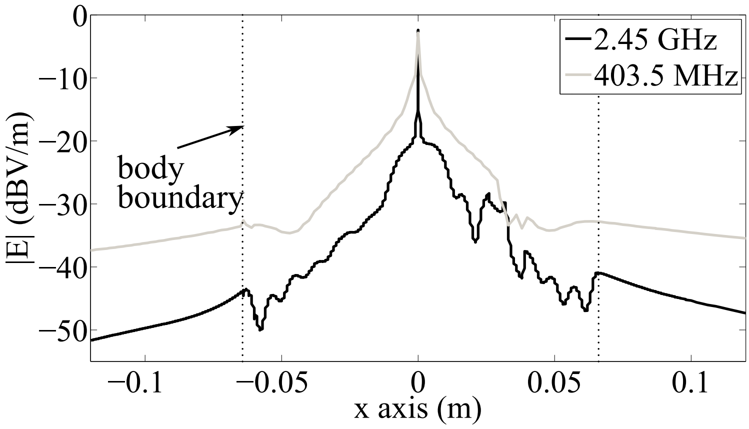

Figure 1.10: RMS magnitude of the electric field from a source inside a heterogeneous phantom at (a) 403.5 MHz (b) 2.45 GHz. The transmit antenna is at the center and the plots show the field from front of the body to the back of the body. The source power for both the frequency is normalized to 1 W.

the tissues, a model which mimics the electrical properties of the different tissues of a human body is needed for the SAR calculation. Furthermore, a body model is needed for the investigation of the EM wave propagation, around and inside the human body for a link loss calculation. The link loss calculation is necessary for designing a robust and a reliable wireless link. For such purposes, phantoms are developed. A phantom is defined as a simulated biological body or as a physical model simulating the characteristics of the biological tissues [8]. A phantom is generally valid in a frequency range as electrical properties of the tissues changes with the frequency as shown in Fig. 1.11 for a high water content tissue (muscle) and a low water content tissue (fat). The attenuation of the EM wave when traveling through the tissues also changes accordingly. The attenuation α_{attn} in Neper/m (1 Neper = 8.686 dB) of the EM waves in a lossy medium is given by:

$$\alpha_{attn} = \omega\sqrt{\frac{\mu\varepsilon_0\varepsilon_r}{2}\left(\sqrt{1+\left(\frac{\sigma_e}{\omega\varepsilon_0\varepsilon_r}\right)^2}-1\right)}, \tag{1.10}$$

where $\mu = \mu_0 = 4\pi \times 10^{-7}$ H/m is the permeability of the free space as the tissues are non-magnetic, $\varepsilon_0 = 8.85 \times 10^{-12}$ F/m is the permittivity of the free

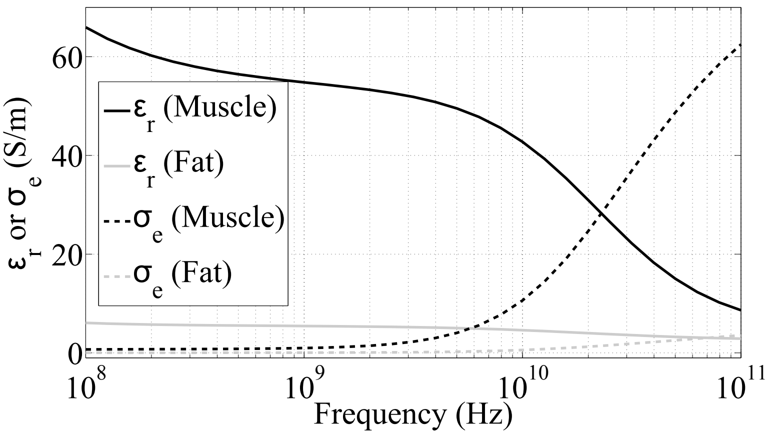

Figure 1.11: The variation of electrical properties of a high water content tissue, muscle, and a low water content tissue, fat, over a frequency range from 100 MHz to 100 GHz [59].

space, ε_r is the relative permittivity of the tissue, σ_e is the conductivity in S/m, and $w = 2\pi f$ with f being the frequency in free space. The attenuation in dB/m for fat and muscle at 403.5 MHz and 2.45 GHz is shown in Table 1.1.

For some applications, phantom representing a particular tissue or the average electrical properties of the different tissues is sufficient. Usually, the tissues are classified into two groups depending on the water content. Bone and fat are low water content tissue having low permittivity and low attenuation (as shown in Table 1.1). On the other hand, muscle, brain and skin are high water content tissue having high permittivity and high attenuation. A homogeneous phantom can represent either of these tissues or an average of the electrical properties of these tissues. A heterogeneous phantom has different tissues. It

Table 1.1: Attenuation of Fat and Muscle

Tissue	Frequency	ε_r	σ (S/m)	α_{attn} (dB/m)
Fat	403.5 MHz	5.58	0.04	27.37
Fat	2.45 GHz	5.28	0.10	71.05
Muscle	403.5 MHz	57.1	0.80	165.99
Muscle	2.45 GHz	52.73	1.74	389.33

could be a simple multi-layer tissue model or an anatomically correct phantom. The use of a phantom also guarantees the repeatability of the investigation process as different human bodies have different shapes, sizes, and thicknesses of these tissues.

A simulated biological body is a numerical or a digital computer model of a human body. It could be a simple homogeneous cylinder having the average electrical properties of the different tissues, or a more complex and anatomically correct phantom having almost all different tissues of a human body. A physical phantom could be a plastic container filled with a homogeneous tissue-stimulating liquid, a semisolid (gel), or a solid phantom. Different types of the phantom used in this research work are described below.

1.4.1 SAM Head Phantom

The Standard Anthropomorphic Model (SAM) shown in Fig. 1.12 is a head shell phantom which was developed as a part of European Collaborative Research Program named SARSYS [60] with MCL [61], SPEAG [62], ITIS [63], and the University of Gent [64] as partners. The dimensions of the phantom is that of 90^{th} percentile of various male head dimensions, obtained from the data of a large anthropometric study of men and women of various ethnic origins, aged over 20 years, randomly selected among US army personnel [65]. Both the numerical model and the physical model are commercially available. The physical model has an outer fiberglass shell of thickness around $2-3$ mm. The shell can be filled with the tissue stimulating liquid. A solid SAM

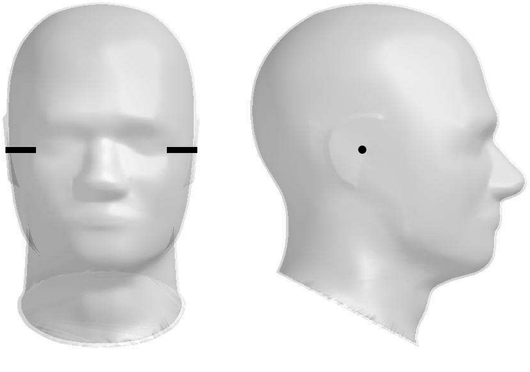

Figure 1.12: Modified SAM Phantom with ear canals

phantom made from carbon-loaded silicone rubber valid in a wide frequency range (130 MHz - 6 GHz) is also available [61]. The numerical SAM phantom is a computer model of the physical SAM phantom with the shell where the electrical properties of the shell and the liquid could be assigned in an EM wave simulator.

The primary use of the SAM phantom is for the calculation of the SAR from the mobile phones (or other hand held device) and their radiation pattern testing. However, we have modified the numerical SAM phantom to include the ear canal in [48] and also to include the outer ear in [66] for the binaural hearing aids application described in Section 2.1.

1.4.2 Poser Phantoms

Poser phantoms are created in a 3D-CAD software called POSER supplied by Curious Labs Inc. [67] and then imported to the electromagnetic wave simulator. The advantages of these phantoms are that they are anthropomorphic and are easy to represent different snapshots of a dynamic scenario with the moving body parts. They are shown in Fig. 1.13. However, they can be modeled just as a homogeneous phantom. In [68], they are used for investigation for gain variation of an implant antenna due to the arm movements or due to

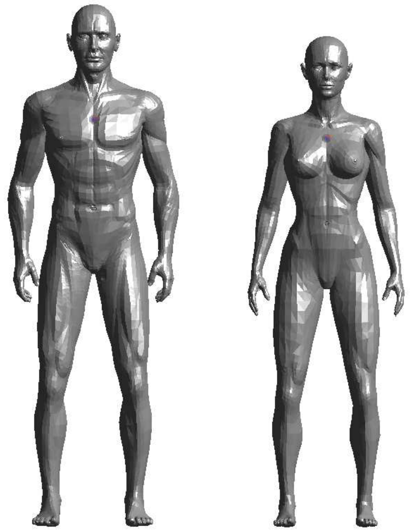

Figure 1.13: A male and a female poser phantom

the different body sizes. In this research work, we have used these phantoms for the investigation of around the body propagation channel considering the arms' influence [69] which is presented in Paper III. A male and a female poser phantoms are also used by us in [70], for the directional analysis of the on-body propagation channel. In [71] (Paper IV), we have used these phantoms for arm movements analysis by using different poses of the human body during a walk cycle.

1.4.3 Virtual Family and Classroom Project Phantoms

Virtual family and classroom project phantoms are whole body anatomical heterogeneous phantoms with more than 80 different tissues obtained from the high resolution magnetic resonance imaging (MRI) of real human beings. They are provided by ITIS foundation [63] developed for the Virtual Family and Classroom project [72]. The virtual family phantoms consist of four phantoms, a male phantom named Duke of age 34 year, a female phantom named Ella of age 26 year, a phantom of a girl named Billie of age 11 year, and a boy phantom named Thelonious who is 6 years old. They are shown in Fig. 1.14. The virtual classroom project phantoms complement the phantoms of the virtual family. They also consist of four phantoms, namely, Louis, a 14 year old male, an 8 year old female child Eartha, an 8 year old male child Dizzie, and a 5 year old female

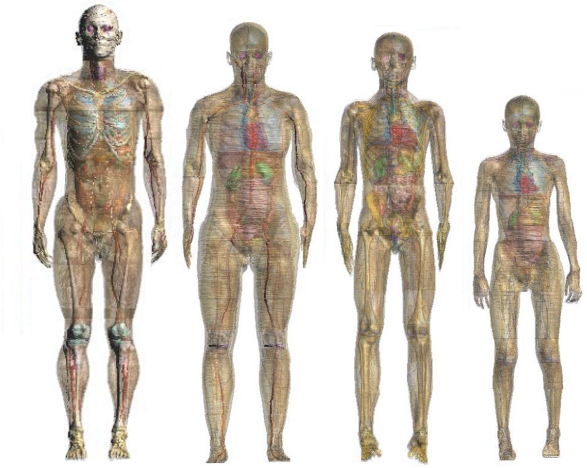

Figure 1.14: Virtual Family and Classroom Project Phantoms. From left to right: Duke, Ella, Louis, and Billie

child Roberta. We have used Duke, Ella, Billie, and Louis in this research. They have been used to investigate the effect of different head sizes for the ear-to-ear propagation channel in [12] (Paper II) and [66]. Duke and Bille are used in [73] for the verification of the analytical model for the propagation channel around the torso. We used Billie as a heterogeneous phantom for localization of the wireless capsule endoscopes in [74]. One of the limitations of using whole body phantoms with different tissues is a long simulation time due to large number of cells in FDTD simulations. Hence, the phantom is truncated to include the area of interest in the simulation domain, e.g. in [12], only the head and the neck has been used for the ear-to-ear propagation channel.

1.4.4 Physical shell phantom with head, shoulder, and upper torso

We have used a physical phantom made with fiberglass shell having the head and the shoulder shown in Fig. 1.15 for measurement of the ear-to-ear propagation channel in [12]. The phantom is hollow and is filled with the tissue stimulating liquid mimicking the average electrical properties of the human head tissues at 2.45 GHz ($\varepsilon_r = 39.2$ and $\sigma_e = 1.80$ S/m). The tissue stimulating liquid is prepared according to the recipe discussed in IEEE Std. 1528-2003 [75]. The electrical properties of the tissue stimulating liquid were measured by Agi-

Figure 1.15: A Physical Shell Phantom with Head and Shoulder

lent 85070D dielectric probe kit using open ended coaxial probe. The phantom does not have the outer ear called pinna. It was fabricated by 3D printing and then attached to the phantom to verify the effect of the pinnas on the ear-to-ear propagation channel. The details are described in Paper II [12].

1.4.5 Semisolid Phantom

One of the disadvantages of using a phantom with an outer shell is the underestimation of the on-body link loss. This is because of the fact that the outer shell are generally made of almost lossless material like fiberglass or plastic. A solution for such problem is using a semisolid phantom. We have used a semisolid phantom as shown in Fig. 1.16 consisting of electrical properties of 2/3 of the muscle at 2.45 GHz ($\varepsilon_r = 35.1$ and $\sigma_e = 1.15$ S/m) for measurement of around the body propagation channel which is described in Section 2.2.1. It has been developed at the Ito and Saito laboratory, Chiba University [76] in Japan. Materials and their quantity used for making this phantom at 2.45 GHz is shown in Table 1.2. Such semisolid phantom degrade over time due to evaporation of water and therefore, require a proper maintenance like keeping in a refrigerator after use by covering it with a plastic wrap to maintain its electrical properties.

Figure 1.16: A cylindrical semisolid phantom used for the measurement of the channel around the body.

Table 1.2: Materials for 2/3 Muscle Tissue at 2.45 GHz

Material	Quantity (gm)
Deionized water	3375
Agar	104.6
Sodium Chloride	7
Polyethylene powder	1012.6
TX-151	30.1
Sodium Dehydroacetate	2

1.4.6 Effect of outer lossless shell

In [12] (Paper II), we have shown that one of the reasons for low ear-to-ear link loss for the SAM phantom when compared to the Duke phantom is the presence of the outer lossless shell in the SAM phantom. It is shown that modeling the outer lossless shell of the numerical SAM phantom with a lossy material with the electrical properties of the liquid filled in the SAM phantom, resulted in an increase of the link loss by 15 dB. Similarly, modeling the outer tissue i.e. skin of the Duke head with a lossless material decreased the link loss by 13 dB. The ear-to-ear propagation is an example of around the body propagation where the devices are located on the opposite side of the body. FDTD Simulations are done at 2.45 GHz to verify the effect of the outer lossless shell in both around the body propagation, a non line-of-sight (NLOS) case, and along the body propagation, a line-of-sight (LOS) case, with the on-body antenna presented in [19]. A circular cylindrical phantom with diameter 20 cm (including 3 mm outer shell for the lossless shell case) and height 50 cm is used. The lossless shell has electrical properties of $\varepsilon_r = 3.7$ and $\sigma_e = 0$ S/m. The phantom has homogeneous electrical properties of 2/3 of the muscle at 2.45 GHz as described in Section 1.4.5. In FDTD simulations, the simulation boundary is terminated by an uniaxial perfectly matched layer (UPML) with an absorbing boundary condition. The termination at the top and the bottom was at the height of the phantom to prevent any waves going over or under the phantom.

Fig. 1.17 shows the S_{21} with and without the shell for the LOS case when the receive antenna is moved along the body and is always aligned with the transmit antenna. S_{21} with and without the outer lossless shell for the NLOS propagation around the body is shown in Fig. 1.18. It can be seen that for the LOS propagation along the body, the presence of the lossless shell at 2.45 GHz for the antenna used does not have any influence on the link loss (negative of S_{21} in dB). However, the link loss is lower in the presence of the lossless

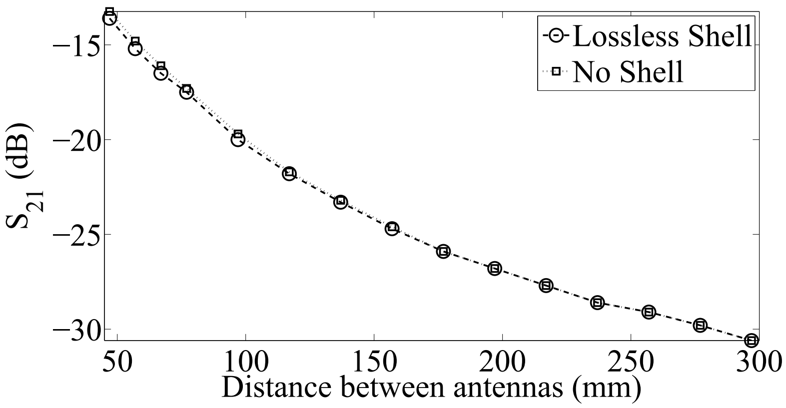

Figure 1.17: S_{21} between the antennas with and without the outer shell on a numerical phantom for along the body LOS propagation.

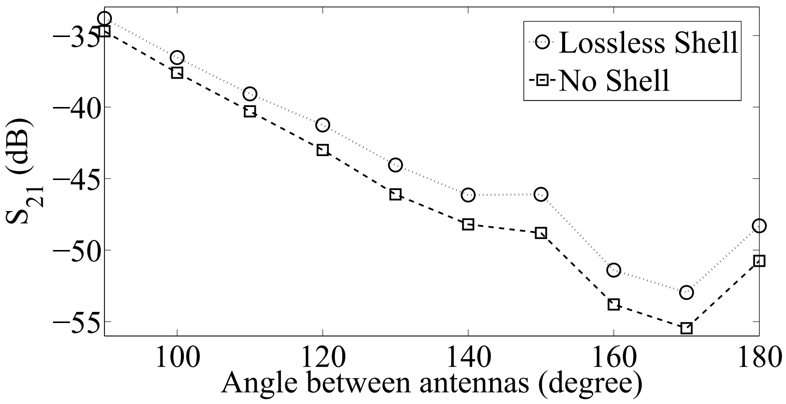

Figure 1.18: S_{21} between the antennas with and without the outer shell on a numerical phantom for around the body NLOS propagation.

shell than without it for the NLOS propagation around the body. Moreover, for this case, the difference between the link loss with and without the shell decreases as the angle between the transmit antenna and the receive antenna decreases and the propagation approaches the LOS case. Hence, any physical or numerical phantom with an outer lossless shell should be used with caution for calculating the link loss when the devices are located around the body.

1.5 Link Budget

A link budget relates the transmitter power to the received signal-to-noise ratio (SNR) taking into account factors such as loss and gain of the components, noise figure, fading margin, and path-loss. If any one of the factors is not known, it can be calculated from the link budget. Usually for the WBAN, when the devices are close to the human body or implanted, the antennas form part of the propagation channel. Hence, instead of using the path-loss which is the loss of the signal while propagating through the medium, we use the term link loss which is the path-loss including the antenna gain. An example of the link budget to calculate a fading margin for the binaural hearing aids is described in Table 1.3 as discussed in [5]. A fading margin is added in the link budget which takes care of the temporal and the spatial variation of the propagation channel ensuring that the minimum received power is exceeded in at least, e.g., 90% of all the cases [77].

Table 1.3: Link Budget

Factor	Symbol	Value
Noise Spectral Density	$k_B T_e$	-174 dBm/Hz
Insertion Loss of SAW filter	L_{SAW}	3 dB
Noise figure (analog part)	NF_{analog}	13 dB
SNR per bit at BER of 0.001	E_b/N_0	10 dB (coded)
Bit rate	b	125 kbps
Sensitivity$_{RX}$ $= k_B T_e + L_{SAW} + NF_{analog} + E_b/N_0 + 10\log_{10} b$ = -97 dBm		

At the bit-error-rate (BER) of 0.001, the required SNR per bit (E_b/N_0) for the demodulation found from the baseband simulation for the coded case was 10 dB [5]. As shown in Table 1.3, the calculated receiver sensitivity is -97 dBm for a bit rate of 125 kbps. Assuming that the transmitter has $P_{TX} = -7$ dBm output power which results in -10 dBm after the SAW filter losses, the link loss LL is calculated as: $LL = P_{TX}$ - Sensitivity$_{RX}$ $= 87$ dB. In [12], we have shown that the ear-to-ear link loss for the largest head is 79 dB. Hence, this gives 8 dB of fading margin.

Chapter 2

Investigated Wireless Body Area Network Applications

This chapter provides an overview of investigations done for various WBAN applications during my graduate study. The applications are: (a) Binaural Hearing Aids (b) Sensors Placed Around the Body (c) Localization in Wireless Capsule Endoscopy (d) In-mouth Devices. It also present results of measurements which have not been submitted or published so far.

2.1 Binaural Hearing Aids

A hearing aid is an electro-acoustic medical device used by a hearing impaired person for improved hearing. It is used by people who still have some hearing left. The hearing aid consists of electronic circuits, controls, battery, a microphone and a loudspeaker. Usually, the complete system can be enclosed in an ear-mold made from the impression taken from the individual's ear, or alternatively soft ear inserts are used, so that the hearing aid fits perfectly inside the ear of the user. Hearing aids are classified by the way they are placed in the ear. The best type of hearing aid required by a person can be decided by an audiologist. An audiologist is a health professional specializing in hearing who performs a hearing test to assess the type and degree of hearing loss [78]. The three basic types of the hearing aid are: behind-the-ear (BTE), in-the-ear (ITE), and in-the-canal (ITC) as shown in Fig 2.1.

In a BTE hearing aid, the electronic circuit is contained in a plastic casing which is placed behind the outer ear. It is connected to an ear-mold that fits inside the outer ear. Amplified sound travels from the hearing aid through the

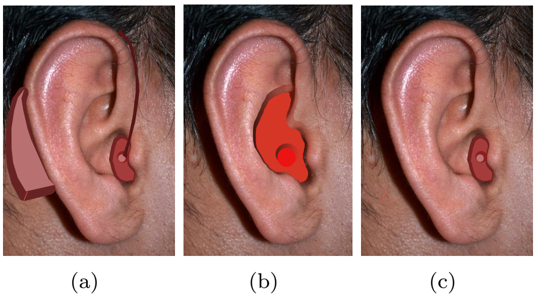
(a) (b) (c)

Figure 2.1: Illustration showing placement of three main types of the hearing aids: (a) Behind-the-Ear (b) In-the-Ear (c) In-the-Canal.

ear-mold and into the ear. It can be used by people with mild to profound hearing loss [78]. The ITE hearing aid is placed inside the outer ear and the users are those suffering from mild to severe hearing loss. An additional feature which might be present in the ITE aids is a telecoil which is a small magnetic coil. In a telecoil-enabled ITE hearing aid, users receive the sound through the circuitry of the hearing aid instead of the microphone. By this method, the user can hear the conversations over the telephone easily. Additionally, a telecoil helps users in some public facilities, such as airports, that have special sound systems installed, called induction loop systems. The ITE hearing aid is not recommended for children as the casing need to be replaced as the ear grows with the age [78]. The smallest type of hearing aid is the ITC aid which fits into the ear canal. A more compact and smaller version of the ITC is completely-in-canal (CIC) hearing aid which is almost completely hidden in the canal. However, because of it's small size, the ITC aid is difficult to adjust or remove. Additionally, an ITC aid lacks any additional devices like the telecoil due to its small size. Moreover, the reduced size of the ITC aids limits their amplification performance. Hence, they are not suitable for people with severe to profound hearing loss [78].

For a better hearing experience, binaural hearing aids are recommended. Binaural processing in audiology is the capability of the brain to process sound coming from both the left and the right ears, which helps in localizing the source of a sound [79]. In a binaural hearing aid system there is a hearing aid in both ears of the user. Thus, binaural hearing aids have a better localization performance compared to a single hearing aid. Modern binaural hearing aids use adaptive filtering for noise suppression. Synchronization of such hearing aids is important for improved hearing in noisy environments. Unsynchronized hearing aids may result in poor localization and thus the user might not be able to predict the direction to the source of the sound correctly. Therefore, binaural hearing aids need to communicate with each other. Another reason for the communication of hearing aids is that if the volume or any specific listening environment program like for concert or restaurant is selected in one hearing aid, it should be communicated to the other. This eliminates the need for changing or adjusting the volume or program manually in the other aid. The communication between the hearing aids in a binaural system takes place over the ear-to-ear propagation channel.

The objective of the research was to investigate the possibility of using the 2.45 GHz ISM band for the communication between the binaural hearing aids. The ITE and the ITC placement scenarios have more stringent requirements on the size of the hearing aid than the BTE placement. Hence, these two scenarios were chosen for the investigation. Two small antennas were designed for each of these cases and the link loss between the antennas was calculated [48] (Paper I). A detailed investigation was made for the ITE placement scenario as it was found in a preliminary investigation that the link loss between the ITE antennas is low enough for a reliable link between the hearing aids. An analytical model was developed to calculate the link loss between antennas for the ear-to-ear propagation channel which incorporates the size of the head, antenna gain, and the dominant signal path between the ears carrying most of the EM energy.

2.1.1 Ear-to-Ear Propagation Channel

The communication between the binaural hearing aids takes place through the ear-to-ear propagation channel. The propagation channel from one ear to the other ear could have two possibilities: (i) on-body ear-to-ear propagation channel which consists of several paths from the antenna in the hearing aid placed in one ear to the antenna in the hearing aid placed in the other ear, over the head surface, and (ii) through-the-body ear-to-ear propagation channel which consists of paths through the lossy tissues of the human head. The through-the-body path-loss, assuming plane waves and infinite lossy medium, and considering a direct path with an average distance between the ears to be $d = 160$ mm from (1.9) is about 115 dB. Further, it should be noted that while calculating this theoretical path-loss, other losses like reflection losses, which might be present when there are several layers of tissues, are ignored. Hence, this loss is under-estimated. However, from our simulations in [66], the link loss was found to be 79 dB for the ITE placement for the Duke phantom head and 75 dB for the SAM head with the outer ears and the lossy outer shell. Moreover, the loss for the ITC placement was 92 dB for the SAM head [48].

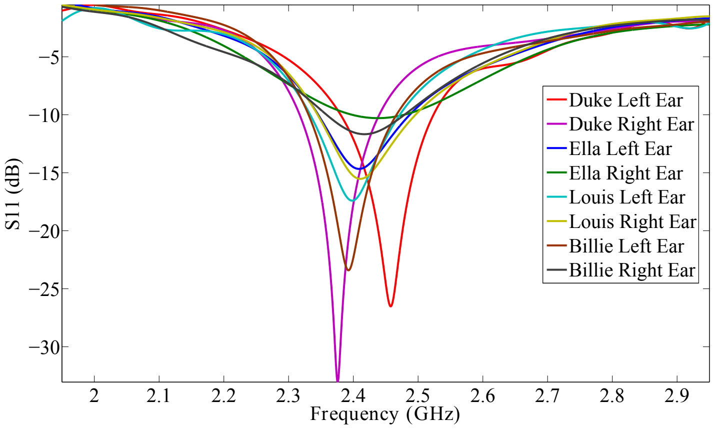

Figure 2.2: Reflection coefficient (S_{11} (dB)) of the ITE antenna placed in the ears of different phantoms [66].

Although the link loss contains the gain (which is negative in dBi) of the antennas, it is still much lower than the theoretical path-loss through the head. This suggests that the wireless communication between the hearing aids mostly takes place through the on-body ear-to-ear propagation channel. Hence, the on-body propagation channel is dominant than the in-body channel for the devices located on the opposite side of the body. This is also shown in [17].

To investigate the ear-to-ear propagation channel, either simulations with numerical phantoms are done or measurements are performed on physical phantoms. The antennas are placed in each ear and the ear-to-ear link loss is calculated or measured. Previous research have investigated on design of miniature antennas for the hearing aids [80]-[84]. In [48], we presented two antennas suitable in size and performance for the ITE and the ITC hearing aids at 2.45 GHz. The antennas were designed and optimized by placing them in the ear of the modified SAM phantom shown in Fig. 1.12. The placement of the ITE antenna in different heterogeneous phantoms shown in Fig. 1.14 resulted in mismatch and detuning as seen in Fig. 2.2. It can be seen from the figure that the detuning of the antenna not only depends on the phantom but also on the placement of the antenna in the different ears within the same phantom. This variation is caused by the asymmetric anatomy of the human ear and the human head as a whole. However, the antenna still has an acceptable matching ($S_{11} < -10$ dB) at the center frequency.

In [48], we found that the simulated ear-to-ear link loss for the modified

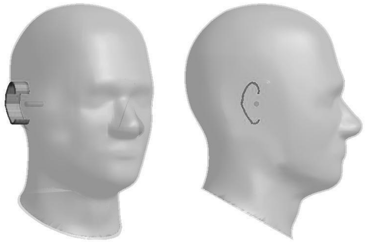

Figure 2.3: A model of pinna attached to the SAM phantom.

SAM phantom for the ITE case was 49 dB. However, with the same antenna, the link loss for the Duke phantom was 79 dB. Thus, there is a difference of about 30 dB in the link loss between the SAM phantom and the Duke phantom. The SAM phantom is a homogeneous phantom and Duke is a heterogeneous phantom, but as mentioned earlier, the heterogeneous nature of the tissues inside the head does not contribute significantly for the ear-to-ear communication owing to high attenuation through the head. The reasons for this difference in the link loss between the two phantoms were investigated. Apart from the variation in the dimensions, there are two basic differences between the SAM phantom and the heterogeneous phantoms: (a) the SAM phantom has an outer lossless shell (b) the pinna (outer ear) is protruding in the heterogeneous phantoms. To investigate the effect of these, the SAM shell was assigned the same electrical properties ($\varepsilon_r = 39.2$ and $\sigma_e = 1.80$ S/m) as that of the SAM liquid. Moreover, simple pinnas which protrudes 18 mm (same as the Duke phantom) was modeled and attached to the SAM phantom as shown in Fig 2.3. The effect of these modifications on the SAM phantom resulted in a link loss of about 75 dB which is closer to the link loss of Duke [66].

As discussed in Section 1.3.3, the creeping wave is a dominant propagation mechanism by which the devices located on the opposite side of the body as in binaural hearing aids communicate with each other. The waves radiated by the antenna in one of the hearing aids get diffracted around the head surface to reach the antenna in the other hearing aid. Hence, the analytical modeling of the ear-to-ear link loss is done as a creeping wave. There can be several paths from one ear to the other ear over which the creeping wave travels. However, not all the paths of the creeping wave contribute to the received power as some paths might be longer than other paths and the creeping wave will attenuate to a great extent over these paths. We did several simulations over the Duke head to determine the dominant creeping wave paths for the ear-to-ear propagation channel. In [12], it is shown that the path going over back of the head, and the path going in front of the head, at the level of the ears, contributes most of the power for the designed ITE antenna. An analytical link loss model was developed for the ear-to-ear propagation channel which models the head with an elliptical cross-section and includes the losses for these two dominant paths of the creeping waves over an elliptical surface. The model also includes the losses due to the pinnas. It is computationally more efficient than FDTD simulations for calculating the link loss of different head sizes. These results are presented in the Paper II.

The effect of the placement of the antennas inside the canal was investigated using the ITC antenna on the modified SAM phantom. The effect of the pinna is more dominant for certain placement positions inside the canal. It was found that when the antennas were placed deep inside the canal separated by 150 mm, the fields were more confined and the link loss was about 95 dB. At 160 mm, it was 89 dB, as the antennas were placed at the outer boundary of the ear canal resulting in higher coupling between the antennas. From this, one could conclude that deeper placement of antennas inside the canal results in high link loss, as reflected by higher value of the link loss at 150 mm than at 160 mm. This is also discussed in [84]. However, this may not always be true. We did simulations to verify the effect of placement of the antennas in the canal with the ITC antenna. The distance between the antennas was increased for each simulation i.e. first the simulation was done by placing the antennas deep inside the canal and then they were gradually moved towards the outer boundary of the canal. The result is presented in Fig. 2.4. From Fig. 2.4, it can be seen that as the distance between the antennas is increased, the link loss increases, reaches a maximum and then starts decreasing. The link loss is given by negative of S_{21} in dB scale. One of the possible explanations for this behavior is due to the interference between the fields from various paths. Further, from Fig.2.4, it can be seen that the presence of pinna can introduce extra loss up to 10 dB, depending on the placement position inside the canal.

By these investigations it can be concluded that if a phantom is used for estimation of the ear-to-ear link loss, it should have lossy outer surface and pinnas for a more accurate estimation. Moreover, the antenna for hearing aids should be polarized in such a way that it radiates the waves with electric field perpendicular to the head surface as the propagation between the hearing aids antenna mostly takes place through the creeping waves which have lower attenuation for the perpendicular polarization.

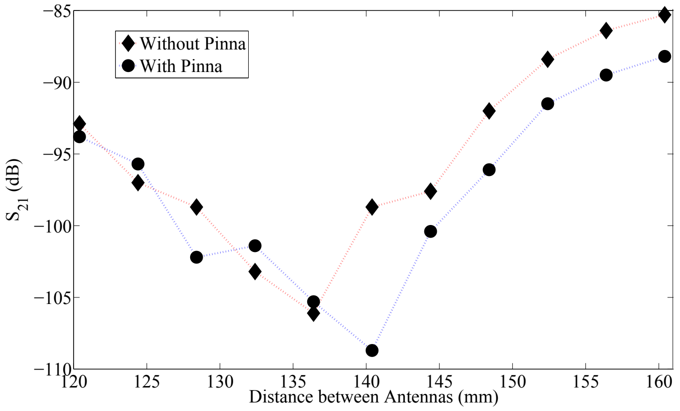

Figure 2.4: Effect of placement of the ITC antenna at different positions inside the canal

2.2 Propagation Around the Body

In the WBAN, there might be a scenario where the devices are located around the torso. As in the case with the hearing aids, the wireless devices placed around the torso communicate through creeping waves. Although the distance between the devices is typically within a meter, the losses could be high as the creeping waves undergo exponential attenuation with distance [16]. Hence, the estimation of the link loss between the on-body devices is essential for an accurate link budget and deciding the necessary sensitivity for a reliable wireless link. Various methods for determining the link loss between the on-body wireless devices are through FDTD simulations [16], measurement on phantoms [19] or actual human volunteers [85]. Statistical and deterministic propagation/link loss models for various WBAN scenarios are presented in [14]-[18], [86], and in our work in [73] and [69](Paper III). The statistical approach models the link loss in a dynamic scenario when the body is moving [86] and the deterministic approach models the link loss in a stationary environment when the body is static as in [17], [73]. The deterministic link loss can be obtained through the analytical models, which are easier to handle and are computationally more efficient when compared with FDTD simulations which are time and memory consuming.

As the creeping waves over the human body attenuate exponentially with distance, the two shortest paths, one going in clockwise direction and other going in anti-clockwise direction at the level of the antennas can be used to describe the model. In [16] and [17], it is shown that these clockwise and anti-clockwise creeping waves interfere with each other resulting in fading dips.

Most of the analytical models are developed by modeling the torso with a circular cross-section. The importance of the torso shape for correctly quantifying the path-loss around the body is discussed in [87]. Fig. 2.5 shows the cross-section of the torso of the Duke phantom at the waist level. It can be seen that it fits more accurately with an ellipse rather than a circle. Hence, an analytical model based on the attenuation of the creeping waves over an elliptical surface would give more accurate estimation of the link loss. In [73], we developed an analytical model for the propagation around the torso based on the elliptical approximation of the torso which is given by:

$$\begin{aligned} LL_n\big|_{\mathrm{dB}} &= -10\log_{10}\frac{P_{RX}}{P_{TX}}\bigg|_n \\ &= -10\log_{10}\left[\frac{G_{RX}G_{TX}\lambda^2}{4\pi^2}\left(\left|\frac{e^{-L_{cn}}}{d_n}e^{-jkd_n}+\right.\right.\right. \\ &\qquad \left.\left.\left.\frac{e^{-L_{acn}}}{p-d_n}e^{-jk(p-d_n)}\right|\right)^2\right] \qquad (2.1) \end{aligned}$$

where p is the perimeter of the ellipse and d_n is the length of the clockwise path at the n^{th} receiver position, L_{cn} and L_{acn} are the complex attenuation factors representing the loss on the elliptical surface for the clockwise and the

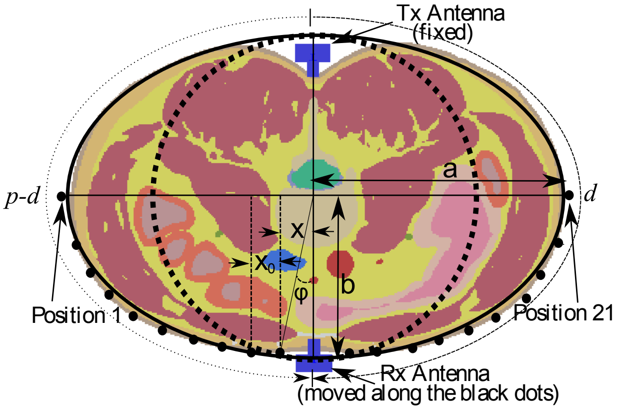

Figure 2.5: Elliptical approximation of the Duke torso. It can be seen that the torso cross-section fits more accurately to an ellipse than a circle. The positions of the receive antenna to validate the model along with other parameters is also shown.

anti-clockwise creeping wave, respectively. Their detail expression can be found in Paper II and Paper III. G_{TX} and G_{RX} are the on-body gain of the receive and the transmit antenna in the direction of the creeping wave. The analytical model was verified through FDTD simulations on the torso of Duke and Billie. The values of a and b for the elliptical approximation of Duke and Billie is shown in Table 2.1. The electrical properties of the tissues in the model were assigned at 2.45 GHz and is assumed to be constant in the simulation band. Since we are interested in the torso of the body, only the truncated bodies of the phantoms were included in the simulation domain. Moreover as discussed in [88] and shown later in Fig. 2.10, the whole body has minimal influence for the channel around the body. Hence, using a truncated model is justified. Further, the arms were excluded at this stage. The ITE antenna developed in [48] was used as the transmit antenna and the receive antenna. The transmit antenna was fixed at the central back and the receive antenna was moved along the front abdomen between 21 equally spaced points at an interval of $a/10$ along the major axis of the ellipse as shown in Fig. 2.5. The resonance frequency of the antenna when placed on the Duke torso was 2.32 GHz and on the Billie torso it was 2.38 GHz. Moreover, the antenna gain varies at different positions on the abdomen. The plots for the analytical model of (2.1) along with the simulation results for Duke and Billie are shown in Fig. 2.6(a) and Fig. 2.6(b), respectively. The figures show the plot for analytical model assuming a constant gain (obtained at the central abdomen position from the simulation) and then using the antenna gain[1] at the different positions. The result for the analytical model described in [17] for a circular torso with the same perimeter as that of the elliptical approximation of the actual torso is also shown. It can be seen that it under-estimates the link loss when compared with the analytical model based on the elliptical approximation of the torso. Moreover, the positions of the predicted fading dips from the elliptical model coincide with the simulation. A fading dip is a significant decrease in the received power due to destructive interference. If possible, the placement of the receiver should be avoided at these positions.

---

[1] There is no well defined measure (to the best of our knowledge) such as the gain for the coupling from the antenna to the creeping wave over the human body which involves near-field effects. However, as discussed in [17] and observed from the elliptical model verification, a good agreement between the simulation and the analytical model is obtained with the standard gain. Hence, using the gain which does not involve near-field effect in the analytical model is an effective approximation.

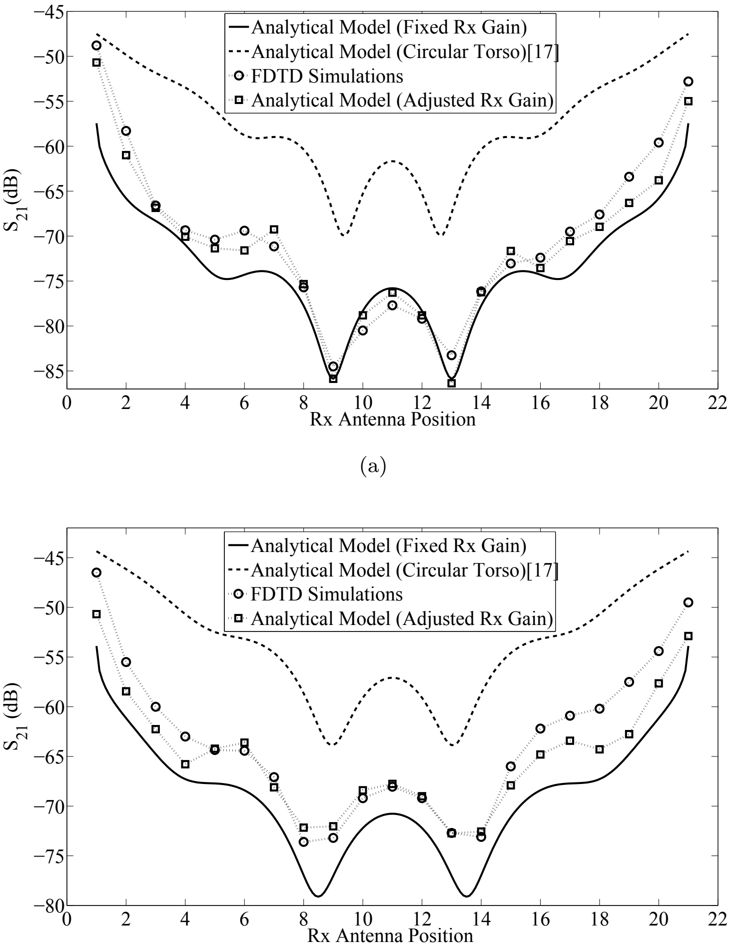

(a)

(b)

Figure 2.6: Verification of the analytical model based on the elliptical approximation of the Duke torso (a), and for the Bille torso (b). S_{21} calculated from the circular approximation based on the analytical model of [17], for the same perimeter of the body is also shown.

Table 2.1: Fitted Ellipse Dimension for the Phantoms

Phantom	a (mm)	b (mm)
Duke	140.9	90.5
Billie	105.6	72.9

2.2.1 Measurement of Propagation Channel Around the Body

Measurements were carried out to verify the developed elliptical analytical model (2.1) on a phantom for a special case of an ellipse when the major-axis is equal to the minor-axis i.e. for a circle. The measurements were done on a semi-solid circular phantom described in Section 1.4.5 at the Ito and Saito laboratory, Chiba University [76]. The phantom is 50 cm in length and has radius of 10 cm. An on-body antenna presented in [19] was used as a transmit and a receive antenna. The antennas were connected to the VNA through cables having ferrite beads to reduce any leakage radiation. The phantom was placed on a table and the whole setup was surrounded by absorbers to reduce any multipath components from the room. The resonance frequency of the antenna when placed on the phantom was around 2.3 GHz. The transmit antenna was fixed at the height of 25 cm and the receive antenna was manually moved from 90° to 270° with respect to the transmit antenna at the same level, and S_{21} was recorded. The receive antenna was moved in a step of 5° from 90° to 140° and from 230° to 270°. From 140° to 230°, a step of 2° was chosen to capture the fading dips. The measurement was repeated two times at about 100 frequency points in 2.2 GHz to 2.4 GHz bandwidth in which the antenna was matched and the average S_{21} at these frequency points was calculated to average out any temporal variations. Fig. 2.7 shows the plots for the measured average S_{21}, S_{21} calculated from (2.1) by using $a = b = 10$ cm, and the FDTD simulated S_{21} for a numerical phantom of the same dimensions. A good agreement can be observed between these plots showing the capability of using the model for the circular phantom. The figure also shows the plot for S_{21} from the circular analytical model of [17]. It can be seen that the analytical model based on the circular assumption underestimates the link loss.

2.2.2 Influence of the Arms

In the above section, influence of the arms on the channel around the torso was not included in the analytical model. Usually, the arms are present at the

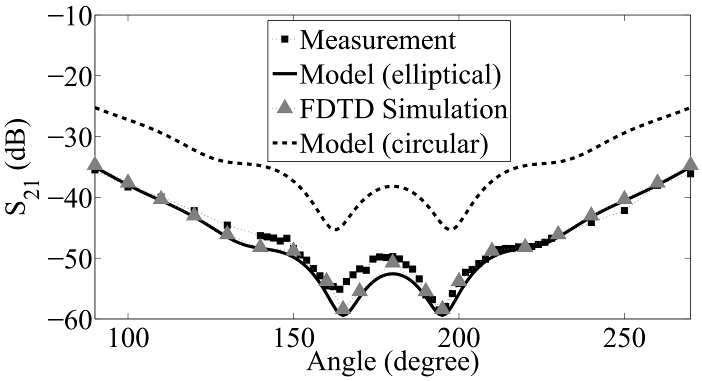

Figure 2.7: Comparision of the measurement, analytical models (elliptical and circular) and simulations for the channel around a semi-solid phantom.

sides of the torso and will influence the deterministic link loss. To investigate the influence of the arms on the propagation channel around the torso, we have considered four different arms positions in [88]. These are: (i) no arms at the sides of the torso (ii) one arm at a side of the torso (iii) both the arms at the side and (iv) arms folded. They are shown in Fig. 2.8. Fig. 2.9 shows the plots for the S_{21} $(-LL|_{\mathrm{dB}})$ around the torso when the transmit antenna is at the back and the receive antenna is moved along the front of the abdomen. It can be seen that the presence of both the arms can decrease the link loss by 6 to 8 dB. This is because the waves from the transmit antenna which get reflected from the arms, add up at the receive antenna, increasing the received power level. When only one arm is present at the side, the link loss is low at that side. Further, the positions of the fading dips also changes. The effect of folded arms on the link loss is minimal. This is because the contribution from the creeping waves above the antenna level is minimal and most of the power received by the receive antenna is from the creeping waves at the antenna level or from reflection, if the arms are present at the side. Due to the same reason, the influence of the whole body on the channel around the torso is minimal as shown in Fig. 2.10. Hence, a truncated model of torso for simulation can be used which has advantage in terms of faster simulation time. We can conclude that there is a significant influence of the arms on the propagation channel around the torso.

In [69] (Paper III), we extended the elliptical model of (2.1) to include the influence of the arms. The model is given by:

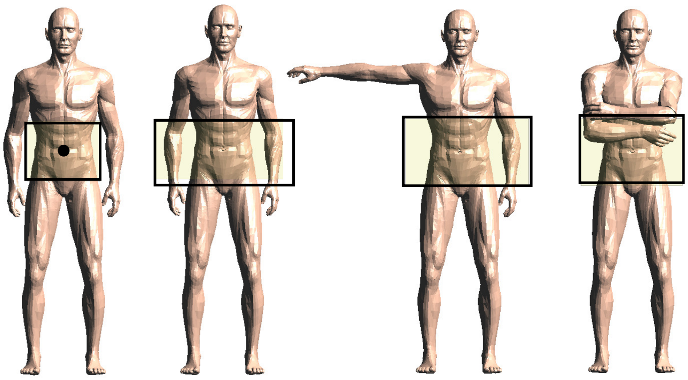

Figure 2.8: The four simulated pose of the POSER phantom to investigate the influence of the arms on the channel around the torso. The region included within the simulation domain is also shown.

$$
\begin{aligned}
LL_n\big|_{\mathrm{dB}} \quad = \quad & -10\log_{10}\Bigg[\frac{G_{RX}G_{TX}\lambda^2}{4\pi^2}\Bigg(\Bigg|\frac{e^{-L_{acn}}}{d_n}e^{-jkd_n}+\frac{e^{-L_{cn}}}{p-d_n}e^{-jk(p-d_n)} \\
& +\sum_{\jmath=\mathcal{L}}^{\mathcal{R}}\frac{\rho}{2\sqrt{2}}\frac{e^{-L_{\mathrm{TQ}_\jmath}}e^{-L_{\mathrm{P}_\jmath\mathrm{RX_n}}}\cos\gamma_\jmath}{t_{\mathrm{TXQ}_\jmath}+s_{\mathrm{i}\jmath}+s_{\mathrm{r}\jmath}+t_{\mathrm{P}_\jmath\mathrm{RXn}}} \\
& \times e^{-jk(t_{\mathrm{TXQ}_\jmath}+s_{\mathrm{i}\jmath}+s_{\mathrm{r}\jmath}+t_{\mathrm{P}_\jmath\mathrm{RXn}})}\Bigg|\Bigg)^2\Bigg] \qquad (2.2)
\end{aligned}
$$

The parameters of the model is described in Paper III.

The elliptical model with the arms was verified for two different positions of the transmit antenna and various arm positions in [69] showing that it is critical to include the effects of the arms for the channel around the torso. It was found that the reflected waves from the arms at an intended receiver position may interfere destructively with the on-body creeping waves resulting in a fading dip. Hence, the link loss at that receiver position was found higher than the link loss obtained without considering the arms. These results are discussed in Paper III.

2.2.3 Arm Movement Analysis

Arms swing during human gait is an important component for locomotion enhancing gait stability and decreasing the metabolic cost of walking [89]. There

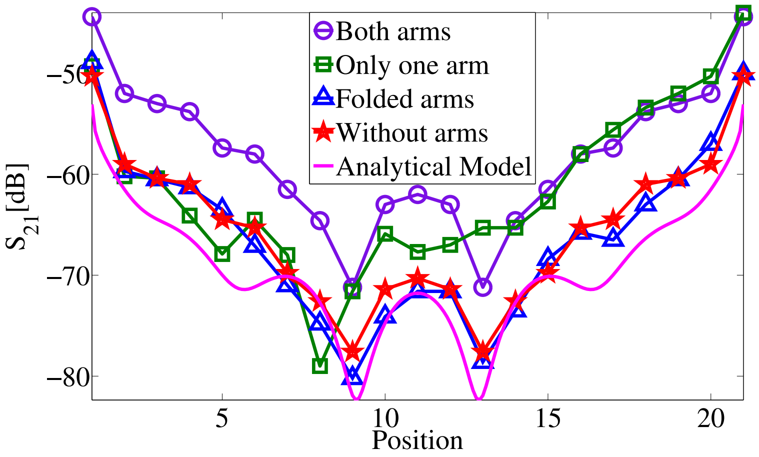

Figure 2.9: Variation of link loss for different positions of the arms around the torso [88].

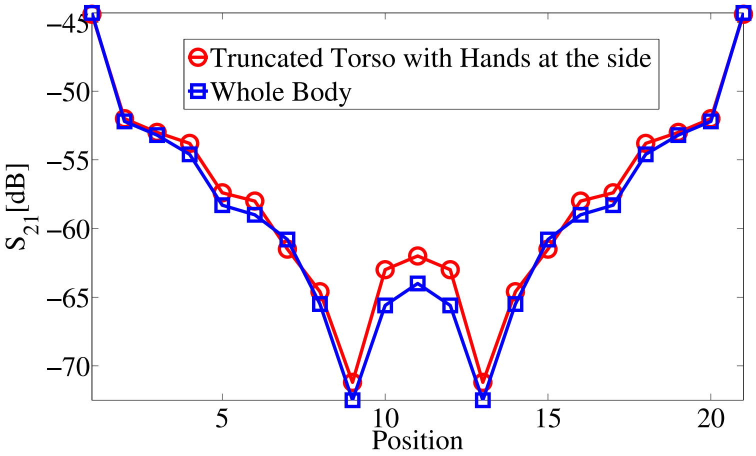

Figure 2.10: The link loss around the torso for the whole body and the truncated model. The difference between the two is minimal, and hence truncated model can be used for the investigation [88].

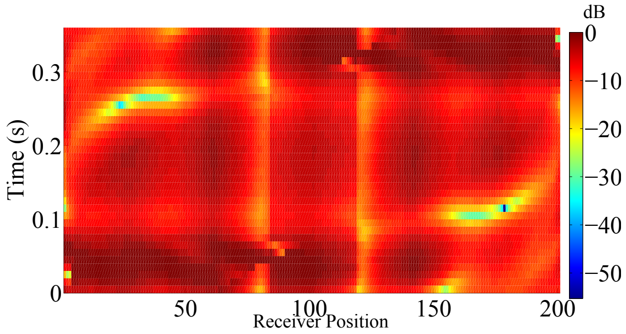

Figure 2.11: The temporal variation of the received power by the receivers for each arm in a symmetrical arms swing case.

is a rhythmic symmetric swing of the arms while walking and a high asymmetry in the arms swing can be an early sign for Parkinson's disease [90], [91]. Asymmetry in the arm swing means that one arm swing differently from the other arm, either in the swinging velocity or the swinging path. In [69], we showed that there would be a temporal variation in the received power by the sensors placed around the torso as the arms swing while walking (Fig. 2.11). At some of the positions of the receiver, this variation is high enough (around 22 dB) to detect the movements of the arms. We used this result for presenting an approach to analyze the movements of the arms while walking in [71] (Paper IV). For arm movement analysis, we placed a transmit antenna at the back of the torso and two receive antennas, one at the left side and other at the right side of the torso. For a symmetrical swinging of the arms while walking, the received power by the two receive antenna will be symmetrical and for asymmetrical case, it will be asymmetrical which was confirmed by the simulations on a walking phantom in the paper. Measurements were carried out on three human volunteers to confirm the variations in the received power for the symmetrical and assymentrical arms swing. The on-body antenna presented in [19], was used for the purpose. The transmit antenna was placed at the back of the volunteer and the receive antenna at the sides with the help of an elastic band. A string was further tied to guarantee minimal movement of the antenna from its position. The dimensions of the volunteers' waist level where the antennas were placed is given in Table. 2.2 where a is half of the waist-to-waist length, b is half of the abdomen-to-back length, and r is the radius of the volunteer's arm at the antenna level. All volunteers were male. The RUSK-LUND channel sounder [92] was used as a transmitter and a receiver. The transmit port of the sounder was directly connected to the transmit antenna.

The two receive antennas were connected to an RF switch and the switch output was connected to the receiver port of the sounder. The schematic of the measurement setup is shown in Fig. 2.12. The measurement was performed in $2.2 - 2.4$ GHz where the antennas have minimum mismatch loss. This is also the lowest frequency band supported by the sounder. As the objective of the measurement was to verify the symmetrical and asymmetrical movements, the volunteers were asked to stand still and only swing the arms. This also has an additional advantage as walking could have resulted in movement of the cables. The measurements were performed both in an anechoic chamber and in a corridor. Three scenarios were considered: (a) swinging of the both arms as in normal walking (symmetrical case) (b) only left arm swinging (right arm still, an asymmetrical case) (c) left arm normal swing and right arm swinging along a curved path (also an asymmetrical case). These scenarios are shown in Fig. 2.13. The volunteers were asked to pause momentarily after each cycle of the arm swing to distinguish between the cycles. A cycle starts when the left arm is forward and the right arm is backward and stops when left arm is backward and right arm is forward. A continuous measurement (without pause) was also done for the scenario (a) in the corridor. For all these scenarios, the normalized S_{21} ($-LL|_{\text{dB}}$) for the transmit antenna to each of the receive antennas is plotted. The normalization is done w.r.t. to the maximum S_{21} for each link. The normalized S_{21} in the anechoic chamber for the normal swinging of the arms for all the three volunteers is plotted in Fig. 2.14 and that for the corridor in Fig. 2.15. The results for the scenario (b) when the the right arm is still is shown in Fig. 2.16 for the anechoic chamber and in Fig. 2.17 for the corridor. Fig. 2.18 shows the results for the scenario (c) when the right arm is moving along a curved path when the measurements are done in the anechoic chamber and Fig. 2.19 presents the results for the corridor measurements. The measurement results for the continuos swinging of the arms for the corridor is presented in Fig. 2.20.

Table 2.2: Dimensions of the Volunteers

Volunteer	Age (year)	a (mm)	b (mm)	r (mm)
Volunteer 1	28	137.5	95.0	31.2
Volunteer 2	29	156.0	115.0	25.1
Volunteer 3	30	150.0	85.0	23.9

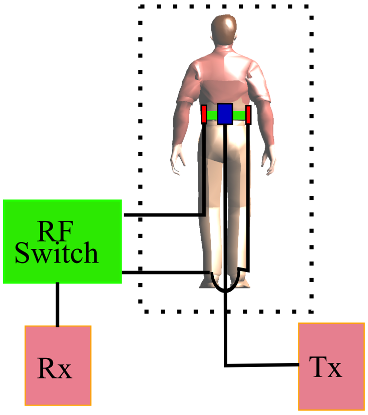

Figure 2.12: Measurement setup for measuring the power variation due to the arm movements. The dotted region is either anechoic chamber or corridor.

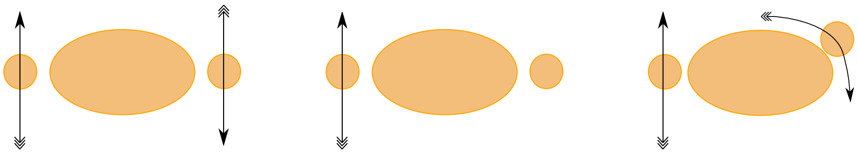
(a) (b) (c)

Figure 2.13: The different arm movements for the measurements. Different arrow heads show the direction in which the left and the right arm moves at one time (a) A normal swing of the arms when the arms swing in opposite direction (b) the left arm moves normally while the right arm is not moving (c) The left arm swing normally while the right arm along a curved path

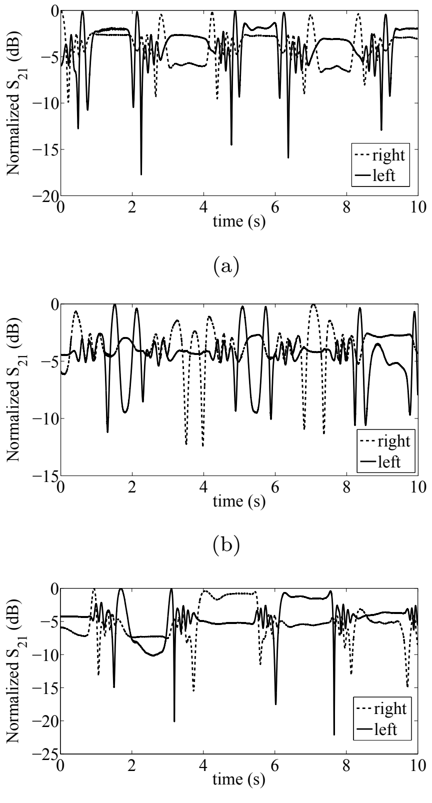

(a)

(b)

(c)

Figure 2.14: Normal Swinging of the arms in the anechoic chamber (a) Volunteer 1 (b) Volunteer 2 (3) Volunteer 3

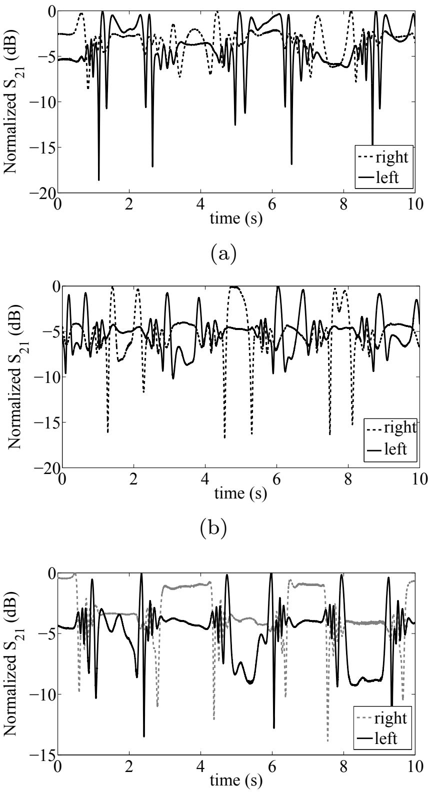

(a)

(b)

(c)

Figure 2.15: Normal Swinging of the arms in the corridor (a) Volunteer 1 (b) Volunteer 2 (3) Volunteer 3

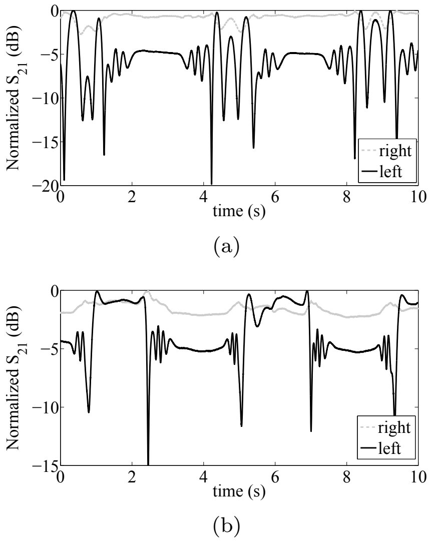

(a)

(b)

Figure 2.16: The left arm is swinging normally and the right arm is still in the anechoic chamber (a) Volunteer 1 (b) Volunteer 3. Please note that the data for the Volunteer 2 was erroneous and hence not shown.

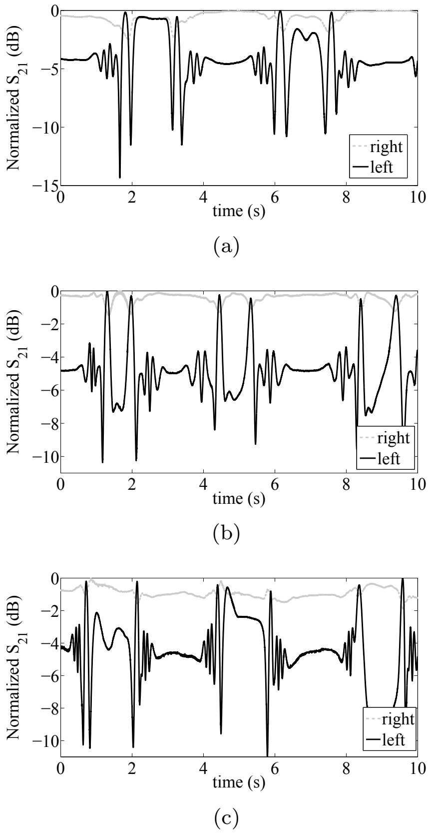

(a)

(b)

(c)

Figure 2.17: The left arm is swinging normally and the right arm is still in the corridor (a) Volunteer 1 (b) Volunteer 2 (c) Volunteer 3

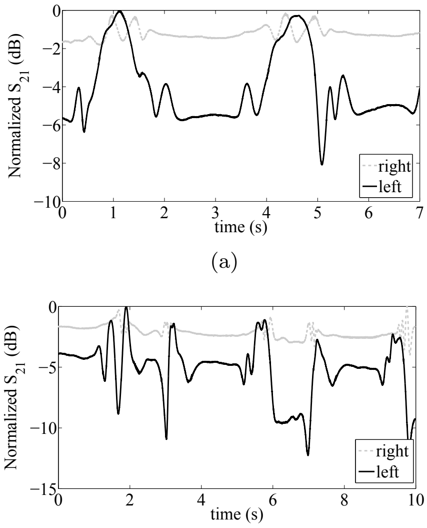

(a)

(b)

Figure 2.18: The left arm is swinging normally and the right arm moving in a curved path the anechaoic chamber (a) Volunteer 1 (b) Volunteer 3. Please note that the data for the Volunteer 2 was erroneous and hence not shown.

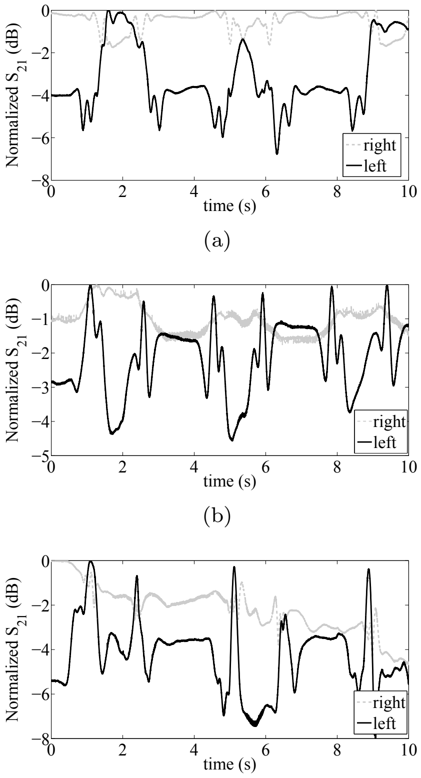

(a)

(b)

(c)

Figure 2.19: The left arm is swinging normally and the right arm moving in a curved path the corridor ((a) Volunteer 1 (b) Volunteer 2 (c) Volunteer 3

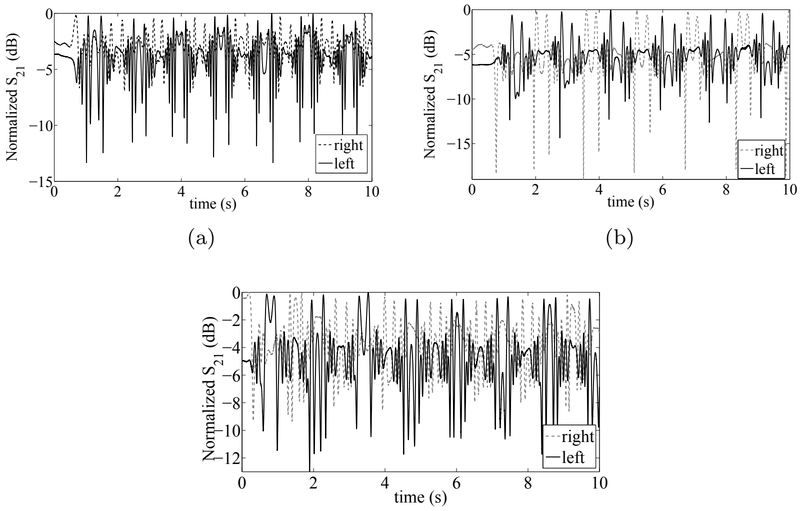

(a) (b)

(c)

Figure 2.20: Normal swinging of the arms without a pause between the different gait cycles in the corridor ((a) Volunteer 1 (b) Volunteer 2 (c) Volunteer 3

It can be clearly seen that for a normal swinging of the arms, the pattern of the received power variation for the arms is close to symmetry. It is not exactly symmetrical and hence it could be concluded that even for a normal swinging of the arms there is some degree of asymmetry in the received power. For the other two scenarios, a high degree of asymmetry can be observed. These measurements show that the normal swinging of the arms can be clearly distinguished from the cases when there is a high degree of asymmetrical movements of the arms. Hence, such a wearable system will be a simple solution for the analysis of the movements of the arms. It could comprise of a belt with three 2.45 ISM band transceivers that also record the RSSI and could be worn around the waist.

2.3 Wireless Capsule Endoscopy

This section is based on our work presented in [74].

Wireless capsule endoscopy (WCE) is a medical diagnosis procedure which has evolved due to wireless technology and miniaturization of the integrated circuits. It is used for diagnosing the gastrointestinal (GI) tract diseases by use of a swallowable pill like capsule containing a wireless transmitter and a camera. Basic organs of the GI tract through which the capsule passes is shown in Fig. 2.21. The camera captures images while the capsule passes through the GI tract and sends them to sensors located on the body. The received signals from all the sensors are recorded and processed to generate an image. Conventional wired endoscopy is done by inserting a long flexible tube through the mouth or the rectum, usually containing optical fibers to transmit light to illuminate the organ under inspection and view the interior through a lens system [93], [94]. This procedure may cause pain and discomfort. Moreover, due to the complex anatomy of the small intestine, the conventional wired endoscopy is incapable of reaching the entire small intestine [94]. Further, sedation may be required for the entire process. Hence, by use of the WCE, these limitations of the conventional wired endoscopy can be mitigated.

Localization algorithms are used to identify the position from where the images are captured inside the GI tract. With knowledge of the location from where the image was captured, therapeutic operation may be performed at the position of any abnormality, if it is detected. However, due to the heterogeneous and the lossy nature of the tissues and the complex anatomy of the GI tract, especially the small-intestine, localization of the capsule is a challenging task. The methods used for localization of the capsule endoscopes are usually based on magnetic field strength or EM waves as discussed in [94]. The main advantage of the localization methods based on magnetic field strength is that low frequency magnetic fields can pass through the body with low attenuation as tissues of the human body are non-magnetic. However, one challenge is

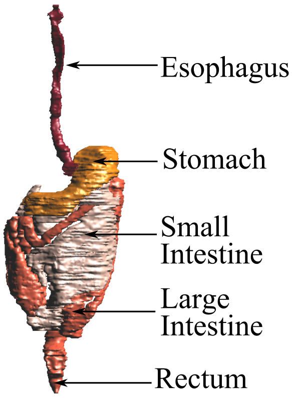

Figure 2.21: Basic organs in the GI tract of humans through which the wireless endoscopy capsule passes.

the interference from the magnetic field produced by material present in the surroundings and also from the earth's magnetic field, which may require additional equipment for the localization. On the other hand, an advantage of EM waves based localization is re-using the EM signal radiated by the capsule without any additional equipment. On the downside, high frequency EM waves have higher attenuation than the magnetic signal when they pass through the human tissues whereas low frequency EM waves have low precision of localization due to narrow bandwidth. Hence, a tradeoff has to be made between attenuation and the precision of localization by selecting a suitable frequency for EM waves.

Conventional methods of localization using EM signal for indoor or outdoor environments are either based on the received signal strength, angle of arrival (AOA), time of arrival or time difference of arrival. AOA methods are problematic due to the multipath components arising because of the complex environment inside the human body which includes several layers of heterogeneous lossy tissues, each having different electrical properties. On the other hand, time-based methods need strict time synchronization and high bandwidth for desired precision, which is hard to achieve in the MedRadio band (401-406 MHz). It could be used for UWB based localization [95]. Hence, localization methods based on the received signal strength indicator (RSSI) have been discussed in detail in the literature [96]-[103].

RSSI based methods use the received signal at different positions on the abdomen for localization of the capsule [97], [98]. Usually, a signal propagation model is used which relates the received signal strength with the distance between the in-body transmit antenna of the capsule and the receive antennas located on the body. After the distance of the transmit antenna from the receive antennas are estimated, a trilateration method is used to calculate the coordinates of the capsule. In [99], instead of using a propagation model, the authors used an algorithm based on a look-up table where an offline measurement on a phantom was carried for different positions of the capsule and stored in a look up table. Later on during the experiment, the RSSI was compared with the closest value in the look up table for the position estimation. There has been efforts to build a more accurate propagation model which does not only depend upon the distance but also the antenna orientation and tissue absorption as discussed in [100], [101]. Thus, the RSSI based methods need a propagation model which varies from person to person due to the complex radio wave absorption properties of human tissues [94].

In [74], we presented a localization method for the wireless capsule endoscopy based on the phase difference of the signal at different frequencies and a non-linear least square iterative method. The distance of the transmit antenna of the capsule from each of the receive antenna located on the body was calculated as following. The phase ϕ_i of the signal received at the ith receiver is given by

$$\phi_i = \phi_{ki} + \phi_{di}, \tag{2.3}$$

where ϕ_{ki} is the phase offset between the transmitter and the ith receiver, which is assumed to be constant, and $\phi_{di} = -\beta d_i$ is the phase of the signal after traveling through a distance d_i in the medium with phase constant β and effective relative permittivity ε_r and effective conductivity σ_e. The phase constant at frequency f of the medium is given by [105]

$$\beta = 2\pi f \sqrt{\frac{\mu_0 \varepsilon_0 \varepsilon_r}{2} \left(\sqrt{1 + \left(\frac{\sigma_e}{2\pi f \varepsilon_0 \varepsilon_r} \right)^2} + 1 \right)}, \tag{2.4}$$

where μ_0 is the permeability and ε_0 is the permittivity in free space. Substituting $\phi_{di} = -\beta d_i$ in (2.3) and differentiating w.r.t. frequency f, the first term ϕ_{ki} being a constant will vanish and we get

$$\frac{\mathrm{d}\phi_i}{\mathrm{d}f} = -d_i \frac{\mathrm{d}\beta}{\mathrm{d}f}. \tag{2.5}$$

Differentiating β w.r.t to frequency, the estimated distance $\hat{d_i}$ is given by

$$\hat{d_i} = -\frac{c}{\sqrt{2}\pi K \sqrt{\varepsilon_r}} \frac{\mathrm{d}\phi_i}{\mathrm{d}f}, \tag{2.6}$$

where d_i is approximated by the estimated distance $\hat{d_i}$, $c = 1/\sqrt{\mu_0 \varepsilon_0}$ is the speed of light in vacuum, and K depends upon a factor $P = 1 + \left(\frac{\sigma_e}{2\pi f \epsilon_0 \varepsilon_r} \right)^2$ and is given by

$$K = \sqrt{\sqrt{P} + 1} - \frac{P - 1}{2\sqrt{P(\sqrt{P} + 1)}}. \tag{2.7}$$

From (2.6), it can be seen that the estimated distance depends upon the slope of the phase of the received signal in the frequency domain. Once the distance to each of the receive antennas was estimated, a linear least square method was used to estimate a rough location of the capsule which was later refined using a non-linear least square method. This method was implemented on the noise free FDTD simulated data of a 2D homogeneous, a 2D heterogeneous, and a 3D homogeneous phantom. A cylinder was used as a homogeneous phantom and Billie was used as a realistic heterogeneous phantom. For all these simulated cases, localization accuracy within 1 cm was achieved. However, as pointed in the paper, this algorithm has certain limitations like the assumption of constant electrical properties of tissues. Further, noise is not taken into account which may affect the phase of the received signal, degrading the accuracy.

In Paper V, we present a localization algorithm based on microwave imaging or tomography which overcomes the above limitations. Microwave imaging is used to estimate the electrical properties of the body. It involves solving inverse EM problems to find the electrical properties of an object of interest by using the scattered electric field data. The basic setup for microwave tomography is shown in Fig. 2.22. Its details are explained in Paper V. Microwave imaging of biological bodies is well studied [106]-[111]. The algorithm is implemented on synthetic data obtained through FDTD simulations of heterogeneous phantoms for the 2D TM polarization. Additive white Gaussian noise is added to the synthetic data. A good accuracy in the cm range is obtained, showing the possibility of the algorithm to localize the capsule with a good accuracy even in the presence of noise.

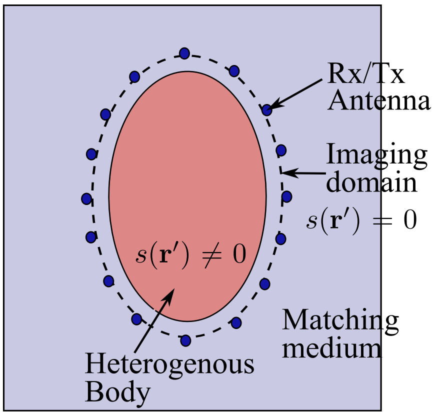

Figure 2.22: Basic setting for microwave tomography. The receive antennas and the transmit antennas are placed close to the heterogeneous body that has to be imaged. One antenna at a time transmits while all other antennas receive the electric field scattered by the body. There is an external matching medium outside the body which reduces the surface waves, reflection, and mutual coupling between the antennas. $\mathbf{r}'$ is any position inside the imaging domain. s is difference between the wave number at position $\mathbf{r}'$ and wave number in the external medium.

2.4 Antenna for In-mouth Tongue Controlled Devices

Part of this section is based on our work presented in [112].

Spinal cord or brain injury may result in paralysis of the limbs and the torso affecting patients with movement disabilities. These patients may have to depend upon someone else for moving a wheelchair or using a computer. Fortunately, for such patients, the tongue muscle is not affected and could be used for controlling a device placed inside their mouth. These tongue controlled devices can be interfaced with either the wheelchair or a computer [24], [113]. The devices are placed inside the mouth and ought to be wireless for the ease of control and maintenance, and thus, the antennas in such devices play a critical role. They typically use 2.45 GHz ISM band for the communication. The in-mouth tongue controlled devices are different from the on-body or the implant devices as these are placed inside the human body but are not surgically implanted. These devices could described by the term semi-implantable devices. The presence of lossy tissues of the tongue, the inner-mouth and the teeth will affect the performance of the device and the antenna in a similar way to actual implanted devices. Waves propagating from an antenna in the mouth to an external antenna will undergo losses because of the reflection, the scattering, the absorption and the path-loss. A very simple model for a mouth can be described in terms of the layered tissue which consist of the layer of the teeth, the muscle, the connecting tissues, the fat and the skin as shown in Fig. 2.23. There will be reflections at each of these tissue interfaces, and absorption in the tissues.

For in-mouth device scenario at 2.45 GHz, the receiver located on a wheelchair or a PC, is usually in the far-field of the antenna. In such scenarios, complete body can be treated as an antenna radiating to free space. The in-mouth antenna characteristics can be defined as a ‘super-antenna’ consisting of the sum of the in-mouth antenna and the body. The received power

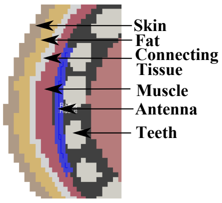

Figure 2.23: Arrangement of different tissue in the mouth. The in-mouth curved dipole antenna is shown with blue color.

by an external antenna from the in-mouth antenna at the distance d can be calculated using the Friis formula:

$$P_{RX} = P_{TX} G_{TX} G_{RX} \left(\frac{\lambda}{4\pi d} \right)^2 , \tag{2.8}$$

where the transmitter gain (G_{TX}) is the gain of the super-antenna (in-mouth antenna including the body).

In [112], we presented a dipole antenna which was curved to fit the curvature of the teeth as shown in Fig. 2.23. The vertical length of the antenna is 21.8 mm which is 64% reduction of the length when compared with the free-space half-wavelength dipole at 2.45 GHz. The radius of the wire was 0.3 mm. The curved dipole was insulated with 0.5 mm thick insulator of permittivity 3.1. The length of the dipole was optimized for minimal return loss in 2.45 GHz ISM band by placing the antenna in front of the teeth with the mouth closed. The placement behind the teeth was also investigated. Both open and closed mouth scenarios were considered. The investigations were done by placing the antenna inside the Duke mouth and only the head was considered in the simulation domain. As the movement of the mandible is not possible in this phantom, an open mouth was realized by overwriting the tissues below the upper jaw by a block having electrical properties of the air as shown in Fig. 2.24. The block was 63 mm deep into mouth with 15 mm height and 50 mm width.

As expected, it was found that the resonance of the antenna shifts depending whether it is placed behind the teeth or in front of the teeth or whether the mouth is open or closed as shown in Fig. 2.25. Moreover, the gain of the antenna also changes with lowest being when it was placed behind the teeth with mouth closed as can be seen from Fig. 2.26. This is the gain of the super-

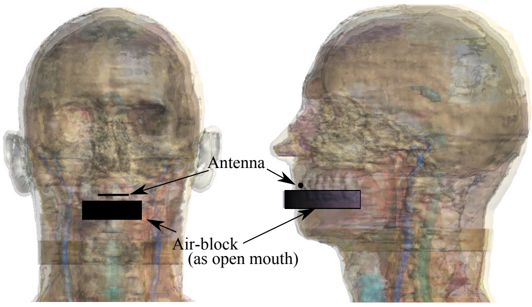

Figure 2.24: Implementation of open-mouth on a static phantom by using an air-block to overwrite the tissues.

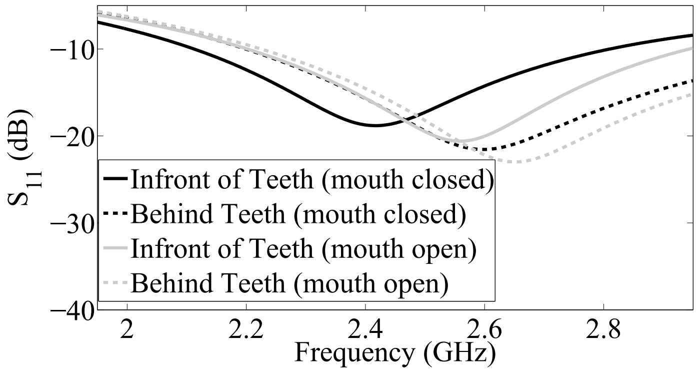

Figure 2.25: Variation in the S_{11} of an in-mouth dipole antenna with open and closed mouth and on the placement of the antenna.

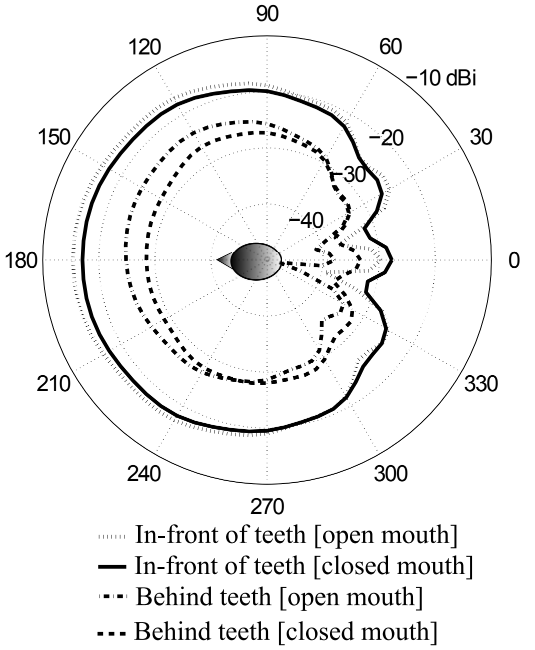

Figure 2.26: Gain of the in-mouth dipole antenna in the transversal plane.

Table 2.3: Theoretical vs. Simulated Link Loss between the in-mouth antenna and an external dipole antenna at 2.45 GHz at 400 mm from the center of the head

Scenario	Friis Formula* (dB)	Simulated (dB)
In front of Teeth-Closed Mouth	-44.9	-44.9
In front of Teeth-Open Mouth	-43.0	-43.7
Behind-the-Teeth-Closed Mouth	-56.0	-56.6
Behind-the-Teeth-Open Mouth	-52.4	-52.8

*with the simulated gain

antenna which includes the head. The gain for different cases along with the link loss calculated by (2.8) and the simulation is shown in Table 2.3. The external receiver is a half-wavelength dipole antenna placed at about 400 mm from the center of the head (287 mm from front of the head). It can be seen that the Friis formula and the simulations agree very well and hence the link loss at any other distance can be easily estimated from the Friis formula with the simulated gain. For in-front of the teeth placement, opening the mouth decreases the link loss by 1.2 dB and for the behind the teeth placement it decreases by 3.7 dB. It should be noted here that the mouth is open to a certain level only and hence opening the mouth more or less than in simulation will change the result. The variation is largely because of the gain variation in the different scenarios. The link loss for the in-mouth antenna placement in front of the teeth is lower than the behind the teeth placement for both open and closed mouth. However, in-front of the teeth placement is not a better placement position if other factors are considered. For example, for the device in [114], which is attached to the maxilla, behind the teeth placement is a good choice because placing the antenna in front of the teeth will involve extra clamps and wires going around the teeth. Behind the teeth placement is also better if cosmetics and patient's integrity is considered. Thus, there has to be trade-off between the link loss requirement and the ease with which device can be mounted inside the mouth.

2.4.1 Comparison Between a Monopole and a Loop antenna for In-mouth Applications

A monopole antenna and a loop antenna was designed for an in-mouth device presented in [114]. The antenna was optimized in SEMCAD-X for good matching in the 2.45 GHz ISM by placing it inside the SAM phantom near it's mouth. The average tissue property of the head $\varepsilon_r = 39.2$ and $\sigma_e = 1.8$ S/m is considered. The antenna was encapsulated within a lossless material having the shape and size of the actual in-mouth device. A battery which was realized with a PEC box in the simulations was also included and placed at its position inside the encapsulation. The design and the dimensions of these two antennas are shown in Fig. 2.27. A 15 cm thin semi-rigid coaxial cable with an SMA connector was soldered to the antenna for feeding. The fabricated antennas were placed inside a plastic casing fabricated by 3D printing. Epoxy resin was then poured in the casing which encapsulated the antenna once the epoxy got solidified. The fabricated antenna is shown in Fig. 2.28.

The simulated and the measured S_{11} of the antennas are shown in Fig. 2.29. The measurement was done by placing the antenna inside the mouth of a person. A calibration kit with the same length of the feeding cable was fabricated

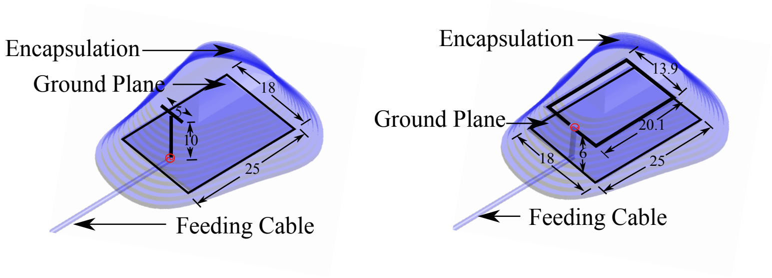

(a) (b)

Figure 2.27: Design of the (a) Monopole antenna (b) Loop antenna. The dimensions shown is in mm.

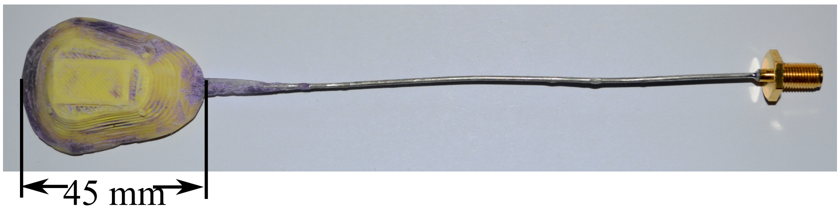

Figure 2.28: Top view of the fabricated encapsulated antenna. The yellow plastic is the casing in which epoxy-resin was filled. The semi-rigid feeding cable is also shown.

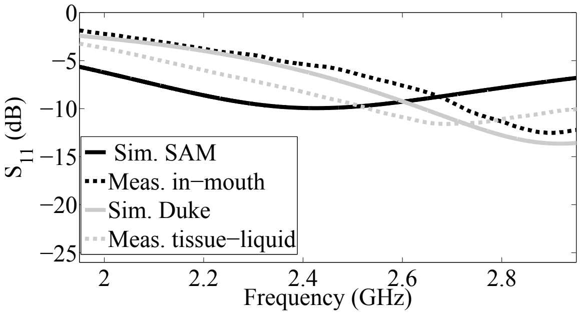

(a)

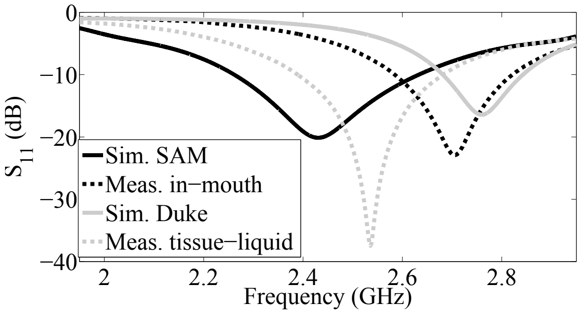

(b)

Figure 2.29: Simulation vs. measurement of the S_{11} of (a) the in-mouth monopole and (b) the loop antenna.

to remove any effect of the cable on the impedance matching. A shift in the resonance frequency of the antennas can be observed for the measurement. The reason for this shift is that the antennas were optimized inside a homogeneous phantom in simulation whereas the measurement was done on an actual human where the antenna surrounding consists of several layers of the tissue with different electrical properties. This was verified by placing the antennas inside the mouth of the Duke phantom which also resulted in the shift of the resonance frequency towards a higher frequency (shown in Fig. 2.29). The S_{11} of the antennas were also measured by placing them inside a container filled with the homogeneous tissue stimulating liquid discussed in Section 1.4.4 having $\varepsilon_r = 39.2$ and $\sigma_e = 1.8$ S/m. As can be seen from the figure, the loop antenna has lower mismatch loss than the monopole antenna. The measured S_{11} in the

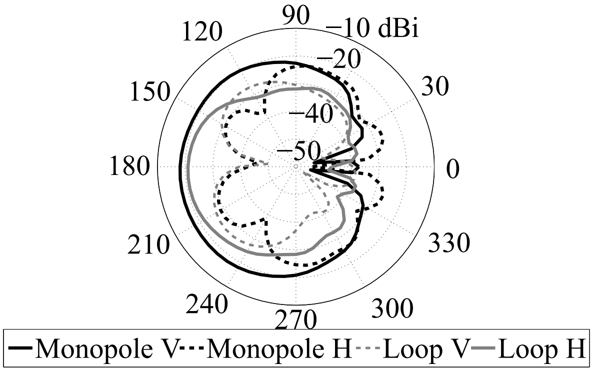

Figure 2.30: Gain pattern of the antennas when placed inside mouth of the Duke phantom. The vertical polarization (w.r.t. the ground) is dominant for the monopole antenna and the horizontal polarization for the loop antenna.

tissue stimulating liquid is closer to the SAM phantom. Some difference might occur due to electrical properties of the epoxy resin which in the simulation were taken as $\varepsilon_r = 3.5$ and $\sigma_e = 0$ S/m [115].

The gain pattern of the antennas in the transversal plane when placed in the mouth of the Duke phantom at 2.45 GHz is shown in Fig. 2.30. As expected, the vertical polarization (w.r.t. to the ground) is dominant for the monopole antenna and the horizontal polarization for the loop antenna. Further, the monopole antenna has higher gain than the loop antenna. The maximum gain of the monopole antenna is about −18 dBi and that of the loop antenna is −21 dBi. Although the gain here is shown at 2.45 GHz, higher gain of the monopole antenna than the loop antenna was also observed at other frequencies.

The transmission characteristics of the antennas were investigated by placing them inside the mouth and measuring S_{21} between the in-mouth antenna and an external monopole antenna through a VNA. The external monopole antenna has a good matching ($S_{11} \leq -10$ dB) in the 2.45 GHz ISM band and $S_{11} \approx -5$ dB around 2.65 GHz where both the fabricated antenna had good matching when placed in the mouth. The feeding cable which is connected to the antenna might have some leakage current. However, as some length of the cable passes between the lips and are also in contact with the tongue, the leakage current will attenuate due to contact with the lossy tissues, with a low influence on the results. This was verified through simulations where the feeding cable was attached to the antenna and the current on the cable was found to be minimal. Moreover, the difference in the simulated far-field gain, with and without the cable, were also minimal. The external antenna was attached to a

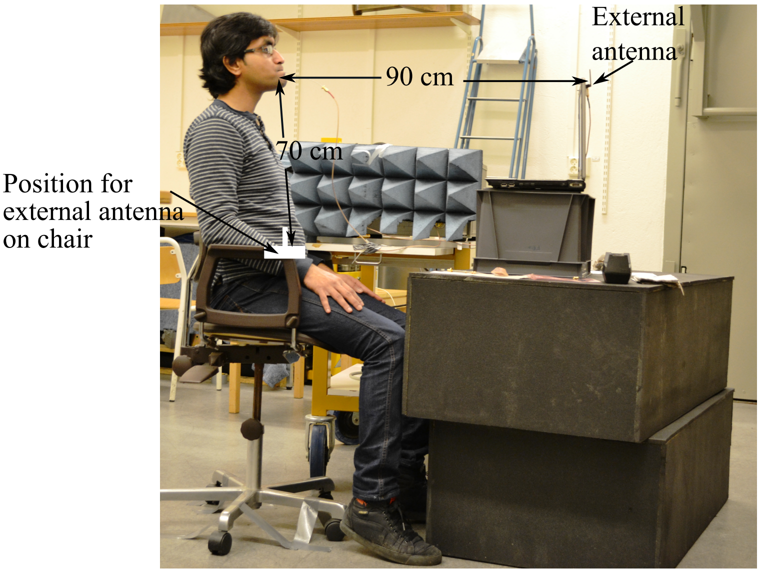

Figure 2.31: Indoor Setup for measurement of S_{21} between the in-mouth antenna and an external antenna placed on a laptop or on the chair.

laptop and a chair. These scenarios mimic the actual use-case of the in-mouth applications. The link was measured for both the vertical and the horizontal polarization of the external monopole antenna. In the horizontal case, the external antenna was placed parallel to the torso. The measurements were done in a laboratory as well as in an anechoic chamber. The measurement setup is shown in Fig. 2.31. For both of the links, the person with the antenna in the mouth was looking parallel to the ground. For the in-mouth-chair link, the laptop was removed from the measurement setup. The measurements were done with the closed mouth (a worst case scenario as discussed earlier in the previous section) and care was taken to remain stable while the measurement was ongoing. The shortest distance between the mouth and the laptop antenna was 90 cm and that between the mouth and the chair antenna was 70 cm. As the monopole antenna and the loop antenna have different matching, for a proper comparison of the measured S_{21}, we follow the procedure discussed in [116] for removing the mismatch loss in the measured bandwidth. The results are shown in Fig. 2.32.

For the in-mouth-laptop link both in the anechoic chamber as well as in the laboratory, the measured S_{21} is high for the polarization of the external antenna which is dominant for the respective in-mouth antennas, i.e. the vertical

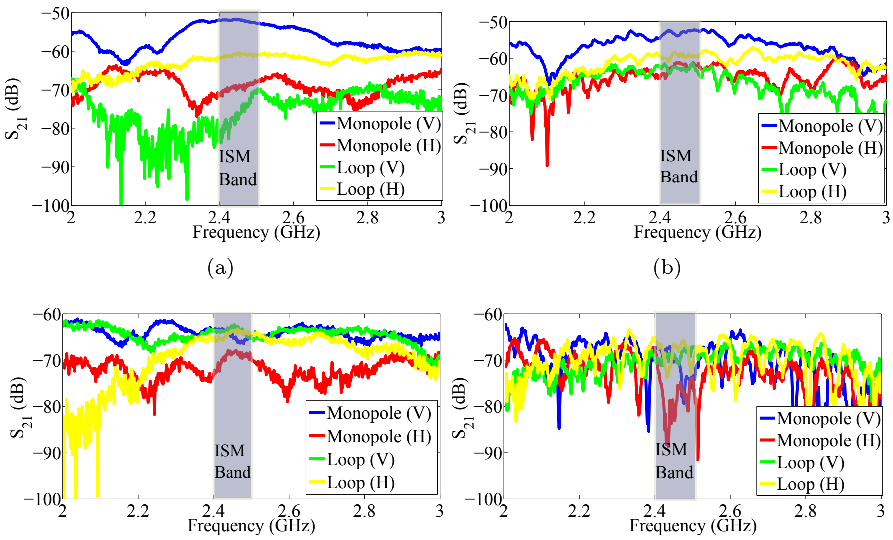

(a) (b) (c) (d)

Figure 2.32: Measured S_{21} for the in-mouth-laptop link: (a) in an anechoic chamber (b) in a laboratory, and for the in-mouth-chair link: (c) in an anechoic chamber (d) in a laboratory. V: vertical polarization of the external antenna, and H: horizontal polarization of the external antenna.

polarization for the monopole antenna and the horizontal polarization for the loop antenna. Further, the measured S_{21} for the in-mouth-laptop co-polarized link (the external antenna is vertical for the monopole antenna and horizontal for the loop antenna) is higher for the monopole antenna than the loop antenna. This is due to higher gain of the monopole antenna for the vertical polarization than the loop antenna for the horizontal polarization, as shown earlier. In the band of interest ($2.4 - 2.5$ GHz), the co-polarized link loss ($-S_{21}|_{dB}$) is around 54 dB for the monopole antenna and around 62 dB for the loop antenna. For the cross-polarization in-mouth-laptop link (the external antenna is horizontal for the monopole antenna and vertical for the loop antenna), the link loss is high (about 70-80 dB) but still about $15 - 20$ dB low than the mean noise level of the VNA which is around 93 dB with 5.7 dB standard deviation. The noise was measured when no antenna is connected to the ports of the VNA.

The in-mouth-chair link is a scenario where the direct link from the mouth to the external antenna is partially shadowed by body parts such as the chest and the hand resulting in higher link loss. Moreover, the gain in the direction of this link is lower than the in-mouth-laptop link, which was confirmed from the 3D gain pattern. Changes in the torso dimension while breathing may also result in variations in the S_{21}. The link loss between the in-mouth loop antenna and the external antenna is almost same in the band of interest (about -65 dB) for both co-polarized and cross-polarized in-mouth-chair link in the anechoic chamber. However, for the monopole antenna, for the co-polarization case, the link loss is about 65 dB whereas for the cross-polarization case it is about 75 dB which may be attributed to the difference in the gain of the monopole antenna in these two polarizations. These behaviors are also observed in the indoor scenario. However, the effect of the multi-path components resulting in fading dips can be observed for the indoor scenario.

Hence, with a proper polarization of the external antenna attached to a computer or a chair, both the in-mouth antennas are suitable for in-mouth devices. However, the monopole antenna outperforms the loop antenna especially when the external antenna is in front of the mouth as in the in-mouth-laptop link.

In Section 1.3.1, it was discussed that a purely magnetic antenna is more efficient than a purely electrical antenna with thin insulation. Furthermore, for a self-resonating antenna both the electrical and the magnetic components of the field radiate. A self-resonating monopole antenna is a *more* electrical whereas a self-resonating loop antenna is a *more* magnetic. We found that for the in-mouth-laptop link, the monopole antenna performed better than the loop antenna. Further, the resonance frequency of the monopole antenna was found to be sensitive to the placement inside the mouth whereas that of the loop antenna was more or less stable.

Chapter 3

Contributions, Conclusions, and Future Work

This chapter presents an overview of the included papers in this thesis. The results and contributions to the research fields discussed in the previous chapters are also presented for each included paper. The chapter is concluded with general discussions and some thoughts for possible future work.

My personal contributions to the papers in all cases constitute the main participation in producing the paper, i.e. doing background studies, development of analytical models and algorithms, implementation and simulations, measurements, analyzing and accounting for results and conclusions, and writing the papers. My supervisor and co-authors have provided me valuable inputs during the process.

3.1 Included Papers

3.1.1 Paper I: Miniaturized antennas for link between binaural hearing aids

In this paper, the possibility of the ear-to-ear propagation link at 2.45 GHz for the binaural hearing aids is investigated using miniaturized antennas. Design of the antennas suitable in size and performance for in-the-ear (ITE) placement, and in-the-canal (ITC) placement is presented. The ear-to-ear link loss is calculated using FDTD simulations for these two placements on a modified SAM head where simple model of the ear canals is included.

The small size of a modern hearing aid puts a stringent constraint on the size of the antennas. The antennas are miniaturized by applying disc loads and high permittivity materials. The ITE antenna is enclosed in a volume of 20 mm × 20 mm × 19.5 mm and the ITC antenna in 7 mm × 7 mm × 11 mm. The return loss of the ITE antenna when placed in the ear is 15 dB and that of the ITC antenna is 11 dB and hence the antennas are well matched with a minimal mismatch loss. The ear-to-ear link loss for the ITE case is found to be 48 dB and that for the ITC case is 92 dB.

Main conclusions:

- Design of two antennas suitable in size and technical performance for the ITE and the ITC type of hearing aids were presented and the ear-to-ear link loss were calculated. With these calculated values of the link loss, the investigation suggests that it is possible to establish a wireless communication link between the binaural hearing aids using miniaturized antennas at 2.45 GHz.
- The communication between the antennas for the ITE placement mainly takes place through the creeping waves over the head surface resulting in a low link loss whereas the communication between the antennas for the ITC placement takes place through the lossy tissues of the head resulting in a high link loss. However, the creeping waves leaking out of the ear canal also contribute for the ITC placement.

Scientific Contribution: We showed the feasibility of using 2.45 GHz for communication between binaural hearing aids using miniature antennas.

3.1.2 Paper II: A Link Loss Model for the On-body Propagation Channel for Binaural Hearing Aids

In the previous paper it was found that the link loss for the ITE case is lower than the ITC case and hence a detailed investigation is done for the ITE case in this paper using heterogeneous phantoms. Moreover, an analytical link loss model is developed for the ear-to-ear propagation channel, which is then verified on different heterogeneous phantoms of different age groups and head sizes. Various factors that could affect the ear-to-ear propagation channel are also investigated.

The ear-to-ear link loss is an important factor in the link budget to decide the necessary sensitivity of the wireless binaural hearing aids for a reliable link. In the previous paper, the link loss calculation was done through simulations on the homogeneous modified SAM phantom. In this paper, heterogeneous phantoms from the virtual family and classroom project are used to calculate the ear-to-ear link loss. Using the ITE antenna optimized for the Duke phantom resulted in 49 dB ear-to-ear link loss for the SAM phantom. However, the link loss for the Duke phantom is found to be 79 dB which is 30 dB higher than the SAM phantom. Apart from the difference in the dimensions of the head of the SAM phantom and the Duke phantom, two other main factors for this large difference in the link loss are found. They are: (1) presence of the outer ears called pinna in the Duke phantom which is absent in the SAM phantom and (2) the presence of the outer lossy skin on Duke whereas the SAM phantom has an outer lossless shell. The effect of these two factors are verified by changing the outer lossless shell of the SAM phantom with the electrical properties of that of the SAM liquid, and introduction of a simple model of the pinna. With these changes, the link loss for the SAM phantom approached the link loss of the Duke phantom. Further, a reverse verification is done by removing the pinna and introducing a lossless shell in Duke. This resulted in a link loss close to that of the SAM phantom. The effect of the pinna in increasing the link loss is verified through measurement on a phantom where the pinnas manufactured by 3D printing were attached.

It is found that the two paths of the creeping waves, clockwise and anti-clockwise from the antenna in one ear to the antenna in the other ear is sufficient to describe the link loss, as these two paths carry most of the power. This is verified through six different simulations on the Duke phantom by blocking the creeping waves in some paths and allowing them in other paths. An analytical model for the ear-to-ear link loss is developed based on the attenuation of the creeping waves on these two paths over an elliptical cross-section of the head which takes into account the losses due to the pinnas. This analytical model is verified on Duke, Ella and Billie through finite-difference-time-domain (FDTD) simulations. Further verification is done by increasing and decreasing the head size of Duke and Billie by 10% in the 2.45 GHz ISM band. In all these cases, a good agreement between the analytical model and the simulation is obtained.

Main conclusions:

- Any phantom, numerical or physical, with an outer lossless shell underestimates the on-body link loss for the devices located on the opposite side of the body as in binaural hearing aids system. Hence, a lossless shell phantom should be used with caution for estimating the link loss for around the body propagation.
- Pinnas (outer ear) should be included for a more realistic estimation of the ear-to-ear link loss.
- The shoulders have minimal influence on the ear-to-ear link loss. Hence, a truncated head phantom can be used for estimating the link loss through the simulations. This helps in reducing the simulation time.

- The developed analytical link loss model has dimensions of the head as parameters and hence can be used to estimate the ear-to-ear link loss for any head size. This estimation of the link loss from the developed model is computationally more efficient than FDTD simulations.

Scientific Contributions: We identified the need of a proper phantom, having outer lossy shell and pinnas, for an accurate calculation of the ear-to-ear link loss. We developed an analytical model for calculating the ear-to-ear link loss that is computationally more efficient than FDTD simulations.

3.1.3 Paper III: An Analytical Link-Loss Model for On-Body Propagation Around the Body Based on Elliptical Approximation of the Torso With Arms' Influence Included

There are scenarios for wireless body area networks where the sensors are located around the torso. For such cases the calculation of the link loss is necessary for the link budget. Further, the arms present around the torso can influence the wireless propagation. In this paper, an analytical model for estimating the link loss for the on-body wave propagation around the torso is presented. The model is based on the attenuation of the creeping waves over an elliptical approximation of the human torso and includes the influence of the arms. Various positions of the arms, receive antenna and the transmit antenna is considered for the verification of the model through FDTD simulations of a phantom. A good agreement is obtained between the simulation and the analytical model.

Main conclusions:

- Torso should be modeled with an elliptical cross-section rather than a circular cross-section for more accurate estimation of the link loss. An analytical model for estimating the link loss for sensors placed around the torso is developed which takes into account the presence of the arms and is based on attenuation of creeping waves over an elliptical cross-section of the torso.

- The results presented in the paper show that it is critical to include the effect of the arms while estimating the link loss as the reflected waves from the arms at an intended receiver position might interfere destructively with the on-body creeping waves. Hence, the link loss at that receiver position will be higher than the link loss obtained without considering the effect of the arms.

- Arms swing during walk result in a temporal variation in the received signal by the receive antennas placed around the torso.

Scientific Contribution: We highlighted the importance of including the influence of the arms for determining of the link loss for devices placed around the body. We developed an analytical model based on the elliptical approximation of the torso which can calculate the link loss in such cases in computationally more efficient way than FDTD simulations.

3.1.4 Paper IV: An Approach to Analyze the Movements of the Arms while Walking using Wearable Wireless Devices

In the previous paper it was shown that the arm movements during walking will result in a temporal variation of the signal received by the sensors placed around the torso. This result is exploited in this paper to present an approach to analyze the movements of the arms while walking, by using three wearable wireless devices placed around the torso. One of the devices is a transmitter placed at the back and the other two are symmetrically placed receivers at the side of the torso that record the power variation due to movements of the arms while walking. It is shown that the power received will have a symmetrical variation if the arm swing is symmetrical. The analytical model developed in the previous paper is used to find the placement positions of the receivers where the variation in the power level is high enough to distinguish the arm movements. FDTD simulations on different pose of a walking phantom are done to confirm the results.

Main conclusions:

- The symmetry of the arm movements while walking can be analyzed by placing three wearable wireless devices around the torso at appropriate locations.
- There is a symmetrical variation in the received power by two antennas for a normal swinging of the arms while walking, if the transmit antenna is placed at the back and the receive antennas are symmetrically placed at the sides of the torso.
- The variation in the received power is asymmetrical if there is a high degree of asymmetry in the arms swing while walking.

Scientific Contribution: We proposed a simple approach to analyze the arm movements using three wireless wearable devices that can be included in a single belt worn around the torso.

3.1.5 Paper V: A Microwave Imaging based Technique to Localize an In-body RF-Source for Biomedical Applications

In this paper, a localization algorithm for an in-body RF source as in wireless capsule endoscopy (WCE) is developed, which works with a good accuracy even in the presence of noise. One of the challenges in the localization of the capsule endoscope is obtaining the electrical properties (relative permittivity and conductivity) and the distribution of the tissues through which the capsule is traveling for a better localization accuracy. Magnetic resonance imaging (MRI) or CT-scan can be used for this purpose. However, MRI scan is not a cost-effective solution whereas CT-scan uses x-rays which may harm the tissues. A cost effective alternative, microwave imaging or tomography, is used in this paper to obtain the electrical properties. The developed algorithm is applied at 403.5 MHz on synthetic data obtained from FDTD simulations of heterogeneous phantoms in the 2D-TM polarization. White Gaussian noise is added to synthetic date to make it more realistic. The calculated root mean square (RMS) of the error distances (distance between the estimated and the true position) for various positions of the transmit antenna is found within 1 cm for the phantoms.

The low value of the RMS of the error distances shows that the algorithm can be used to localize the capsule within a centimeter range. The main benefits of the developed algorithm are that: (a) it does not depend on a signal propagation model which is difficult to standardize for different people having different anatomies and tissue thicknesses (b) it uses microwave imaging for determining electrical properties (c) the same setup which is used for the capsule endoscopy can be used for the microwave imaging.

Main conclusions:

- An algorithm for the localization of an in-body RF-source as in wireless capsule endoscopy using EM waves at 403.5 MHz is developed.
- Microwave imaging is used to determine the electrical properties and the distribution of the tissues, and the position of an RF-source is then estimated based on the image.
- The algorithm is implemented on FDTD simulated data of heterogeneous phantoms in the presence of white Gaussian noise in the two dimensional case with a localization error within 1 cm.

Scientific Contribution: We introduced the use of microwave imaging as a part of a calibration process for the localization of an in-body RF-source.

3.2 Conclusions

The results presented in this thesis will be beneficial to WBAN engineers and researchers for understanding antennas, wave propagation, and localization in different WBAN applications. The discussions regarding antennas for hearing aids will help antenna engineers designing antennas suitable for hearing aids. The developed analytical model for the link loss in a binaural hearing aid system will guide engineers to design a reliable wireless link between the hearing aids. The use of a phantom with a lossy outer shell and pinnas for proper calculation and measurements of the ear-to-ear link loss was also emphasized. Researchers working with analysis of arm movements can benefit from the approach using wireless wearable devices and the measurements presented in the thesis. The analytical model of wave propagation around the torso that includes the arms influence can help them to know how the signal propagates around the torso, and how it is affected by the arm movements. The model can also be used to find proper placement positions of sensors located around the torso for a reliable communication between two such sensors. Wireless capsule endoscopy is becoming a popular method for endoscopy. The algorithms developed in this thesis give an insight on localization methods that do not use a pre-defined signal propagation model. These algorithms could be further developed for use in a real capsule endoscopy system. The investigations regarding the in-mouth antenna suggest that it is possible to establish a wireless link between an in-mouth device having a small antenna to a receiver placed on a chair or a laptop at 2.45 GHz.

3.3 Future Work

Completed research projects always open a door for future research. The research work in the field of antennas, wave propagation and localization in WBANs done in this thesis also provides new opportunities.

The work done in this thesis is mostly for the ITE placement of the binaural hearing aids with some insight on the ITC placement. Further research can be done for the ITC and the BTE placement. As the loss through-the-head path is higher than the over-the-head creeping paths for the ear-to-ear propagation channel, an antenna for the ITC case which minimizes the radiation towards the head can be designed. For such an antenna, the communication between the hearing aids should be mostly through the waves leaking out of the canal and then creeping over the head surface. This may reduce the ear-to-ear link loss for the ITC placement. The simulations suggested that two paths of creeping waves, one going over behind the head and other going over front of the head, at the level of the ears, carry most of the power. Hence, future research on design of an antenna such that it has maximum radiation along these two paths and minimal radiation along all other paths is also a possibility.

For the arm movements' analysis, measurements were done to verify the symmetry of the arm movements. One motivation for doing this analysis is that a high degree of asymmetric arm movements can be an early sign of the Parkinson's disease. The measurements were done on healthy volunteers who were asked to swing the arms symmetrically or asymmetrically. Future work in this regard would be to design a belt which can be worn around the waist, comprising of three wearable transceivers at the proper positions which records the received signal strength. Measurements can be done using the belt on several subjects, both patients with Parkinson's disease, and healthy volunteers, to record the variations in the received signal by the transceiver while they are walking. Based on these measurements, a statistical index could be developed which can quantify the asymmetry in the arm movements while walking.

For the wireless capsule endoscopy, the developed algorithm was implemented for 2D cases. It can be extended to 3D case as a future work by series of 2D measurements or using a 3D microwave imaging technique. In the developed algorithm we used a large number of on-body antennas for receiving the signal. Optimizing the number of antennas which can reduce the total number without affecting the precision of localization should also be done. Validating the algorithm through measurements is the next step. A further step is to test the localization algorithm in a real wireless capsule endoscopy system.

The in-mouth antenna could be implemented in an actual in-mouth device and measurements can be performed with a patient in a wheelchair. Several measurements can then be done in different indoor and outdoor environments for measuring the statistical performance of the antenna and the link.

References

[1] "World Population Ageing: 1950-2050," A Report, Department of Economic and Social Affairs, Population Division, United Nations

[2] C. Rotariu, H. Costin, G. Andruseac, R. Ciobotariu, and F. Adochiei, "An integrated system for wireless monitoring of chronic patients and elderly people," in *Proc. 15th Int. Conf Sys. Theory, Control, and Computing*, ICSTCC, Sinaia, Oct. 2011

[3] L. Wolf, and S. Saadaoui, "Architecture Concept of a Wireless Body Area Sensor Network for Health Monitoring of Elderly People," in *Proc. 4th IEEE Consumer Communicat and Networking Conference*, CCNC, pp. 722-726, Jan. 2007

[4] S. Armstrong, "Wireless connectivity for health and sports monitoring: a review," in *British Journal of Sports Medicine*, vol. 41, Issue 5, pp. 285-289, Jan. 2007

[5] H. Sjoland, and et. al., "A Receiver Architecture for Devices in Wireless Body Area Networks," *IEEE Jour. Emerging Sel. Top. Circ. Sys.*, vol. 2, no. 1, pp. 82-95, March 2012

[6] H. Cao, V Leung, C. Chow, and H. Chan, "Enabling technologies for wireless body area networks: A survey and outlook," *IEEE Comm. Mag.*, vol. 47, no. 12, pp. 84-93, Dec. 2009

[7] K. Kyung-Sup, S. Ullah, and N. Ullah, "An overview of IEEE 802.15.6 standard," in *3rd Int. Symp. App. Sci. Biomed. Comm. Tech.*, ISABEL, Rome, Nov. 2010

[8] P. S. Hall, and Y. Hao, "Antennas and Propagation for Body-Centric Wireless Communications," Artech Hounce Inc., 685 Canton Street, Norwood, MA 02062, 2006

[9] C. Hertleer, H. Rogier, L. Vallozzi, and L. Van Langenhove, “A Textile Antenna for Off-Body Communication Integrated Into Protective Clothing for Firefighters,” *IEEE Trans. Antennas Propagat.*, vol. 57, no. 4, pp. 919-925, April 2009

[10] J. Carter, J. Saberin, T. Shah, P.R. Sai Ananthanarayanan, and C. Furse, “Inexpensive fabric antenna for off-body wireless sensor communication,” in *Proc. IEEE Antennas Propagat. Soc. Int. Symp.*, APSURSI), Toronto, July 2010

[11] Qiang Bai, Hyung-Joo Lee, K.L. Ford, R.J. Langley, “Switchable textile microstrip antenna for on/off-body communications and shape distortion study,” in *IEEE Asia-Pacific Conf. Antennas Propagat.*, APCAP, pp. 114-115, Aug. 2012

[12] R. Chandra, and A.J. Johansson, “A Link Loss Model for the On-Body Propagation Channel for Binaural Hearing Aids,” *IEEE Trans. Antennas Propagat.*, vol. 61, no. 12, pp. 6180-6190, Dec. 2013

[13] [online]http://www.medtronicdiabetes.com/treatment-and-products/minimed-revel-system, downloaded Dec. 2013

[14] A. Fort, F. Keshmiri, G.R. Crusats, C. Craeye, and C. Oestges, “A Body Area Propagation Model Derived From Fundamental Principles: Analytical Analysis and Comparison With Measurements,” *IEEE Trans. Antennas Propag.*, vol. 58, no. 2, pp. 503-514, Feb. 2010

[15] G. Roqueta, A. Fort; C. Craeye and C. Oestges, “Analytical Propagation Models for Body Area Networks”, in *Proc. IET Seminar on Antennas Propagat. for Body-Centric Wireless Commun.*, pp. 90-96, Apr. 2007

[16] J. Ryckaert, P. De Doncker, R. Meys, A. de Le Hoye, and S. Donnay, “Channel model for wireless communication around human body”, *Electronics Lett.*, vol. 40, no. 9, pp. 543-544, April 2004

[17] T. Alves, B. Poussot, J.-M. Laheurte, “Analytical Propagation Modeling of BAN Channels Based on the Creeping-Wave Theory,” *IEEE Trans. Antennas Propagat.*, vol. 59, no. 4, pp. 1269-1274, Apr. 2011

[18] G.A. Conway, W.G. Scanlon, S.L. Cotton, and M.J.Bentum, “An analytical path-loss model for on-body radio propagation,” in *Proc. URSI Int. Symp. on Electromagnetic Theory*, pp. 332-335, Aug. 2010

[19] G.A. Conway, and W.G. Scanlon, “Antennas for Over-Body-Surface Communication at 2.45 GHz,” *IEEE Trans. Antennas Propagat.*, vol. 57, no. 4, pp. 844-855, Apr. 2009

[20] Chia-Hsien Lin, K. Saito, K. Takahashi, and K. Ito, “A Compact Planar Inverted-F Antenna for 2.45 GHz On-Body Communications,” *IEEE Trans. Antennas Propagat.*, vol. 60, no. 9, pp. 4422-4426, Sept. 2012

[21] [online]http://www.2-sight.eu/en/product-en, downloaded Dec. 2013

[22] K. Gosalia, G. Lazzi, and M. Humayun, “Investigation of a microwave data telemetry link for a retinal prosthesis,” *IEEE Trans. Microwave Theory Techniq.*, vol. 52, no. 8, pp. 1925-1933, Aug. 2004

[23] [online]http://www.givenimaging.com/en-int/Innovative-Solutions/Capsule-Endoscopy, Downloaded Dec. 2013

[24] J.J. Struijk, “An Inductive Tongue Computer Interface for Control of Computers and Assistive Devices,” *IEEE Trans. Biomed. Engg.*, vol. 53, no. 12, pp. 2594-2597, Dec. 2006

[25] H. Park, and et. al., “A Wireless Magnetoresistive Sensing System for an Intraoral Tongue-Computer Interface,” *IEEE Trans. on Biomed. Circuits Sys.*, vol. 6, no. 6, pp. 571-585, Dec. 2012

[26] S.L. Cotton, and W.G. Scanlon, “Channel Characterization for Single- and Multiple-Antenna Wearable Systems Used for Indoor Body-to-Body Communications,” *IEEE Trans. Antennas Propagat.*, vol. 57, no. 4, pp. 980-990, Apr. 2009

[27] Yu Wang, I.B. Bonev, J.O. Nielsen, I.Z. Kovacs, and G.F. Pedersen, “Characterization of the Indoor Multiantenna Body-to-Body Radio Channel,” *IEEE Trans. Antennas Propagat.*, vol. 57, no. 4, pp. 972-979, Apr. 2009

[28] R. Rosini, R. D’Errico, and R. Verdone, “Body-to-Body communications: A measurement-based channel model at 2.45 GHz,” in *Proc. IEEE 23rd Int. Symp. Pers. Indoor Mobile Radio Commun.*, PIMRC, pp. 1763-1768, Sept. 2012

[29] A. J Johansson, “Wireless Communication with Medical Implants: Antennas and Propagation,” PhD Dissertation, Department of Electroscience, Lund University, 2004

[30] R. Chavez-Santiago, A. Khaleghi, I. Balasingham, and T.A. Ramstad, “Architecture of an ultra wideband wireless body area network for medical applications,” in *Proc. 2nd Int. Symp. Applied Sci. Biomed. Commun. Tech.*, ISABEL, Bratislava, Nov. 2009

[31] Q.H. Abbasi, A. Sani, A. Alomainy, and Y. Hao, “Numerical Characterization and Modeling of Subject-Specific Ultrawideband Body-Centric Radio Channels and Systems for Healthcare Applications,” *IEEE Trans. Info. Tech. Biomed.*, vol. 16, no. 2, pp. 221-227, Mar. 2012

[32] A. Alomainy, A. Sani, A. Rahman, J.G. Santas, and Y. Hao, “Transient Characteristics of Wearable Antennas and Radio Propagation Channels for Ultrawideband Body-Centric Wireless Communications,” *IEEE Trans. Antennas Propagat.*, vol. 57, no. 4, pp. 875-884, Apr. 2009

[33] A. Sani, and et. al, “Experimental Characterization of UWB On-Body Radio Channel in Indoor Environment Considering Different Antennas,” *IEEE Trans. Antennas Propagat.*, vol. 58, no. 1, pp. 238-241, Jan. 2010

[34] S. Alipour, F. Parvaresh, H. Ghajari, and F.K. Donald, “Propagation characteristics for a 60 GHz Wireless body area network (WBAN),” in *Proc. Military Commun. Conf.*, MILCOM, pp. 719-723, Nov. 2010

[35] N. Chahat, M. Zhadobov, S. Alekseev, and R. Sauleau, “Human skin-equivalent phantom for on-body antenna measurements in 60 GHz band,” *Electronics Lett.*, vol. 48, no. 2, pp. 67-68, Jan. 2012

[36] N. Chahat, M. Zhadobov, S.A. Muhammad, L. Le Coq, R. Sauleau, “60-GHz Textile Antenna Array for Body-Centric Communications,” *IEEE Trans. Antennas Propagat.*, vol. 61, no. 4, pp. 1816-1824, April 2013

[37] N. Chahat, G. Valerio, M. Zhadobov, and R. Sauleau, “On-Body Propagation at 60 GHz,” *IEEE Trans. Antennas Propagat.*, vol. 61, no. 4, pp. 1876-1888, April 2013

[38] Federal Communications Commission website: http://www.fcc.gov

[39] European Telecommunication Standards Institute
website: http://www.etsi.org

[40] European Telecommunications Standards Institute, ETSI EN 301 839-1 V1.3.1:Electromagnetic compatibility and Radio spectrum Matters (ERM); Short Range Devices (SRD); Ultra Low Power Active Medical

Implants (ULP-AMI) and Peripherals (ULP-AMI-P) operating in the frequency range 402 MHz to 405 MHz; Part 1: Technical characteristics and test methods, 2009

[41] FCC Encyclopedia, Medical Device Radio communications Service (MedRadio), [online] http://www.fcc.gov/encyclopedia/medical-device-radiocommunications-service-medradio, downloaded Dec. 2013

[42] Electronic Code of Federal Regulations, Title 47: Telecommunication, Part 95-Personal Radio Services, Subpart I-Medical Device Radiocommunication Service (MedRadio)

[43] C.S. Farlow, "An Overview of the Medical Device Radiocommunications Service (MedRadio) and Future Telemetry Considerations," *1st Invitational Workshop on Body Area Network Technology and Applications Future Directions, Technologies, Standards and Applications*, Worcester Polytechnic Institute, June 2011

[44] Electronic Code of Federal Regulations, Title 47: Telecommunication, Part 95-Personal Radio Services, Subpart H-Wireless Medical Telemetry Service (WMTS)

[45] FCC Encyclopedia, Wireless Medical Telemetry Service (WMTS), [online] http://www.fcc.gov/encyclopedia/wireless-medical-telemetry-service-wmts, downloaded Dec. 2013

[46] IEEE Standard, 802.15.6, IEEE Standard for Local and metropolitan area networks - Part 15.6: Wireless Body Area Networks, 2012

[47] 47 CFR Parts 2 and 95, [ET Docket No. 0859; FCC 1254], Medical Body Area Network, Federal Register, Rules and Regulations, vol. 77, No. 176, 11 Sept., 2012

[48] R. Chandra, and A. J Johansson, "Miniaturized antennas for link between binaural hearing aids," in *Proc. 32nd Annu. Int. Conf. of the IEEE Engg. Med. Biol. Soc.*, EMBC, pp. 688-691, Aug. 2010

[49] J. Kim, and Y. Rahmat-Samii, "Implanted antennas inside a human body: simulations, designs, and characterizations," *IEEE Trans. Microwave Theo. Tech.*, vol. 52, no. 8, pp. 1934-1943, Aug. 2004

[50] F. Merli, and et. al., "Design, Realization and Measurements of a Miniature Antenna for Implantable Wireless Communication Systems," *IEEE Trans. Antennas Propagat.*, vol. 59, no. 10, pp. 3544-3555, Oct. 2011

[51] A. Kiourti, and K.S. Nikita, “A Review of Implantable Patch Antennas for Biomedical Telemetry: Challenges and Solutions [Wireless Corner],” *IEEE Antennas Propag. Mag*, vol. 54, no. 3, pp. 210-228, June 2012

[52] Ho-Yu Lin, M. Takahashi, K. Saito, and K. Ito, “Performance of Implantable Folded Dipole Antenna for In-Body Wireless Communication,” *IEEE Trans. Antennas Propagat.*, vol. 61, no. 3, pp. 1363-1370, Mar. 2013

[53] F. Merli, B. Fuchs, J. R. Mosig, A. K. Skriverviky, “The Effect of Insulating Layers on the Performance of Implanted Antennas,” *IEEE Trans. Antennas Propagat.*, vol. 59, no. 1, pp. 21-31, Jan. 2011

[54] A. Karlsson, “Physical limitations of antennas in a lossy medium,” *IEEE Trans. Antennas Propagat.*, vol. 52, no. 8, pp. 2027-2033, Aug. 2004

[55] D. A. Sanchez-Hernandez, “High Frequency Electromagnetic Dosimetry,” Artech House, Inc., 685 Canton Street, Norwood, MA 02062

[56] “Guidelines For Limiting Exposure To Time-Varying Electric, Magnetic, and Electromagnetic Fields,” *ICNIRP Guidelines*, International Commission on Non-Ionizing Radiation Protection, 1998

[57] “Proposed Changes in the Commission’s Rules Regarding Human Exposure to Radiofrequency Electromagnetic Fields,” *FCC Technical Report*, Federal Communications Commission, USA, 2003

[58] J. Lee and S. Nam, “Effective Area of a Receiving Antenna in a Lossy Medium,” *IEEE Trans. Antennas Propagat.*, vol. 57, Issue 6, pp. 1843 - 1845, Jun. 2009

[59] An Internet resource for the calculation of the Dielectric Properties of Body Tissues in the frequency range 10 Hz - 100 GHz, Italian National Research Council, Institute for Applied Physics, Nello Carrara, Florence, Italy, [online] http://niremf.ifac.cnr.it/tissprop/

[60] SARSYS Project, “Development of Procedures for the Assessment of Exposure to Electromagnetic Near-Fields from Telecommunications Equipment,” Final Technical Report, Microwave Consultants Limited (MCL), Great Britain, IT’IS Foundation for Research on Information Technologies in Society, Switzerland, Schmid & Partner Engineering AG, Switzerland and INTEC Ghent Unviversity, Belgium, Jul. 1998 - Jul. 2000

[61] MCL Technology Ltd, Court Farmhouse, Dingstow, Monmouthshire, NP25 4DY, UK

[62] Schmid & Partner Engineering AG, Zeughausstrasse 43, 8004 Zurich, Switzerland

[63] IT'IS Foundation, Zeughausstrasse 43, CH-8004 Zurich, Switzerland

[64] Universiteit Gent, Vakgroep, Informatietechnologie, Sint-Pietersnieuwstraat 41, 9000 Gent, Belgium

[65] The history of the SAM head phantom, [online]:http://www.mcluk.org/headbackground.php, downloaded Dec. 2013

[66] R. Chandra, and A. J Johansson, "Influence on the ear-to-ear link loss from heterogeneous head phantom variations," in *Proc. 5th Eur. Conf. Antennas Propagat. (EUCAP)*, pp. 1612-1615, Apr. 2011

[67] Curious Labs Inc. 655 Capitola Road, Suite. 200, Santa Cruz, CA 95062

[68] A.J Johansson, "Wave-propagation from medical implants-influence of body shape on radiation pattern," in *2nd Joint Proc. 24th Ann. Conf. Annual Fall Meet. Biomed. Engg. Soc. Engg. Med. Bio.*, EMBS/BMES, vol. 2, pp. 1409-1410, 2002

[69] R. Chandra, and A. J Johansson, "An Analytical Link-Loss Model for On-Body Propagation Around the Body Based on Elliptical Approximation of the Torso With Arms' Influence Included," *IEEE Antennas Wireless Propagat. Lett.*, vol. 12, pp. 528-531, 2013

[70] R. Chandra, T. Abbas, and A. J Johansson, "Directional analysis of the on-body propagation channels considering human's anatomical variations," in *Proc. 7th Int. Conf. Body Area Net.*, BodyNets, pp. 120-123, Sept. 2012

[71] R. Chandra, and A. J Johansson, "An approach to analyze the movements of the arms while walking using wearable wireless devices," in *Proc. 35th Ann. Int. Conf. IEEE Engg. Med. Bio. Soc.*, EMBC, pp. 3431,3434, Jul. 2013

[72] A. Christ, and et al., "The Virtual Family Development of anatomical CAD models of two adults and two children for dosimetric simulations", *Phy. Med. Bio.*, vol. 55, no. 2, pp. N23-N38, Jan. 2010

[73] R. Chandra, and A. J Johansson, "An elliptical analytic link loss model for wireless propagation around the human torso," in *Proc. 6th Eur. Conf. Antennas Propagat.*, pp. 3121-3124, Mar. 2012

[74] R. Chandra, A. J Johansson, and F. Tufvesson, "Localization of an RF source inside the Human body for Wireless Capsule Endoscopy," in *Proc. 8th Int. Conf. Body Area Net.*, pp. 48-54, Oct. 2013

[75] IEEE Recommended Practice for Determining the Peak Spatial-Average Specific Absorption Rate (SAR) in the Human Head from Wireless Communications Devices: Measurement Techniques, IEEE Standard 1528-2003, 2003

[76] Ito and Saito laboratory, Chiba University,
Website: http://www.ap.tu.chiba-u.jp

[77] Andreas F. Molisch, *Wireless Communications*, IEEE Press/John Wiley & Sons, Ltd., 2009

[78] "NIDCD Fact Sheet: Hearing Aids", NIH Publication No. 08-4340, National Institute on Deafness and Other Communication Disorders, National Institute of Health, U.S. Department of Health and Human Services, Nov. 2008

[79] D. R. Moore, "Anatomy and Physiology of Binaural Hearing," *Int. Jour. Audiology*, vol. 30, Issue 3, pp. 125-134, 1991

[80] J. Zhang, and O. Breinbjerg, "Self-resonant electrically small loop antennas for hearing-aids application," in *Proc. 4th Eur. Conf. Antennas Propagat.*, EUCAP, Apr. 2010

[81] W. H. Yatman, L. K. Larsen, S. H. Kvist, J. Thaysen, and K.B. Jakobsen, "In-the-ear hearing-instrument antenna for ISM-band body-centric ear-to-ear communications," in *Proc. Loughborough Antennas Propagat. Conf.*, LAPC, Loughborough, Nov. 2012

[82] S. H. Kvist, K. B. Jakobsen, and J. Thaysen, "Design and Measurement of a 2.45 GHz On-Body Antenna Optimized for Hearing Instrument Applications," in *Proc. 34th Annu. Antenna Meas. Techniq. Assoc. Symp.*, pp. 33-37, Nov. 2012

[83] S. H. Kvist, S. Ozden, J. Thaysen, and K. B. Jakobsen, "Improvement of the ear-to-ear path gain at 2.45 GHz using parasitic antenna element," in *Proc. 6th Eur. Conf. Antennas Propagat.*, EUCAP, pp. 944-947, Mar. 2012

[84] L. Huitema, S. Sufyar, C. Delaveaud, and R. D'Errico, "Miniature antenna effect on the ear-to-ear radio channel characteristics," in *Proc. 6th Eur. Conf. Antennas Propagat.*, pp. 3402-3406, Mar. 2012

[85] P. S. Hall, and et. al., “Antennas and propagation for on-body communication systems,” *IEEE Antennas Propagat. Mag.*, vol. 49, no. 3, pp. 41-58, June 2007

[86] S. L. Cotton, G. A. Conway, and W. G. Scanlon, “A Time-Domain Approach to the Analysis and Modeling of On-Body Propagation Characteristics Using Synchronized Measurements at 2.45 GHz,” *IEEE Trans. Antennas Propagat.*, vol. 57, no. 4, pp. 943-955, Apr. 2009

[87] A.M Eid, and J.W. Wallace, “Accurate Modeling of Body Area Network Channels Using Surface-Based Method of Moments,” *IEEE Trans. Antennas Propagat.*, vol. 59, no. 8, pp. 3022-3030, Aug. 2011

[88] R. Chandra, and A. J Johansson, “Effect of frequency, body parts and surrounding on the on-body propagation channel around the torso,” in *Proc. 34th Ann. Int. Conf. IEEE Engg. Med. Bio. Soc.*, pp. 4533-4536, Aug. 2012

[89] S. M. Bruijn, O. G. Meijer, P. J. Beek, and J. H. van Dieen, “The effects of arm swing on human gait stability,” *The Journal of Exp. Biology*, pp. 3945-3952, Dec. 2010

[90] J. Roggendorf, S. Chen, S. Baudrexel, S. van de Loo, C. Seifried, and R. Hilker, “Arm swing asymmetry in Parkinson’s disease measured with ultrasound based motion analysis during treadmill gait,” *Gait & Posture*, vol. 35, Issue 1, pp. 116-120, Jan. 2012

[91] X. Huang, J. M. Mahoney, M. M. Lewis, G. Du, S. J. Piazza, and J. P. Cusumano, “Both coordination and symmetry of arm swing are reduced in Parkinson’s disease,” *Gait & Posture*, vol. 35, Issue 3, pp. 373-377, Mar. 2012

[92] “Antenna Array Calibration and MIMO Channel Sounding,” Brochure, MEDAV GmbH, Grafenberger Str. 32-34, D-91080 Uttenreuth, Germany

[93] G. Ciuti, A. Menciassi, P. Dario, “Capsule Endoscopy: From Current Achievements to Open Challenges,” *IEEE Reviews in Biomed. Engg.*, vol. 4, pp. 59-72, 2011

[94] T.D. Than, G. Alici, H. Zhou, Weihua Li, “A Review of Localization Systems for Robotic Endoscopic Capsules,” *IEEE Trans. Biomed. Engg.*, vol. 59, no. 9, pp. 2387-2399, Sept. 2012

[95] D. Manteuffel, and M. Grimm, "Localization of a functional capsule for wireless neuro-endoscopy," in *Proc. Biomed. Wireless Tech., Net., Sensing Sys.*, BioWireleSS, pp. 61-64, Jan. 2012

[96] K.Pahlavan, and et. al., "RF Localization for Wireless Video Capsule Endoscopy," *Int. Journal Wireless Inf. Net.*, Vol. 19, pp. 326-340, Dec. 2012

[97] K. Arshak and F. Adepoju, "Adaptive linearized methods for tracking a moving telemetry capsule," in *Proc. IEEE Int. Symp. Ind. Electron*, pp. 2703-2708, June 2007

[98] D. Fischer, and et. al., "Localization of the wireless capsule endoscope in its passage through the GI tract," *Gastrointestinal Endoscopy*, vol. 53, AB126, 2001

[99] T. Shah, S. M. Aziz, and T. Vaithianathan, "Development of a tracking algorithm for an in-vivo RF capsule prototype," in *Proc. Int. Conf. Electr. Comput. Eng.*, pp. 173-176, Dec. 2006

[100] W. Lujia , H. Chao , T. Longqiang , L. Mao and M. Q. H. Meng, "A novel radio propagation radiation model for location of the capsule in GI tract", in *Proc. IEEE Int. Conf. Rob. Biomimetics*, pp. 2332-2337, 2009

[101] W. Lujia, L. Li, H. Chao, and M. Q. H. Meng, "A novel RF-based propagation model with tissue absorption for location of the GI tract," in *Proc. Annu. Int. Conf. IEEE Eng. Med. Biol. Soc.*, pp. 654-657, Sept. 2010

[102] K. Arshak and F. Adepoju, "A Method for Estimating the Geometric Position of a Wireless Telemetry Capsule in Real-Time," in *Proc. of European Conf. on Wireless Technol.*, pp. 193-196, Oct. 2007

[103] W. Yi, F. Ruijun, Y. Yunxing, U. Khan and K. Pahlavan, "Performance bounds for RF positioning of endoscopy camera capsules," in *Proc. IEEE Trop. Conf. Biomed. Wireless Technol.*, pp. 71-74, 2011

[104] H. Jinlong, and et. al., "Design and implementation of a high resolution localization system for in-vivo capsule endoscopy," in *Proc. 8th Int. conf. Dependable Auton. Secure Comput.*, pp. 209-214, Dec. 2009

[105] N. N. Rao, Elements of Engineering Electromagnetics, 5th Edition, Prentice-Hall, 2000

[106] N. Joachimowicz, C. Pichot, and J-P. Hugonin, "Inverse scattering: an iterative numerical method for electromagnetic imaging," *IEEE Trans. Antennas Propagat.*, vol. 39, no. 12, pp. 1742-1753, Dec. 1991

[107] J.J. Mallorqui, N. Joachimowicz, A. Broquetas, and J. Bolomey, "Quantitative images of large biological bodies in microwave tomography by using numerical and real data," *Electronics Lett.*, vol. 32, no. 23, pp. 2138-2140, Nov. 1996

[108] A. Abubakar, P.M. van den Berg, and J.J Mallorqui, "Imaging of biomedical data using a multiplicative regularized contrast source inversion method," *IEEE Trans. Microwave Theory Techniq.*, vol. 50, no. 7, pp. 1761-1771, Jul. 2002

[109] S.Y. Semenov, and et. al., "Three-dimensional microwave tomography: initial experimental imaging of animals," *IEEE Trans. Biomed. Engg.*, vol. 49, no. 1, pp. 55-63, Jan. 2002

[110] P. Mojabi, and J. LoVetri, "Microwave Biomedical Imaging Using the Multiplicative Regularized Gauss–Newton Inversion," *IEEE Antennas Wireless Propagat. Lett.*, vol. 8, pp. 645-648, 2009

[111] C. Gilmore, A. Zakaria, S. Pistorius, and J. Lo Vetri, "Microwave Imaging of Human Forearms: Pilot Study and Image Enhancement," *Int. Jour. Biomed. Imaging*, vol. 2013, Article ID 673027, 2013

[112] R. Chandra, and A. J Johansson, "In-mouth antenna for tongue controlled wireless devices: Characteristics and link-loss," in *Proc. 33rd Ann. Int. Conf. IEEE Engg. Med. Bio. Soc.*, EMBC, pp. 5598-5601, Sept. 2011

[113] X. Huo, and M. Ghovanloo, "Using Unconstrained Tongue Motion as an Alternative Control Mechanism for Wheeled Mobility," *IEEE Trans. Biomed. Engg.*, vol. 56, no. 6, pp. 1719-1726, June 2009

[114] M.E. Lund, H.V. Christiensen, H.A. Caltenco, E.R. Lontis, B. Bentsen, and L.N.S. Andreasen Struijk, "Inductive tongue control of powered wheelchairs," in *Proc. 32nd Ann. Int. Conf. IEEE Engg. Med. Bio. Soc.*, EMBC, pp. 3361-3364, Sept. 2010

[115] Dielectric Constants of Common Materials,
[online] http://www.rafoeg.de/20,Dokumentenarchiv/
20,Daten/dielectric_chart.pdf, downloaded Jan. 2014

[116] J. Rahola, and J. Ollikainen, "Analysis of Isolation of Two-Port Antenna Systems using Simultaneous Matching," in *Proc. 2nd Eur. Conf. Antennas Propagat.*, EUCAP, Edinburgh, Nov. 2007

Appendix

FDTD

Simulations done in this thesis uses the finite-difference-time-domain (FDTD) method. The FDTD is a numerical analysis technique for solving the Maxwell's electromagnetic equations in the three dimensions and in time. The volume to be investigated is subdivided into small cubic volume called voxel. In these voxels Maxwell's equations are solved iteratively with as time is stepped forward. The electric field (**E**) and magnetic field (**H**) components are updated in the grid in a leap-frog scheme using the finite difference form of the curl operators on the fields that surround the component. The Maxwell's curl equations are

$$\nabla \times \mathbf{H} = \frac{\partial}{\partial t}\varepsilon \mathbf{E} + \sigma_e \mathbf{E}$$

$$\nabla \times \mathbf{E} = -\frac{\partial}{\partial t}\mu \mathbf{H} - \sigma_h \mathbf{H}$$

where σ_h is a term for magnetic losses in the material. These equations are discretized using finite difference approximations in time as well as space. The first partial space and time derivative are

$$\frac{\partial F(i,j,k,n)}{\partial x} = \frac{F(i+1/2,j,k,n) - F(i-1/2,j,k,n)}{\Delta x} + O[(\Delta x)^2],$$

$$\frac{\partial F(i,j,k,n)}{\partial t} = \frac{F(i,j,k,n+1/2) - F(i-1/2,j,k,n-1/2)}{\Delta x} + O[(\Delta t)^2],$$

where $F(i,j,k,n)$ is the electric or magnetic field at time $n\Delta t$ and i,j,k are indices to the 3D grid. $O[(\Delta x)^2]$ and $O[(\Delta t)^2]$ are error terms in space and time, respectively. This is applied to the Maxwell's curl equations and discretized to obtain explicit expressions for all six field components. The transient fields in a 3D grid are then calculated with every forward step in time. To obtain a stable numerical solution using the FDTD, the time step used for updating is limited by

$$\Delta t \leq \frac{1}{c\sqrt{(\Delta x)^{-2} + (\Delta y)^{-2} + (\Delta z)^{-2}}}$$

where c is the speed of light within the material in a cell and, Δx, Δy, and Δz are the mesh steps in the three dimensions. Using fine mesh results in larger memory requirements and longer simulation time.

Further, at the boundary of the simulation space, truncation is needed so that the EM waves do not reflect back to the simulation domain. This truncation is usually done with absorbing boundary conditions (ABC) which absorbs the incoming waves. This is done by placing uniaxial perfectly matched layers (UPML) at the truncation. UPML acts like an absorber in an anechoic chamber. The incoming waves are attenuated by the successive lossy layers and when the waves reach the last layer it is reflected back as outside the UPML a PEC is placed. However, as the EM waves have to travel the UPML twice, very weak EM waves re-enter the simulation domain.

SEMCAD-X

The electromagnetic field simulator which is used in for the FDTD simulations is SEMCAD-X provided by Schmid & Partner Engineering AG, Switzerland. In SEMCAD-X, non-uniform grids are implemented to save memory by using a variable grid size to capture fine local structure. Further, Nvidia Quadro® FX 5600 graphics processing unit is used for a faster simulation. Care has been taken to obtain stable solution. All simulations have been discretized to at least 10 voxels per wavelength in the material. For a broadband simulation a Gaussian pulse is used and for a harmonic simulation a sinusoidal signal is used. The broadband simulation is terminated when the pulse has decayed completely whereas the harmonic simulation is terminated when the steady state is reached.

Part II

Included Papers

Paper I

Miniaturized Antennas For Link Between Binaural Hearing Aids

We have investigated the possibility of using the 2.45 GHz ISM band for communication between binaural hearing aids. The small size of a modern hearing aid makes it necessary to miniaturize the antennas to make this feasible. Two different types of hearing aid placements have been investigated: in the outer ear and in the ear canal. Both put strict demands on the size of the antenna, which have been miniaturized by applying disc loads and high permittivity materials. The investigations have been done by FDTD simulation of a modified SAM phantom head, where we have included a simple model of the ear canal. Simulations show that the outer ear placement is better, as it gives a total link loss of 48 dB. The placement in the ear canal gives a total link loss of 92 dB.

R. Chandra, and A. J Johansson,
"Miniaturized antennas for link between binaural hearing aids,"
in *Proc. 32nd Annu. Int. Conf. of the IEEE Engg. in Med. and Biol. Soc.*, EMBC, pp. 688-691, Aug. 2010

1 Introduction

Binaural processing in audiology is the capability of the brain to process sound coming from both the left and the right ears which helps in localizing the source of a sound [1]. Modern binaural hearing aids use adaptive filtering for noise suppression. Synchronization of such hearing aids is important for improved hearing in noisy environments. Unsynchronized hearing aids may result in loss of localization and thus the user may not be able to predict the direction to the source of the sound correctly. Size and power are the two main challenges for designing a system which could be embedded into hearing aids for communication with each other. One alternative is to use Near Field Magnetic Induction (NFMI) for transmission of information as used in Oticon Epoq [2]. They communicate binaurally with a built-in radio transmitter using NFMI technology at 3.84 MHz [3]. Design of a low power wireless hearing aid communication system using packaged antenna for behind-the-ear (BTE) placement at 400 MHz has been discussed in [4], [5].

This paper explores the possibility of using 2.45 GHz ISM band for establishing wireless communication link between hearing aids using small antennas. The two main challenges in implementing this are the size of the antenna and the presence of the human head, which is a lossy medium for electromagnetic wave propagation. Miniaturization of a monopole antenna is achieved by embedding them into a dielectric of high permittivity and loading them with a disc [6]. Two positions has been explored, (a) by inserting the antenna into the ear canal and (b) by using the antenna outside the ear. These two positions can be used for into-the-canal (ITC) hearing aids and into-the-ear (ITE) hearing aids, respectively. Disc loaded monopole antennas embedded inside high permittivity material were simulated for both the ITE and ITC scenarios. All simulations were done in commercially available SEMCAD-X [13] which uses the FDTD method.

2 Numerical Head Model

Many numerical head models have been used in the literature [7]-[10]. They have typically been used either for simulating an implant antenna or for measuring radiation effects from the mobile phones. These models do not have ear canals. The ear canal is basically an air filled tube and has significant effect on the antennas in the hearing aids. The SAM phantom model provided by SEMCAD-X [13] has been modified to include ear canals. The ear canal has been modeled as a cylindrical air cavity having a diameter of 7 mm and a length of 26 mm, which is a realistic model for average adult human ear canal [11]. Homogeneous electrical property of the human head (dielectric constant, $\varepsilon_r = 39.2$ and conductivity, $\sigma_e = 1.80$ S/m) at 2.45 GHz is considered for the SAM liquid. These electrical properties are that of equivalent head tissue given in [12]. The SAM shell was assumed to have $\varepsilon_r = 3.7$. Fig. 1 shows the dimensions of the model. A homogeneous head model was used in order to reduce the simulation time and to get results which are independent from the variation between the different available heterogeneous head models.

3 Wave Propagation Theory

3.1 Wave Propagation inside Head

Classical theory deals with antennas placed inside a lossless medium. But for scenarios like ITC, the antenna no longer remain inside a lossless medium, rather it is inside a lossy medium characterized by the electrical properties of the surrounding which in this case is the head tissue [14]. The complex permittivity of a medium, ε_c is defined as:

$$\varepsilon_c = \varepsilon_e - j\frac{\sigma_e}{\omega} \tag{1}$$

where σ_e is conductivity and $\omega = 2\pi f$, f being the frequency.

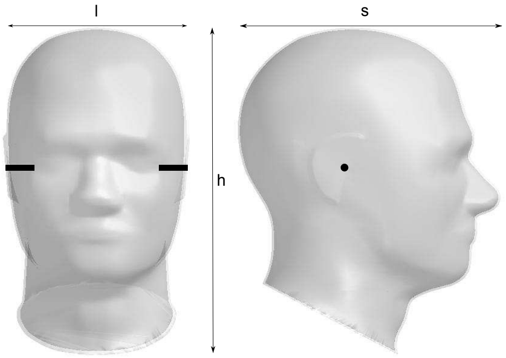

Figure 1: Modified SAM phantom model with ear canals with l=164 mm, h=312 mm, s=234 mm. Left:Front View, Right:Side View. The cylindrical ear canals are drawn in black. Its radius is 3.5 mm and the length is equal to 26 mm.

The permittivity ε_e is scaled with the permittivity of vacuum $\varepsilon_0 = 8.854\times10^{-12}$ as $\varepsilon_r = \frac{\varepsilon_e}{\varepsilon_0}$. The complex wavenumber of a lossy medium is defined as:

$$k = \omega\sqrt{\mu\varepsilon_c} = \omega\sqrt{\mu(\varepsilon_e - j\frac{\sigma_e}{\omega})} = \omega\sqrt{\mu(\varepsilon_r\varepsilon_0 - j\frac{\sigma_e}{\omega})} \tag{2}$$

For radiation from an antenna in a lossy medium, two separate loss mechanisms contribute: (a) Attenuation loss, proportional to $e^{-2\alpha R}$, where $\alpha = |Im[k]|$ and (b) dissipation loss in the reactive energy stored in the near field around the antenna [15].

From the extended Friis formula for a lossy medium [15], path loss in a lossy medium can be written as:

$$(PL)_{lossy\_medium} = -20\log_{10}\left(\frac{\lambda_{eff}}{4\pi R}e^{-\alpha R}\right) \tag{3}$$

where $\lambda_{eff} = \frac{2\pi}{Re[k]}$ is the effective wavelength in a lossy medium and R is the distance between the transmitting and receiving antennas.

3.2 Wave propagating around the head

A creeping wave is the phenomenon by which the receiving antenna located on the other side of a head receives the signal. This phenomenon is common for on body surface propagation [16]. A creeping wave can be modeled as a free space wave with some extra loss because of the creeping phenomenon, with a distance traveled, same as that of the curvature of the head and with a loss exponent $n > 2$, because no direct line of sight exist. This scenario is applicable for the ITE hearing aids.

4 Antenna Design

4.1 Size reduction Technique

Two methods for the size reduction of the monopole antenna have been tested. The first one is loading the monopole antenna with a disc. Further size reduction has been achieved by embedding it in a dielectric medium [17]. For a dielectric medium of infinite extent, the size reduction factor, F_r is equal to $\sqrt{\varepsilon_r}$ of the medium. In a practical antenna for hearing aids, the size reduction factor, F_{ra} will be a function of the shape, size, electrical characteristics of the dielectric material, electrical properties of the head tissues and the position of the antenna with $F_{ra} < F_r$.

4.2 Antenna Structure

The antennas were optimized for the return loss, $S_{11} \leq -10$ dB and the bandwidth in 2.45 GHz ISM band. The degrees of freedom which could be optimized are dimensions and the dielectric constant of the dielectric, the radius of the ground plane, the length and the radius of the central conductor and the radius of the disc load. For ITE antenna, the dimensions of the dielectric was chosen such that it fits inside the outer ear and that for ITC was chosen so that it fits inside the ear canal. The radius of the disc load (r_{disc}) and the central conductor (r_{mp}) was fixed to reduce the degrees of freedom. The length of the central conductor (l_{mp}), the radius of the ground plane (r_g) and the dielectric constant were varied to get a minimal return loss in 2.45 GHz ISM band. Table 1 summarizes the optimized antennas dimensions and the dielectric constant of the material needed to embed them. The dielectric material has been assumed to be lossless ($\sigma_e = 0$). It should be noted here that other values may also result in the optimized values for the return loss and the bandwidth depending upon which degree of freedom is kept constant.

ITE Antenna

For the ITE antenna, disc loaded monopole was embedded in a cylindrical dielectric of $\varepsilon_r = 56$ of the radius, $r_{d\_top} = 10$ mm and the height, $l_{d\_top} = 11$ mm. The ground plane was at a distance, $d = 1.75$ mm from the bottom of this dielectric element. However, an additional cylindrical dielectric element was required below this top cylindrical dielectric element for impedance matching with same ε_r of the radius, $r_{d\_lower} = 3.5$ mm and the height, $l_{d\_lower} = 8.5$ mm because of the ear canal and the presence of the human head. The axis of these dielectric elements coincides with the axis of the disc loaded monopole. Fig. 2 illustrates the geometry of the ITE antenna.

ITC Antenna

For the ITC antenna, the disc loaded monopole was embedded into a cylindrical dielectric ($\varepsilon_r = 49$) material of the radius, $r_d = 3.5$ mm and the length, $l_d = 11$ mm at the center of the dielectric element with the axis of the disc loaded monopole perpendicular to that of the dielectric element. Geometry for the ITC antenna is illustrated in Fig. 3.

5 Simulation Setup

Fig. 4 shows the model with the antennas position for the simulation. The orientation of the antennas was chosen so that the coupling between the left ear antenna and the right ear antenna was maximized. For the ITE case, the lower dielectric element was inserted into the ear canal so that the axis of antenna and the ear canal's axis are collinear. Since the monopole has broadside radiation pattern, the main part of the radiation will be in the tangential direction of the head and the electromagnetic waves will reach the other antenna by creeping along the head's surface. For the ITC case, the antenna was placed at the center of the ear canal with the axis of the central conductor vertical and perpendicular to the ear canal's axis. Simulations were done in commercially available numerical electromagnetic solver SEMCAD which uses the finite-difference-time-domain (FDTD) method. The antenna ground plane and the disc load was modeled as a thin Perfect Electric Conductor (PEC) sheet. The central monopole conductor was modeled as a thin PEC wire. A voltage source with an internal resistance of 50 Ω was used for the antenna excitation. A Gaussian sine wave with the central frequency of 2.45 GHz and the bandwidth of 1 GHz was used for the broadband simulation. Voxelling was done with a non uniform grid setting for faster simulation [16]. An uniaxial perfectly matched layer (UPML) was used as the simulation boundary around the model.

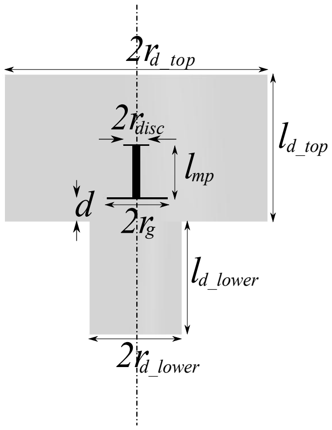

Figure 2: Geometry for the ITE antenna. Axis of the disc loaded monopole is the same as the axis of the dielectric elements shown by dash-dotted line

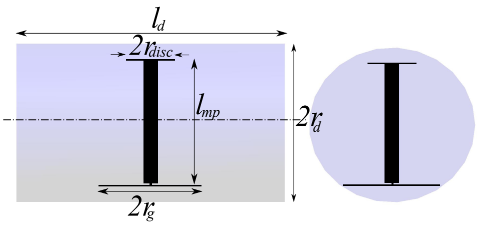

Figure 3: Geometry for the ITC antenna. Left: front view; Right: side view. It should be noted that the axis of the dielectric element shown by dash-dotted line is perpendicular to the axis of the disc loaded monopole.

Table 1: Antenna Parameters

Parameter	**ITC**	**ITE**
r_{disc}(mm)	1	1
r_{mp}(mm)	0.3	0.3
r_g(mm)	2.10	2.25
l_{mp}(mm)	5.3	4
ε_r	49	56

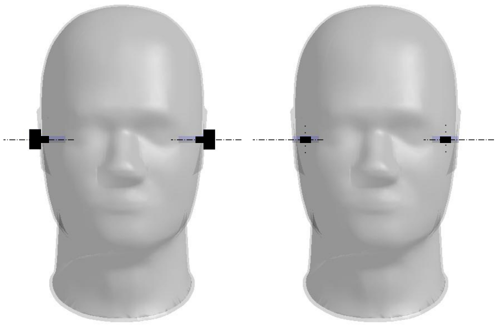

Figure 4: Antenna placement on the models for the simulation. Left: ITE case, Right: ITC case. The dash-dotted lines shows the axis of the ear canals. In the ITC case, the axis of the central conductor is shown by the dotted lines.

6 Simulation Results

6.1 Return Loss and Link Loss

The return loss (negative of reflection coefficient in dB) and the antenna coupling performance is plotted in Fig. 5. f_{res} is the resonance frequency and BW is the impedance bandwidth. Table 2 presents a summary of the simulation. If the theoretical value of the path loss is calculated from (3), we get $PL_{lossy\_medium} = 103.1$ dB for a distance, $R = 138$ mm, which is the distance between the antennas for the ITC case with the $\lambda_{eff} = 19.3$ mm at 2.45 GHz. This theory assumes an infinite lossy dielectric medium surrounding the antennas. The simulated S_{21} at 2.45 GHz has a value of -91.7 dB (link loss = 91.7 dB). The finite dimension of the head resulting in the reflections from the head-air interface contributes to the higher value of the simulated S_{21}. One more contributing factor for the higher value in the simulation is the waves that leaks out from the open end of the ear canal and reaches the receiving antenna by creeping along the head's surface as seen in Fig. 6. The simulated peak value of S_{21} for the ITE case is -47.1 dB. Fig. 7 shows the creeping wave phenomenon for ITE case.

Table 2: Simulation Results

Parameter	**ITC**	**ITE**
f_{res}(GHz)	2.46	2.44
$S11_{res}$(dB)	-11.0	-15.3
BW(MHz)	174	139.4
$S21_{peak}$(dB)	-91.7	-47.1
$S21_{2.45GHz}$(dB)	-91.7	-47.2
$S21_{res}$(dB)	-91.8	-47.1

6.2 Specific Absorption Rate

Specific Absorption Rate (SAR) is the mass-normalized rate at which EM energy is absorbed by the tissue at a specific location. SAR is an important biologically effective quantity used in protection guidelines dealing with EM energy exposure. The regulated spatial peak SAR limitation for the head in Europe is 2 W/Kg averaged over 10 g [18] of tissue and in USA, it is 1.6 W/Kg averaged over 1 g [19] of tissue. These limitations on the SAR value limits the maximum power that can be accepted by the antenna. Table 3 presents the

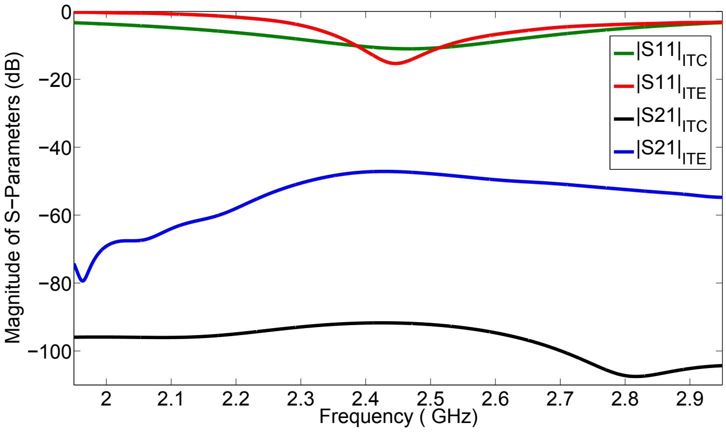

Figure 5: Simulated reflection coefficient (S_{11}) and the coupling between the antennas (S_{21})

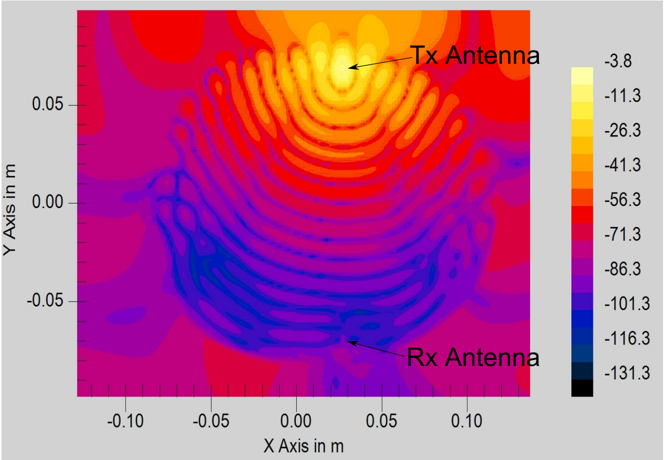

Figure 6: Real modulus of electric field at 2.45 GHz for propagation inside head tissues sliced at the level of the antennas for the ITC case. The waves leaking out from open end of the canal can also be seen.

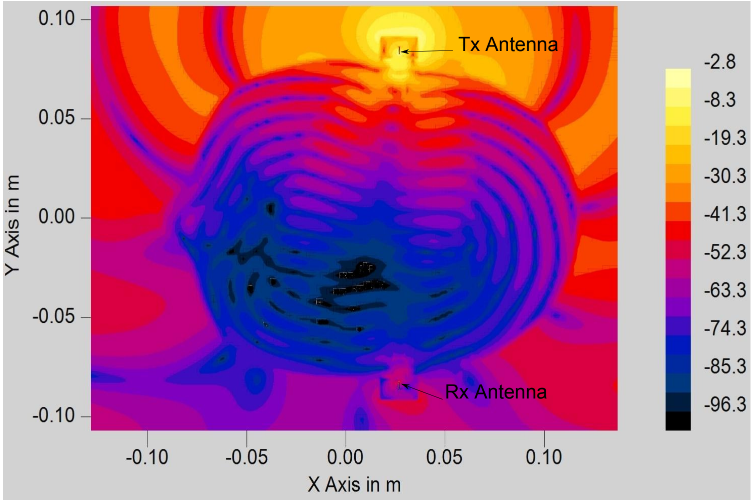

Figure 7: Real modulus of electric field at 2.45 GHz for creeping waves as seen from top of the head sliced at the level of the antennas for ITE scenario.

maximum accepted power for the ITE and ITC antenna under these limitations. These values were calculated in SEMCAD by fast averaging IEEE-C95.3/1528 guidelines [20]-[21].

Table 3: Maximum Accepted Power

SAR Limitation	**ITC**	**ITE**
1.6 W/Kg over 1 g	5.5 mW	18.4 mW
2 W/Kg over 10 g	37.3 mW	80.1 mW

7 Conclusions and Future Work

We have presented two antennas suitable in size and technical performance for use in establishing a wireless link between binaural hearing aids using the 2.45 GHz ISM-band. The external, ITE, case has a lower total link loss. The loss of the internal, ITC, case is higher due to the fact that the wave propagation is mainly through a lossy material.

Further analytical investigation will be done of the effects on the path loss from the internal reflections inside the head. Future studies will include a refined model of the middle ear and the ear canal in a heterogeneous head model as well as the upper part of the human torso, in order to get more realistic simulation results.

References

[1] D. R. Moore, "Anatomy and Physiology of Binaural Hearing," *International Journal of Audiology*, vol. 30, Issue 3, pp. 125 - 134, 1991

[2] D. J. Schum, "Redefining the hearing aid as the user's interface with the near and far worlds," *The Hearing Journal*, vol. 60, Issue 5, pp. 30-33, May 2007

[3] Website: http://www.oticon.dk

[4] G.S.A. Shaker, M.R. Nezhad-Ahmadi, S. Safavi-Naeini, and G. Weale, "On design of a low power wireless hearing aid communication system," *IEEE MTT-S Int. Microwave Symp. Digest*, pp. 903 - 906, June 2008

[5] G.S.A. Shaker, M.R. Nezhad-Ahmadi, S. Safavi-Naeini, G. Weale, "Modeling and design of a wireless hearing aid communication system," *IEEE Radio and Wireless Symposium, RWS '09.*, pp. 127 - 130, Jan. 2009

[6] T.L. Simpson, "The disk loaded monopole antenna," *IEEE Trans. Antennas Propagat.*, vol. 52, Issue 2, pp. 542 - 550, Feb. 2004

[7] J. Kim, and Y. Rahmat-Samii, "An implanted antenna in the spherical human head: SAR and communication link performance," *IEEE Tropical Conf. Wireless Commun. Tech.*, pp. 202 - 203, Oct. 2003

[8] J. Kim, and Y. Rahmat-Samii, "Implanted antennas inside a human body: simulations, designs, and characterizations," *IEEE Trans. Microwave Theo. Techniq.*, vol. 52, Issue 8, Part 2, pp. 1934 - 1943, Aug. 2004

[9] Z. N. Chen, G. C. Liu, and T. See, "Transmission of RF Signals Between MICS Loop Antennas in Free Space and Implanted in the Human Head," *IEEE Trans. Antennas Propagat.*, vol. 57, Issue 6, pp. 1850 - 1854, June 2009

[10] S. Koulouridis, and K.S. Nikita, "Study of the coupling between human head and cellular phone helical antennas," *IEEE Trans. Electromagnetic Compatibility*, vol. 46, Issue 1, pp. 62 - 70, Feb. 2004

[11] P. Kopf-Maier, *Wolf-Heidegger's Atlas of Human Anatomy*, vol. 2, Karger, 2000

[12] K. Fujimoto, *Mobile antenna systems handbook*, Artech House, 2008

[13] Website:http://www.semcad.com/

[14] A. J Johansson, "Wireless Communication with Medical Implants: Antennas and Propagation," *PhD thesis*, Lund University, Sweden, 2004

[15] J. Lee, and Sangwook Nam, "Effective Area of a Receiving Antenna in a Lossy Medium," *IEEE Trans. Antennas Propagat.*, vol. 57, Issue 6, pp. 1843 - 1845, June 2009

[16] G. A. Conway, and W. G.Scanlon, "Antennas for Over-Body-Surface Communication at 2.45 GHz," *IEEE Trans. Antennas Propagat.*, vol. 57, Part 1, Issue 4, pp. 844 - 855, Apr. 2009

[17] J. Lu, D. Thiel, and S. Saario, "FDTD analysis of dielectric-embedded electronically switched multiple-beam (DE-ESMB) antenna array," *IEEE Trans. Magnetics*, vol. 38, Issue 2, pp. 701 - 704, Mar. 2002

[18] "Guidelines For Limiting Exposure To Time-Varying Electric, Magnetic, and Electromagnetic Fields," *ICNIRP Guidelines*, International Commission on Non-Ionizing Radiation Protection, 1998

[19] "Proposed Changes in the Commission's Rules Regarding Human Exposure to Radiofrequency Electromagnetic Fields," *FCC Technical Report*, Federal Communications Commission, USA, 2003

[20] "IEEE Standard for Safety Levels with Respect to Human Exposure to Radio Frequency Electromagnetic Fields 3 kHz to 300 GHz," *IEEE Std C95.1*, 1999

[21] "IEEE Recommended Practice for Determining the Peak Spatial-Average Specific Absorption Rate (SAR) in the Human Head From Wireless Communications Devices: Measurement Techniques," *IEEE Standards*, IEEE Std 1528-2003, 2003

Paper II

A Link Loss Model for the On-body Propagation Channel for Binaural Hearing Aids

Binaural hearing aids communicate with each other through a wireless link for synchronization. An analytical propagation model is useful to estimate the ear-to-ear link loss for such binaural hearing aids. This paper presents an analytical model for the deterministic component of the ear-to-ear link loss. The model takes into account the dominant paths having most of the power of the creeping wave from the transceiver in one ear to the transceiver in the other ear, and the effect of the protruding part of the outer ear, called pinna. Simulations are done to validate the model using in-the-ear placement of antennas at 2.45 GHz on numerical heterogeneous phantoms of different age-groups and head sizes showing a good agreement with the model. The ear-to-ear link loss for a numerical homogeneous SAM (Specific Anthropomorphic Mannequin) phantom is compared with a numerical heterogeneous phantom. The loss for the SAM phantom is found to be 30 dB lower than that for the heterogeneous phantom. It is shown that the absence of the pinna and the lossless shell in the SAM phantom underestimate the link loss. The effect of the pinnas is verified through measurements on a phantom where we have included the pinnas fabricated by 3D-printing.

R. Chandra, and A. J Johansson,
"A Link Loss Model for the On-Body Propagation Channel for Binaural Hearing Aids," in *IEEE Trans. Antennas Propagat.*, vol. 61, no. 12, pp. 6180-6190, Dec. 2013

1 Introduction

Wearable medical devices have revolutionized the field of medical sciences and have improved the quality of life of both diseased and healthy persons. They can be used for vital signal monitoring of patients as in Wireless Body Area Networks (WBAN) and can alert doctors about the critical condition of their patients. These devices can be used for rehabilitation of patients with disability, and also by healthy people without any disease or disability, e.g., by sportsmen and athletes. The main advantage of the wearable devices is that they are non-invasive and have limited risk of infection [1], [2].

The wearable medical devices placed at different positions on the body may communicate with each other for data exchange. In such scenarios, on-body propagation model become critical for proper estimation of the link budget. Various statistical and analytical on-body propagation models have been discussed in [3]-[8]. In [3], a time domain analysis and modeling of the on-body propagation characteristics was presented. The measurements were done in different scenarios like anechoic chamber, open office area, hallway, and outdoor environment, and autocorrelation and cross-correlation statistics of various on-body channels were presented at 2.45 GHz. The time-variant statistics for different on-body channels presented in this paper are useful for developing statistical channel models. In [4], a simplified physical body area propagation model was derived using Maxwell's equations. The body was approximated by a circular lossy cylinder. For around the body propagation, it was shown that the waves are guided by the curved surface and attenuate exponentially with the distance. Such waves are called creeping waves. A channel model for wireless communication around the human body was developed in [6]. FDTD simulations using vertically polarized dipole antenna at eight different heights along the body with 15 radial points around the body for each height were done. The model was then derived by fitting lines minimizing the mean square error of the data points. It was found that the model has exponential attenuation which corresponds to the creeping wave phenomenon. The attenuation of the creeping waves was found from the slope of the fitted line. An analytical propagation model of BAN channels based on the creeping wave theory was presented in [7] by re-using the theory of the wave propagation over the inhomogeneous earth's surface [9]. However, these research results either don't show a closed form analytical expression for the creeping wave's attenuation which is derived from the fitted model specific to the dimension of the phantom used, or is developed by treating the human body as having a circular cross-section. Hence, further investigation is needed for the attenuation of the creeping waves over more realistic cross-section of the human body.

Hearing aids are one such wearable medical device which is used for rehabilitation of hearing impaired persons. Binaural hearing aids are a system where there is a hearing aid in both the ears of the user. They communicate with each other for synchronization data through the ear-to-ear on-body propagation channel [10]. The ear-to-ear propagation channel has been discussed in [11]-[17]. In [11] it was shown that diffraction is the main propagation mechanism around the head for the link between the ears. This diffraction mechanism is the same as the creeping wave phenomenon. It was shown in our previous work [10] that in-the-ear (ITE) placement has less attenuation than in-the-canal (ITC) placement of the binaural hearing aids as the communication between the ITE antennas was through the creeping waves. In [13], the effect of the head size on the ear-to-ear radio propagation channel was examined. It was shown by simulations that the variations in the head size may result in up to 10 dB variation in the link loss. In [14], authors have shown by measurements with different antennas on the physical SAM (Specific Anthropomorphic Mannequin) head that small variations in the position of the antenna do not affect the ear-to-ear link loss whereas the operating frequencies have a larger impact on the link loss. Their result showed that the link loss increases with increase in the frequency. The importance of the correct orientation of the antenna to decrease the link loss was also shown. Homogeneous models were used for the simulations or for the measurements. The protruding part of the outer ear called pinna and the lossy skin are absent in the SAM head/homogeneous head. However, in [17] we have shown the significant effect of the pinna and the lossy skin on the ear-to-ear link loss. An analytical propagation model for the communication between the ITE binaural hearing aids is required for proper estimation of the ear-to-ear link loss. The analytical model for the propagation around the head presented in [7], can be used for this purpose. Since the model was developed for a simplified model of the head, treating it as a circular cylinder, there was a good agreement between the simulations and the measurements. However, this model does not take into account the losses due to the pinnas.

In this paper, we have presented an analytical model which includes the losses of the pinnas. The cross-section of the head is modeled as a more realistic elliptical shape rather than a circular shape. It is shown that the two paths of the creeping waves are sufficient to describe the link loss. Simulations are done in SEMCAD-X [18] which uses the FDTD method. A low-profile and compact ITE antenna [17] on the heterogeneous phantoms is used to verify the analytical propagation model. Measurements are done to verify the effect of the pinna on the ear-to-ear link loss. Both the simulations and the measurements are done in the 2.45 GHz ISM band.

The paper is organized as follows. In Section 2, the numerical phantoms used for the simulations are described. A brief summary of the antenna used for the simulations is given in Section 3. Section 4 present the analytical model.

Other factors apart from the pinna which may effect the ear-to-ear link loss are discussed in Section 5. In Section 6, the measurement process and results are presented. Conclusions are presented in Section 7.

2 Numerical Phantoms

Four numerical heterogeneous phantoms of different age group and gender, and one homogeneous phantom, are used for the simulations. The modified SAM head phantom with the ear canals [10], shown in Fig. 1(a), is used as a homogeneous phantom. Average homogeneous electrical properties of tissues in human head (relative permittivity, $\varepsilon_r = 39.2$ and conductivity, $\sigma_e = 1.80$ S/m) at 2.45 GHz are assigned to the SAM phantom. The ear canal is modeled as an air filled cylindrical tube of diameter 7 mm and length 26 mm. The heterogeneous numerical phantoms used in this paper are provided by ITIS foundation [19] developed for the Virtual Family and Classroom project [20]. They are whole body anatomical models consisting of more than 80 tissues with different electrical properties. The models are those of a 34 year old male called Duke, a 26 year old female called Ella, a 15 year old boy, Louis, and a 11 year old girl, Billie. They are shown in Fig. 1(b). Since we are interested in the ear-to-ear link loss, only the truncated head with the neck of the phantoms are used for the simulations. This also has an advantage in terms of faster simulation. However, we have examined and presented the effect of the shoulders on the link loss. Table 1 presents the electrical properties of the tissues present in the head and the neck of the phantoms at 2.45 GHz. Tissue is the name of the tissue of the phantom of Virtual Family Project and Gabriel list gives the mapping of the phantom tissue to the Gabriel list obtained from [21] for the electrical properties. The approximate head dimensions of the phantoms are shown in Table 2 where the dimensions l, h, s are shown in Fig. 1.

3 Antenna

The ITE antenna introduced in [10] and optimized for Duke at 2.45 GHz with dimensions given in [17] is used in this paper for the simulations. The antenna is placed normal to the head surface in the ear as shown in Fig. 2. The antenna detunes differently for different phantoms, and for different ears within the same phantom. However, the antenna remain well matched at 2.45 GHz. The return loss of the ITE antenna at 2.45 GHz for different phantoms are shown in Table 3.

Table 1: Tissue Parameters

Tissue	**Gabriel List**	ε_r	σ_e **(S/m)**
Air Internal	Air	1	0
Artery	Blood	58.26	2.54
Blood Vessel	Blood	58.26	2.54
Bone	Bone Cortical	11.38	0.39
Brain Grey Matter	Brain Grey Matter	48.91	1.80
Brain White Matter	Brain White Matter	36.16	1.21
Cartilage	Cartilage	38.77	1.75
Cerebellum	Cerebellum	44.80	2.10
Cerebrospinal fluid	Celebro Spinal Fluid	66.24	3.45
Commissura anterior	Brain White Matter	36.16	1.21
Commissura posterior	Brain White Matter	36.16	1.21
Connective tissue	Tendon	43.12	1.68
Cornea	Cornea	51.61	2.29
Ear Cartilage	Cartilage	38.77	1.75
Ear Skin	Skin (Dry)	38.00	1.46
Eye Lens	Lens Cortex	33.97	1.09
Eye Sclera	Eye Tissue (Sclera)	52.62	2.03
Eye vitreous humor	Vitreous Humor	68.20	2.47
Fat	Fat	5.28	0.10
Hippocampus	Brain Grey Matter	48.91	1.80
Hypophysis	Gland	57.20	1.96
Hypothalamus	Gland	57.20	1.96
Intervertebral disc	Cartilage	38.77	1.75
Larynx	Cartilage	38.77	1.75
Mandible	Bone Cortical	11.38	0.39
Marrow Red	Bone Marrow (infiltrated)	10.30	0.45
Medulla Oblongata	Brain (average)	42.53	1.51
Midbrain	Brain (average)	42.53	1.51
Mucosa	Mucous Membrane	42.85	1.59
Muscle	Muscle	52.73	1.74
Nerve	Nerve	30.14	1.08
Pharynx	Air	1	0
SAT	Fat	5.28	0.10
Skin	Skin (Dry)	38.00	1.46
Skull	Bone Cortical	11.38	0.39
Spinal Cord	Spinal Chord	30.14	1.08
Teeth	Tooth	11.38	0.39
Tendon Ligament	Tendon	43.12	1.68
Thalamus	Brain Grey Matter	48.91	1.80
Thymus	Thymus	57.20	1.96
Thyroid gland	Gland	57.20	1.96
Tongue	Tongue	52.62	1.80
Vein	Blood	58.26	2.54
Vertebrae	Bone Cortical	11.38	0.39

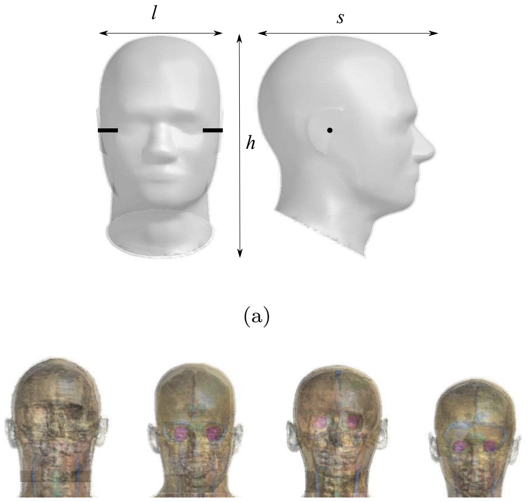

(a)

(b)

Figure 1: Phantoms (a) Modified SAM Head with ear canals [10] (b) Heterogeneous Phantoms (only the truncated head part is shown here). From L to R: Duke, Ella, Louis, Billie

Table 2: Dimensions of the phantom's head

Phantom	Age (year)	Gender	l (mm)	h (mm)	s (mm)
SAM	–	Male	164	312	234
Duke	34	Male	155	251	238
Ella	26	Female	143	239	209
Louis	15	Male	152	241	214
Billie	11	Female	137	233	188

For l, h and s see Fig. 1

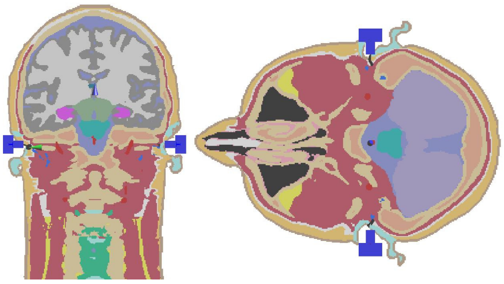

Figure 2: Placement of the antennas in the ear [17]

Table 3: Return Loss of the ITE Antenna on Different Phantoms at 2.45 GHz

Phantom	Left Ear (dB)	Right Ear (dB)
SAM	15	15
Duke	24	9
Ella	13	11
Louis	12	13
Billie	12	11

4 Link Loss Model

It is well established that the creeping wave is the dominant phenomenon for the communication around the curved part of the body. In [7] and [22], it was shown that the clockwise and the anti-clockwise creeping wave interfere with each other. The phantom in these investigations was symmetrical. However, the realistic phantoms are anatomically asymmetric and hence for the ear-to-ear channel there will be several paths such as over top of the head, over back of the head, over the front part of the head, etc. Investigations are done through simulations to determine the dominant paths i.e. the ones having most of the power of the creeping waves.

4.1 Dominant Paths of the Creeping Waves

The creeping waves from the transmitter in one ear can reach the receiver in the other ear by numerous paths. But it is not necessary that all these paths will have significant power as some paths will have high attenuation. Six different simulation cases are considered to determine the paths having significant power using the ITE antenna on Duke phantom. In these cases, one or more creeping paths are truncated by an uniaxial perfectly matched layer (UPML) such that the creeping waves are blocked on these paths. The descriptions of the cases are presented in Table 4. The table lists the creeping paths and the blocked paths for the six cases. For example, for case (a), simulation domain includes the front and the top part of the head, allowing the waves to creep over these paths and truncating the back side of the head with an UMPL which blocks the creeping waves on the back side of the head. It should be noted here that the front, the back and the top are relative position w.r.t. the ear (antenna placement). These six cases are illustrated in Fig. 3 where the shadowed region represents the simulation domain. The link loss of all these cases is compared with the link loss when the complete head is used in the simulation domain. The simulation results are shown in Fig. 4. Throughout the paper we present the plot of $S_{21}|_{dB}$ which is related to the link loss (LL) in dB scale by: $LL|_{dB} = -S_{21}|_{dB}$. It should be noted that the frequency band of interest is 2.45 GHz ISM band and hence all the comparison are done in this band where the antennas are matched to 50 Ω source impedance. At other frequencies like around 2 GHz and 2.9 GHz, there are extreme dips in the simulated S_{21} for some scenarios which is either because of the high mismatch loss at these frequencies, or due to strong destructive interference of waves coming from different paths. However, since these are not the frequencies of the interest, no further investigations are done for these extreme dips in the simulated S_{21}.

Table 4: Simulation cases for determination of dominant path of creeping waves between the ears

Scenario	Creeping Path	Blocked Path
Case (a)	Front and Top	Back
Case (b)	Top	Front and Back
Case (c)	Top and Back	Front
Case (d)	Front and Back	Top
Case (e)	Front	Top and Back
Case (f)	Back	Front and Top

The difference between the link loss with these six simulation cases and the complete head is shown in Table 5 at 2.4 GHz, 2.45 GHz and 2.5 GHz where $\Delta S_{21} = S_{21}|_{complete\_head} - S_{21}|_{UPML}$. A positive ΔS_{21} means increase in the link loss and a negative ΔS_{21} means decrease in the link loss when compared to the actual case when the complete head is included. It can be seen that

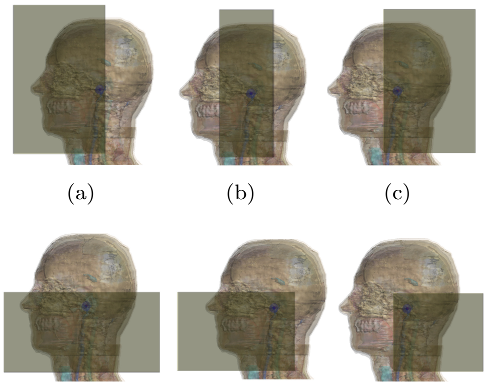

(a) (b) (c)

(d) (e) (f)

Figure 3: Duke head with the simulation domain for determining dominant creeping path. Shadowed region is the simulation domain. (a) Creeping path: front and top; Blocked: back (b) Creeping path: top; Blocked: front and back (c) Creeping path: back and top; Blocked: front (d) Creeping path: front and back; Blocked: top (e) Creeping path: front; Blocked: top and back (f) Creeping path: back; Blocked: front and top

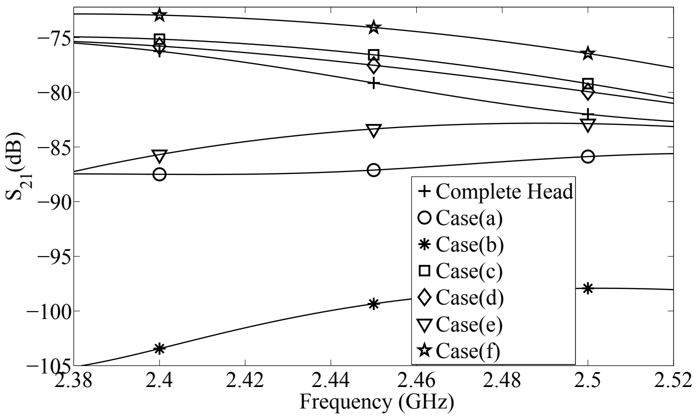

Figure 4: S_{21} for different scenarios for determining the paths of the creeping waves carrying significant power in the ISM band. For the description of the cases in the legend refer to Table 4 and Fig. 3.

Table 5: Difference between the link loss with and without UPML

Scenario	ΔS_{21}(dB) [2.4 GHz]	ΔS_{21}(dB) [2.45 GHz]	ΔS_{21}(dB) [2.5 GHz]
Case (a)	11.3	8.0	3.9
Case (b)	27.2	20.3	15.9
Case (c)	-1.1	-2.5	-2.8
Case (d)	-0.4	-1.6	-2.1
Case (e)	9.5	4.2	0.8
Case (f)	-3.3	-5.0	-5.6

whenever the back of the head is excluded from the simulation boundary (cf. case (a), (b), (e)) so that no wave creeps over the back side of the head, the link loss increased by 4.2-20.3 dB at the central frequency of 2.45 GHz. From this, it can be concluded that the creeping wave propagating over the back of the head is the strongest. This can also be confirmed by case (f) as the link loss is lowest when only back path is included. However, when the top of the head is excluded from the simulation boundary as in case (d), the link loss decreased by 1.6 dB at 2.45 GHz. Hence, the top creeping wave does not carry any significant power. This observation is also supported by the increase in the link loss by 20.3 dB at 2.45 GHz in case (b) where the waves creeps only over the head top. In case (d), where the front and the back of the head is included, the difference is small. Hence, the front and the back path carry most of the significant power. With these observations we can conclude that the two paths, one going around the back and the other going around the front part of the head should give a good estimation of the ear-to-ear link loss.

4.2 Effect of the outer lossy skin and the Pinna

The presence of the outer lossy skin and the pinnas on the heterogeneous phantoms introduces extra loss when compared with the SAM head. In [17], it was shown that for low profile antennas which are very close to the head surface, the loss because of the pinnas could be up to 13 dB. The presence of the pinnas may introduce an additional loss as the strongest creeping wave which creeps over back part of the head passes through them and hence gets attenuated. The loss because of the pinnas could be theoretically calculated by the sum of the propagation loss in a lossy medium (pinna) and the reflection loss as described in [17].

To verify the effect of the pinnas on the ear-to-ear link loss, an approximate pinna is modeled for the SAM phantom with the lossy shell having the electrical properties same as that of the SAM liquid which are approximately same for the ear-cartilage of the Duke phantom. The electrical properties of the pinna is assigned the same values (relative permittivity, $\varepsilon_r = 39.2$ and conductivity, $\sigma_e = 1.8$ S/m) as the SAM liquid to maintain the homogeneity. The height of the pinna is taken as 18 mm which is same as that of the pinna in the Duke phantom. A semicircular structure of the pinna resulted in 7 dB further increment in the link loss whereas a more realistic structure of the pinna resulted in 11 dB increment in the link loss as shown in Fig. 5 [17].

A reverse methodology is implemented to verify the effect of the pinnas and the lossy skin on the Duke phantom. The tissues of the ear in the Duke phantom, namely, the ear cartilage and the ear skin (see Table 1) is assigned the electrical properties of air. This is done to remove the effect of the pinna. It resulted in decrease of the ear-to-ear link loss by 8 dB at 2.45 GHz. Next, the skin of the phantom (which is the outer most layer) is assigned the electrical properties of lossless SAM shell (relative permittivity, $\varepsilon_r = 3.7$ and conductivity, $\sigma_e = 0$). This further decreased the link loss by 13 dB at 2.45 GHz. The effects are illustrated in Fig. 6.

The link loss for the SAM phantom with realistic pinnas and a lossy shell approaches to that of the Duke phantom in the ISM band as seen in Fig. 5. Moreover, the reverse methodology shows the significant effect of the pinnas and the lossy skin on the ear-to-ear link loss. Hence, it can be concluded that any numerical or real phantom with an outer lossless shell should be used with a caution while estimating the link loss for the on-body propagation and that the homogeneous phantoms should have a lossy outer shell. The phantoms should have the pinnas to get more accurate estimate of the ear-to-ear link loss. The shape of the pinna is also critical as more realistic pinna model estimates more accurate results.

With the observations that the two paths of the creeping waves, namely, the front path and the back path are sufficient to describe the ear-to-ear link loss and the significant effect of the pinna and the lossy skin on the link loss, the analytical model for the ear-to-ear link loss is developed in the next section.

4.3 Complete Link Loss Model

In this section the ear-to-ear link loss analytical model based on the creeping wave is developed. The model is for low profile antennas such that the height of the antenna above the body surface is negligible. The head is approximated by a more realistic elliptical cross-section rather than a circular cross-section. The elliptical approximation is illustrated in Fig. 7 for Duke head. In [23], it was shown that the human body can be approximated by a metallic cylinder. Thus, the head is assumed to be metallic. The loss because of the waves creeping over the metallic surface is considered as an approximation for the waves creeping over the lossy medium. The lowest mode for the creeping wave is considered. A simpler version of the model for an elliptical approximation of the human torso is presented in our previous work [24]. For developing the analytical model, a heuristic approach is followed where the formulation of the attenuation of the field over an elliptical surface derived from the geometrical theory of diffraction [25] along with the reference field over a conducting plane [7] is used. The approach is validated by full wave FDTD simulations in [24] on the elliptical approximation of the human torso. It is valid for ellipse where a and b are comparable i.e. semi-major axis is not very different from semi-minor axis which is usually the case for a human torso and head. Here, the model with the additional effect of the pinna is presented.

The creeping wave field on the elliptical path can be written as

$$\mathbf{E} = \mathbf{E}_0 e^{-L}, \tag{1}$$

where the reference field $\mathbf{E}_0$ over the conducting plane for the vertical polarization at a distance s is given by [7]

$$\mathbf{E}_0 = 2\sqrt{\frac{\eta_0}{2\pi}} \frac{\sqrt{P_{TX} G_{TX}}}{s} e^{-jks}, \tag{2}$$

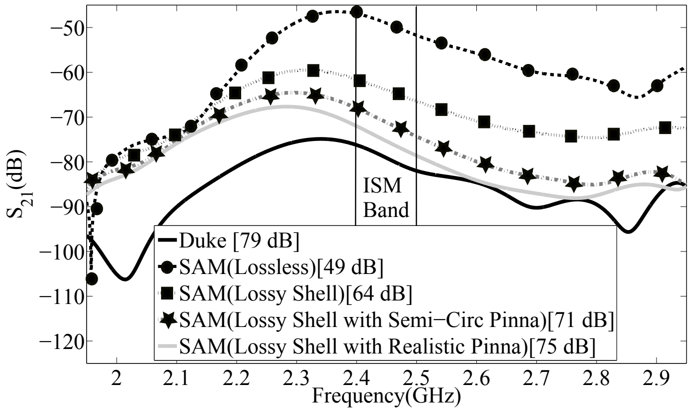

Figure 5: S_{21} for homogeneous vs. heterogeneous phantom using the ITE antenna [17]. The value in the square braces in the legend is the link loss at 2.45 GHz.

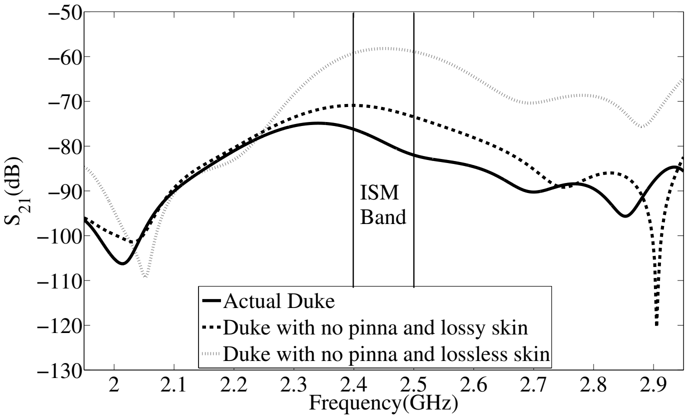

Figure 6: Effect of pinna and lossy skin on ear-to-ear link loss for Duke

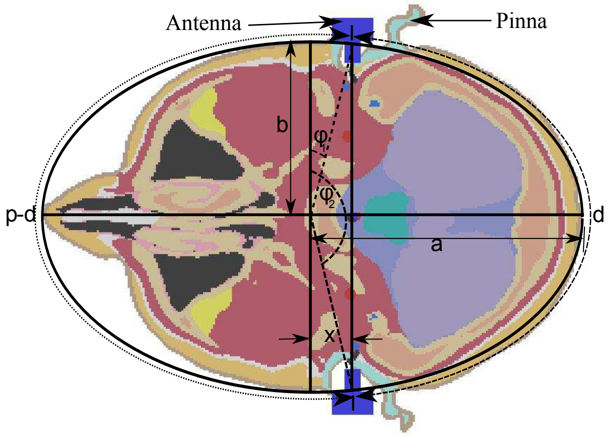

Figure 7: Elliptical fit for Duke in the transverse plane at the level of the antennas. $a = 115.8$ mm is the semi-major axis of the ellipse and $b = 75.1$ mm is the semi-minor axis of the ellipse. d is the length of the path of the creeping wave going over the back side of the head and p is the perimeter of the ellipse. x is the offset of the ears from the center of the ellipse.

where P_{TX} is the feeding power, $k = \frac{2\pi}{\lambda_0}$ is the wave number in the free space and G_{TX} is the gain of the transmitting antenna. η_0 is the wave impedance of the free space. L is the complex attenuation factor representing the loss on the surface. It is product of creeping distance and creeping attenuation per unit length. For the elliptical path over a metallic surface, it is given by [25]

$$L = \frac{(k)^{1/3}}{2} \left(\frac{3\pi ab}{4} \right)^{2/3} e^{\frac{j\pi}{6}} \int_{\varphi_1}^{\varphi_2} f(\varphi) \mathrm{d}\varphi, \tag{3}$$

where a is the semi-major axis and b is the semi-minor axis of the ellipse. φ_1 and φ_2 are the exit point angle at the transmitter and the trapping point angle at the receiver respectively as shown in Fig. 7. The integrand $f(\varphi)$ is defined as

$$f(\varphi) = \frac{ab}{\sqrt{[a^4 \cos^2 \varphi + b^4 \sin^2 \varphi][a^2 \cos^2 \varphi + b^2 \sin^2 \varphi]}}. \tag{4}$$

The total field at the receiver can be written as:

$$\mathbf{E} = \mathbf{E}_f + \mathbf{E}_b, \tag{5}$$

where the subscript f is for the wave creeping over the front part of the head and b is for the back of the head. $\mathbf{E}_f$ is given by:

$$\mathbf{E}_f = \mathbf{E}_{0f} e^{-L_f}, \tag{6}$$

where the reference field $\mathbf{E}_{0f}$ for the front part of the head is given by (2) with $s = p - d$, where p is the perimeter of the ellipse and d is the elliptical arc length between the ears at back side of the head (as shown in Fig. 7). The arc length, t, of the creeping wave between the angle φ_1 and φ_2 on the elliptical surface can be expressed as [25]:

$$t = ab \int_{\varphi_1}^{\varphi_2} \frac{(a^4 \cos^2 \varphi + b^4 \sin^2 \varphi)^{\frac{1}{2}}}{(a^2 \cos^2 \varphi + b^2 \sin^2 \varphi)^{\frac{3}{2}}} \mathrm{d}\varphi. \tag{7}$$

L_f can be calculated by (3) with the integration from $-\varphi_1$ to $\varphi_2 = \pi + \varphi_1$, where φ_1 is given by

$$\varphi_1 = \tan^{-1} \left[\frac{a}{b} \frac{x}{\sqrt{a^2 - x^2}} \right], \tag{8}$$

where x is the offset of the ear from the center of the ellipse as shown in Fig. 7. d can be calculated by substituting the proper values of φ_1 and φ_2 and p can be calculated by substituting $\varphi_1 = 0$ and $\varphi_2 = 2\pi$ in (7). The wave going over the back of the head has to pass through the pinnas and hence there will be reflection and absorption loss apart from the surface attenuation. E_b is given by:

$$\mathbf{E}_b = \mathbf{E}_{0b} e^{-L_b} T_{pinna}^2 e^{-2\alpha R}. \tag{9}$$

The reference field, $\mathbf{E}_{0b}$ is given by (2) with $s = d$. For L_b in (3), φ_1 is same as that in (8) and $\varphi_2 = \pi - \varphi_1$. T_{pinna} is the equivalent transmission coefficient for the air-pinna-air interface given by [26] as:

$$T_{pinna} = \frac{T_1 T_2 e^{-j\alpha_d}}{1 + \rho_1 \rho_2 e^{-2j\alpha_d}}, \tag{10}$$

where T_1 and T_2 are the transmission coefficient of the air-to-pinna and pinna-to-air interface respectively. ρ_1 and ρ_2 are the reflection coefficient of the air-to-pinna and the pinna-to-air interface respectively. α_d is the electrical length of the pinna with relative permittivity ε_r for the normally incident waves and is given by $\alpha_d = \frac{2\pi\sqrt{\varepsilon_r}R}{\lambda}$. Since the vertical polarization is dominant for the used antenna (described in the next section), TM waves are assumed. $e^{-\alpha R}$ in (9) represents the absorption loss in the pinna of average thickness R with $\alpha = |Im[k_{pinna}]|$ where k_{pinna} is complex wavenumber of the lossy medium (pinna). It should be noted that the terms T_{pinna} and $e^{-\alpha R}$ are squared to represent the effect of the both pinnas. The received power is

$$P_{RX} = \frac{|\mathbf{E}|^2 A_{RX}}{2\eta_0}. \tag{11}$$

Substituting $A_{RX} = G_{RX}\frac{\lambda^2}{4\pi}$ and $\mathbf{E} = \mathbf{E}_f + \mathbf{E}_b$, the link loss between the perfectly matched antennas in the dB scale can be written as:

$$LL|_{dB} = -10\log_{10}\left(\frac{P_{RX}}{P_{TX}}\right). \tag{12}$$

The detail equation of the link loss is

$$\begin{aligned} LL|_{dB} \quad = \quad -10\log_{10}\Bigg[\frac{G_{RX}G_{TX}\lambda^2}{4\pi^2}\Bigg(\Bigg|\frac{e^{-L_f}}{p-d}e^{-jk(p-d)} + \\ \frac{e^{-L_b}T_{pinna}^2 e^{-2\alpha R}}{d}e^{-jkd}\Bigg|\Bigg)^2\Bigg]. \end{aligned} \tag{13}$$

4.4 Verification of the Analytical Model

The analytical model is verified for the phantoms Duke, Ella, and Billie, having the largest, the medium and the smallest head, respectively. The parameters of Duke, Ella, and Billie head after the elliptical fit are described in Table 6. The values of L_f, L_b, creeping loss (losses excluding the gain of the antennas) and the total ear-to-ear link loss obtained from the analytical model are also shown. The gain of the antenna is the on-body antenna gain calculated from the simulations when the antenna is placed in the ear of the phantoms. The gain of the antenna in the azimuthal plane for the vertical polarized (solid line) and horizontal polarized (dot line) E-field is shown in Fig. 8 for Duke. It can be seen from the radiation pattern that the vertical polarization (normal to the head surface) is dominant. Moreover, the pattern is asymmetrical i.e. the two directions in which creeping waves exit or reach the antenna have different gain. Since the gain is the far-field gain, the asymmetry in the gain pattern is caused not just because of the pinna but also due to the anatomy of the whole head. As the antenna is placed in the ear, which is more towards the back side of the head, the far-field gain has slightly lower value on this side due to less lossy tissues of the head seen by the antenna on this side. For all the phantoms, the simulated gain is found slightly higher on the back side of the head, as can be seen for Duke phantom in Fig. 8. The consequence of using the far-field gain for the creeping wave is discussed in Section 4.5. Moreover, the two antennas on different ears have different gain due to the mismatch. Hence, the highest gain of the two antennas at 0° is taken as the model assumes perfect match. The comparison between the simulated link loss and the link loss calculated with the analytical model in the ISM band is shown in Fig. 9. The difference between the analytical and the simulated link loss is within 4 dB for the phantoms showing a good agreement.

Additional verification is done at 2.45 GHz by increasing and decreasing the size of Duke and Billie head by 10%. It should be noted that scaling the head size resulted in slight change in the antenna gain apart from change in the head dimensions. A comparison between the simulation of scaled version of the heads and the analytical model is shown in Fig. 10. Again, a good agreement is achieved. However, as the head is scaled down, keeping the antenna size fixed, the difference between the simulation and the analytical model increases as can be seen at scale factor of 0.9 (decrease in head size by 10%). This is because of the fact that scaling down resulted in smaller pinna which do not fully obscure the EM waves.

4.5 Limitations and Discussions about the Analytical Model

The analytical model gives the deterministic component of the ear-to-ear link loss. In the indoor scenarios where multi-path components (MPCs) are present, the link loss could be higher or lower depending upon the interference of the

Table 6: Parameters of the Analytical Model

Freq.(GHz)	Gain(dBi)	L_f	L_b	CL[*](dB)	LL[†](dB)
Duke: $a = 115.8$ mm, $b = 75.1$mm, $p = 609.7$ mm, $d = 270.8$ mm, $x = 17$ mm, $R = 5$ mm, $\phi_1 = .225$ rad					
2.4	-10.0	4.30+2.48i	3.69+2.13i	61.34	81.34
2.45	-9.95	4.33+2.50i	3.72+2.15i	61.80	81.70
2.5	-10.2	4.36+2.52i	3.74+2.16i	62.27	82.67
Ella: $a = 98.0$ mm, $b = 72.3$mm, $p = 538.1$ mm, $d = 249.0$ mm, $x = 10.0$ mm, $R = 4.5$ mm, $\phi_1 = .138$ rad					
2.4	-8.2	4.09+2.36i	3.66+2.11i	58.00	74.41
2.45	-8.5	4.12+2.38i	3.68+2.12i	58.42	75.42
2.5	-8.7	4.15+2.40i	3.71+2.14i	58.83	76.23
Billie: $a = 84.2$ mm, $b = 65.5$ mm, $p = 469.8$ mm, $d = 207.6$ mm, $x = 13.7$ mm, $R = 4$ mm, $\phi_1 = .209$ rad					
2.4	-7.0	4.05+2.34i	3.37+1.95i	56.40	70.40
2.45	-6.7	4.08+2.35i	3.39+1.96i	56.85	70.25
2.5	-6.6	4.10+2.37i	3.41+1.97i	57.29	70.49

[*] CL: Creeping Loss (losses excluding the antenna gain)

[†] LL: Total ear-to-ear link loss (including the antenna gain)

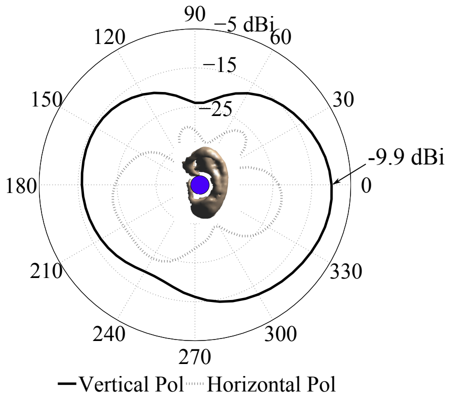

Figure 8: Gain Pattern of the antenna on Duke. Solid line is for the vertically polarized field w.r.t. the head surface and dotted line is for horizontal polarization. The pinna is shown in the azimuthal plane for the reference of the azimuthal angle.

MPCs. The model is valid for the antennas which are very close to the human body so that the dominant propagation mechanism is through the creeping waves. The elliptical fit of the head is done when the models are looking parallel to the transversal plane. Duke was looking parallel to the transversal

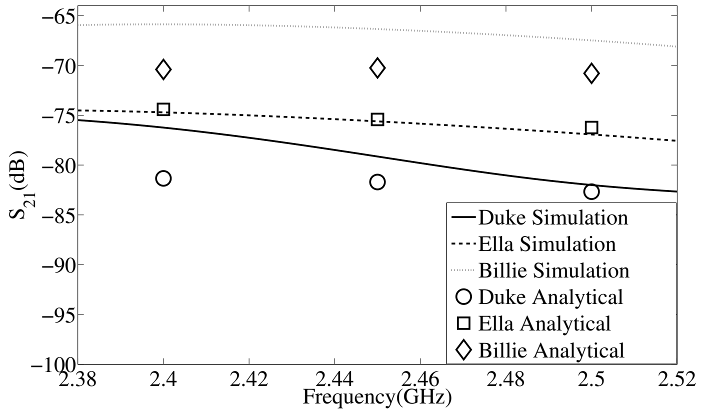

Figure 9: Simulated vs. Analytical S_{21} for Duke, Ella, and Billie in the ISM band.

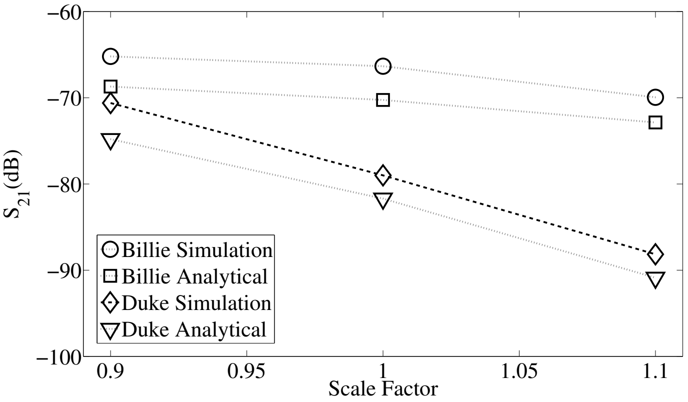

Figure 10: Simulated vs. Analytical S_{21} for different scale factor of Duke and Billie head.

plane at the ear level (xy plane in the simulations) but for Billie, the model is rotated by 5° to make her vision parallel to the xy plane. The gain of the antenna is also critical as it is difficult to measure with the body [7], but could result in significant difference in the link loss. The difference in the link loss from the analytical model between Duke and Billie is about 11 dB at 2.45 GHz.

5 dB out of this 11 dB is the difference in the creeping loss attributed to the difference in the head size and the ear thickness. The rest 6 dB is due to the difference in the gain of the antennas. Hence, a more appropriate method of calculating the gain of the antennas with the body may result in more accurate results. Moreover, as discussed in [24], there is no well defined measure (to best of our knowledge) such as the gain for the coupling from the antenna to the creeping wave over the human body which involves near-field effects. Hence, using the standard gain which is calculated in far-field is an effective approximation.

Difference in the analytical model and the simulations may also arise due to elliptical approximation of the human head as a real head does not have a perfect elliptical cross-section. Moreover, the model assumes the attenuation of the creeping waves over a perfectly conducting surface whereas the layers of the lossy tissues of the head may have an additional effect on the losses. Nevertheless, in spite of these assumptions and limitations, a good agreement between the analytical model and the simulations is observed showing the possibility of using the analytical model for estimation of the ear-to-ear link loss.

5 Other Factors Affecting the Ear-to-Ear Link Loss

5.1 Effect of Different Head Sizes

The effect of the head size on the ear-to-ear propagation channel has been discussed in [12], [13] and [17]. In our previous work [17], we have shown by simulations on the heterogeneous phantoms that different head size will have different link loss as shown in Fig. 11. The link loss difference between Duke and Ella is about 3 dB, between Duke and Louis is 6 dB, and between Duke and Billie is about 12 dB at 2.45 GHz where the antenna is still matched. The difference in the link loss between different phantoms can be attributed to the fact that the different head size will result in different path lengths of the creeping waves going behind the head and front of the head and also because of the gain variations of the antenna resulting from anatomical variations in different phantoms.

5.2 Effect of the Shoulders

The shoulders may also affect the ear-to-ear link loss as the reflections from the shoulders may result in multipath components interfering either constructively or destructively with the creeping waves resulting in different power levels. The

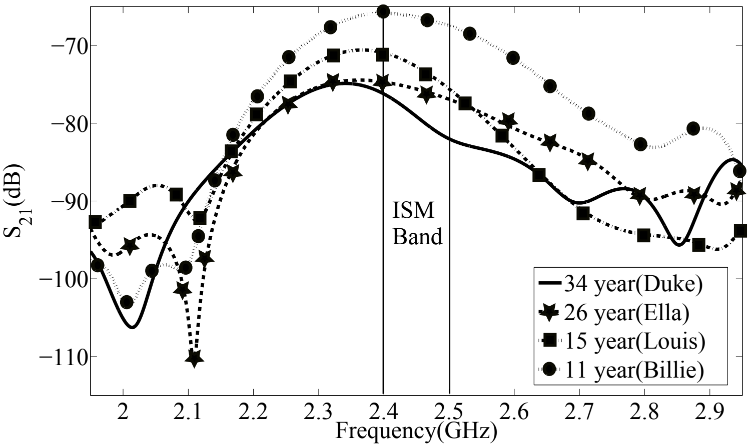

Figure 11: S_{21} for different phantoms [17]

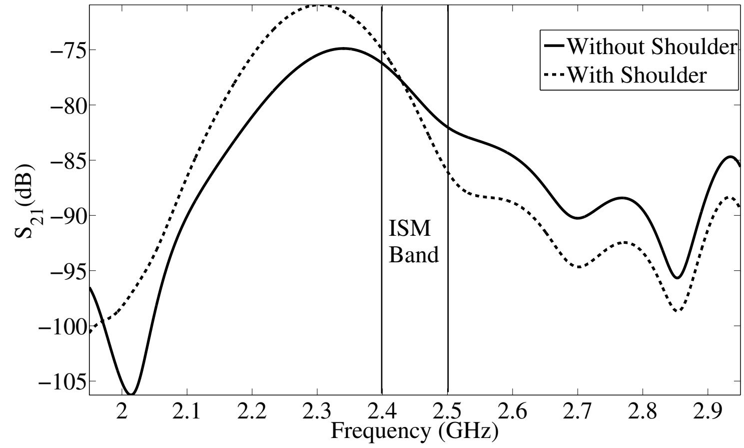

Figure 12: S_{21} with shoulders and without shoulders for Duke phantom [17]

effect of the shoulders on Duke phantom can be observed in Fig. 12. It can be seen that the difference between the link loss with and without the shoulders is within 2 dB in the ISM band. Thus, there is a possibility to exclude the shoulders in order to decrease the simulation time [17].

6 Measurements

Measurements are carried out to verify the effect of the pinna. The measurement setup and the measured scenarios are described below.

6.1 Measurement Setup

The phantom shown in Fig. 13 is used for the measurements. The phantom is hollow and is filled with the tissue stimulating liquid mimicking the average electrical properties of the human head tissues at 2.45 GHz (ε_r = 39.2 and σ_e = 1.80 S/m). The tissue stimulating liquid is prepared according to the recipe discussed in IEEE Std. 1528-2003 [27]. The electrical properties of the tissue stimulating liquid are measured by Agilent 85070D dielectric probe kit using open ended coaxial probe. The measured result in the ISM band is shown in Fig. 14. The mean value for measured relative permittivity ε_r is 39.2 and that for conductivity σ_e is 2.0 S/m in the ISM band, showing a good agreement with the theoretical target values (ε_r = 39.2 and σ_e = 1.8 S/m). The phantom does not have the pinnas. External pinnas are manufactured and attached to the phantom. The measured scenarios are (a) ear-to-ear link loss without the pinnas (b) ear-to-ear link loss with the pinna. Return loss of the antennas are also measured in all these scenarios. The measurement is done in an anechoic chamber of the EIT department, Lund University. S-parameters, S_{11} and S_{21}, are measured at 1601 frequency points in 1.95 GHz to 2.95 GHz frequency band using HP-8720C Vector Network Analyzer (VNA). The output power is set to -10 dBm. TOSM calibration is done to calibrate the VNA using a fabricated calibration kit. The calibration kit is fabricated in order to remove the effect of the semi-rigid cable which is attached to the antenna. The cables are placed tangentially to the head surface in order to have minimal influence of the spurious radiation, if any, from the cables. This is done as the current in the cables will generate the electric field which is tangential to the head surface and will have higher attenuation compared to the vertical component of the field from the antennas.

6.2 Fabricated Pinna

The pinnas are commercially fabricated by the 3D-printing technology by Shapeways [28]. Nylon plastic is used as the material. The measured mean value of ε_r of the plastic is 2.4 and that of σ_e is 0.004 S/m as shown in Fig. 14. Since the plastic used for fabricating the pinnas has very low dielectric properties, it would not have a significant effect on the link loss. The pinnas are hollow from inside and holes are made on them to facilitate the filling of the

Figure 13: Phantom used for the measurement. The placement of the antennas and the pinna can also be seen.

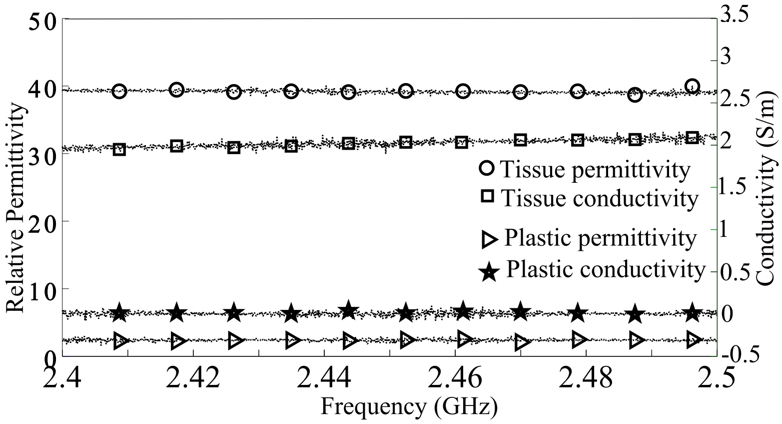

Figure 14: Measured electrical properties of the plastic used for fabricating pinna and the tissue stimulating liquid. The relative permittivity is shown on the left y-axis and the conductivity on the right y-axis.

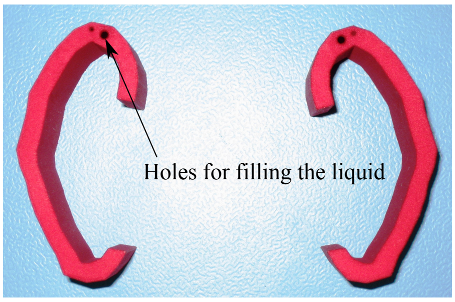

Figure 15: Pinnas fabricated by the 3D-printing

hollow pinnas with the tissue stimulating liquid. After filling the pinnas with the liquid, the holes are closed with a glue gun. The pinnas are glued on the phantom with the help of 1 mm thick double sided tape made of foam plastic. The fabricated pinnas are shown in Fig 15. The thickness of the plastic wall of the pinnas is 1 mm and the air-spacing in which the tissue stimulating liquid is filled is 2.5 mm. The pinnas protrude 24 mm from the head surface and have a length of 58 mm. The phantom with the pinna and the antenna placement is shown in Fig 13.

6.3 Antennas

A monopole antenna is designed and optimized on the SAM phantom with the pinnas to work in 2.45 GHz band. The antenna is loaded with a disc and then the disc is shorted to the ground plane to miniaturize the size and make the antenna low profile. The fabricated antenna with the dimensions is shown in Fig. 16. The central conductor of the semi-rigid coaxial cable, UT-85-H-M17 provided by Rosenberger [29] is used as the central conductor in the monopole antenna. The outer conductor is then soldered to the ground plane of the antenna (also shown in Fig. 16). The length of the cable is 1 m with the SMA connector at the other end of the cable. Hence, the calibration kit is fabricated to remove the effect of this semi-rigid cable. The semi-rigid cable has outer diameter of 2.2 mm. It is used in order to place the antenna close to the head because directly attaching the SMA connector to the antenna could have resulted in much more air gap between the antenna and the head. The ground plane and the loading disc are etched out from a Teflon laminate of 0.8 mm thickness having 0.35 μm thick copper layer.

The simulated and the measured reflection coefficient ($S_{11}|_{dB}$) of the fabricated antenna on the phantom with and without the pinnas are shown in

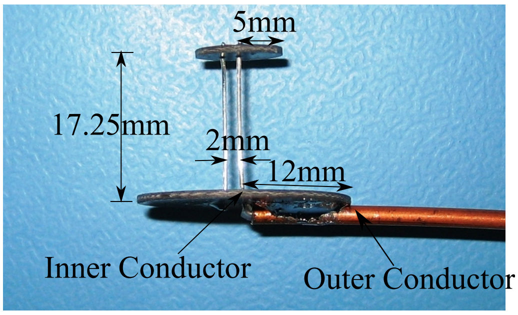

Figure 16: Fabricated Antenna

Fig. 17. It could be seen that the presence of the pinna improves the matching. The difference between the simulated and the measured reflection coefficient can be attributed to the fact that the antenna is optimized over the SAM phantom with a lossy shell whereas the phantom used for the measurement has an outer lossless shell. Some mismatch also occurs due to the cable attached to the antenna. The shift in the resonance frequency can be observed when the antenna is placed over the phantom when compared to the free space. The simulated antenna gain in the azimuth plane (plane of the head surface) with the phantom and in the free space is shown in Fig. 18. It can be seen from the figure that the antenna is vertically polarized and the presence of the phantom decreases the gain.

6.4 Measured Results and Discussions

As shown in Fig. 17, the antenna is mismatched when placed on the phantom without the pinna but the presence of the pinna improves the matching. The mismatch loss in the absence of the pinnas are removed from the measured S_{21} for proper comparison by treating the return loss in the presence of the pinnas as the reference. This is done as:

$$|S_{21}|_{no\_pinna}|^2 = |S_{21}|_{no\_pinna}|^2_{meas} \times F, \tag{14}$$

where F is the correction factor for removal of the mismatch loss without the pinna with the antenna with the pinna as the reference, given by:

$$F = \frac{(1 - |S_{11}|^2_{pinna}) \times (1 - |S_{22}|^2_{pinna})}{(1 - |S_{11}|^2_{no\_pinna}) \times (1 - |S_{22}|^2_{no\_pinna})}, \tag{15}$$

where $|.|$ represents the absolute value of the S-parameters in linear scale.

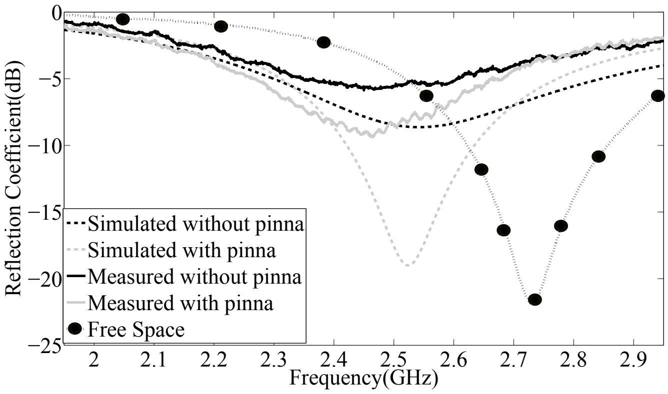

Figure 17: Simulated and measured reflection coefficient of the fabricated antenna. The simulation is done on the SAM head and the measurement on the phantom shown in Fig. 13. Simulated reflection coefficient in free space is also shown.

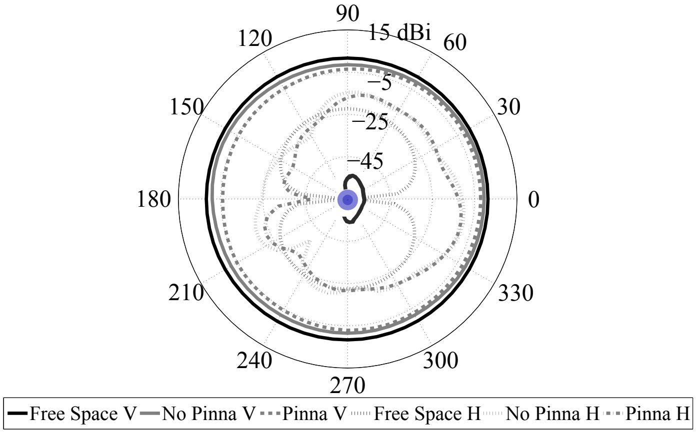

Figure 18: Simulated gain of the antenna in free space and on SAM head with and without the pinna in the azimuthal plane. V: Vertical polarization w.r.t. the head surface and H: Horizontal polarization w.r.t the head surface.

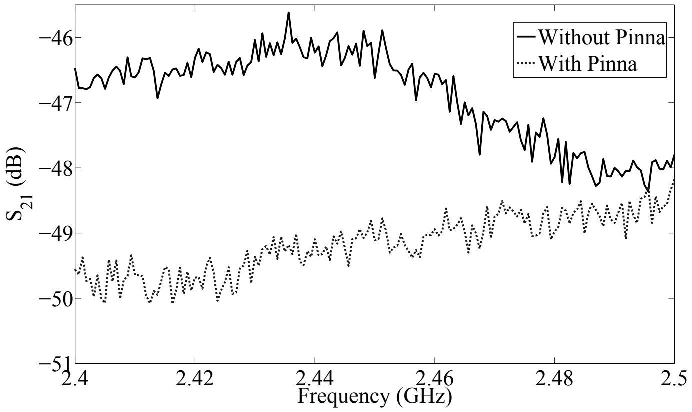

Figure 19: Measured S_{21} with and without the pinna in the 2.45 GHz ISM Band

The measured results are shown in Fig. 19. It can be seen that the link loss without the pinna is 4 dB less than the link loss with the pinna at 2.45 GHz. The difference is not as significant as discussed in Section IV-B. The possible reason for this could be the fact that the antennas used for the measurements are not low profile as the antennas used in simulations. Moreover, the phantom used for the measurement does not have the ear canals. Hence, the antennas are not shadowed to the extent as that in simulations. Further, the values of the link loss are lower than the numerical heterogeneous phantom as the phantom has a lossless shell of 2.5 mm with relative permittivity of 3.7. Hence, the effect of a lossless shell in decreasing the link loss can be observed as discussed in Section IV(B). Nevertheless, the increase in the link loss because of the pinnas can still be observed.

7 Conclusions

An analytical model based on creeping waves for the ear-to-ear link loss was presented. It is useful for estimating the deterministic component of the link loss between the transceivers for binaural hearing aids. The model takes into account the losses on the surface of the head, the loss due to the pinna and models the cross-section of the head with an elliptical shape. Through the simulations, it was observed that the two paths of the creeping wave, one going over the back of the head and the other in front of the head at the level of the ears were the dominant paths of the creeping waves carrying most of the power. Hence, a two path analytical model was developed. The verification of the model was done through the simulations on realistic heterogeneous phantoms of different age (34 year, 26 year and 11 year) and head size. Additional validation was done by increasing and decreasing Duke and Billie head by 10%. The difference between the model and the simulations was found to be within 4 dB in 2.45 GHz ISM band showing a good agreement. The main benefit of the model lies in fast estimation of the link loss when compared with time and memory consuming numerical simulations. With the estimated value of the link loss, the sensitivity of the hearing aids could be decided. A comparison between the numerical SAM phantom and a numerical heterogeneous phantom was done which showed a significant contribution of the pinna and the lossy skin in increasing the link loss by about 30 dB. The effect of the pinnas on the link loss was verified through measurement on a phantom where external pinnas manufactured by 3D-printing were attached. The measurement result showed a maximum increase in the link loss by 5 dB in the ISM band by the 3D-printed pinnas filled with the tissue stimulating liquid. Hence, for a proper calculation of the ear-to-ear link loss, the influence of the pinna and lossy skin has to be considered.

Acknowledgment

This research work has been done as a part of the project, Ultra Portable Device (UPD) for Wireless Communication. The authors would like to thank Swedish Foundation for Strategic Research (SSF) for funding the Ultra Portable Devices (UPD) project at Lund University.

References

[1] P.F. Binkley, “Predicting the Potential of Wearable Technology,” *IEEE Eng. Med. Biol. Mag.*, vol. 22, no. 3, pp. 23-27, June 2003

[2] A. Dittmar, R. Meffre, F. De Oliveira, C. Gehin, and G. Delhomme, “Wearable Medical Devices Using Textile and Flexible Technologies for Ambulatory Monitoring,” in *Proc. 27th Annu. Int. Conf. of the Eng. in Med. and Biology Soc.*, IEEE-EMBS 2005, pp. 7161-7164, 2005

[3] S.L. Cotton, G.A. Conway, and W.G. Scanlon, “A Time-Domain Approach to the Analysis and Modeling of On-Body Propagation Characteristics Using Synchronized Measurements at 2.45 GHz,” *IEEE Trans. Antennas Propagat.*, vol. 57, no. 4, pp. 943-955, Apr. 2009

[4] A. Fort, F. Keshmiri, G.R. Crusats, C. Craeye, and C. Oestges, “A Body Area Propagation Model Derived From Fundamental Principles: Analytical Analysis and Comparison With Measurements,” *IEEE Trans. Antennas Propagat.*, vol. 58, no. 2, pp. 503-514, Feb. 2010

[5] G. Roqueta, A. Fort, C. Craeye, and C. Oestges, “Analytical Propagation Models for Body Area Networks,” in *Proc. IET Seminar Antennas Propagat. for Body-Centric Wireless Commun.*, pp. 90-96, April 2007

[6] J. Ryckaert, P. De Doncker, R. Meys, A. de Le Hoye, and S. Donnay, “Channel model for wireless communication around human body,” *Electronics Lett.*, vol. 40, no. 9, pp. 543-544, April 2004

[7] T. Alves, B. Poussot, J.-M. Laheurte, “Analytical Propagation Modeling of BAN Channels Based on the Creeping-Wave Theory,” *IEEE Trans. Antennas Propagat.*, vol. 59, no. 4, pp. 1269-1274, April 2011

[8] G.A. Conway, W.G. Scanlon, S.L. Cotton and M.J.Bentum, “An analytical path-loss model for on-body radio propagation,” in *Proc. URSI Int. Symp. on Electromagnetic Theory*, pp. 332-335, Aug. 2010

[9] J.R. Wait, “The ancient and modern history of EM ground-wave propagation,” *IEEE Antennas Propagat. Mag.*, vol. 40, no. 5, pp. 7-24, Oct. 1998

[10] R. Chandra and A. J Johansson, “Miniaturized antennas for link between binaural hearing aids,” in *Proc. 32nd Annu. Int. Conf. IEEE Engg. Med. Biol. Soc., (EMBC’10)*, pp. 688-691, Aug. 2010

[11] T. Zasowski, G. Meyer, F. Althaus, and A. Wittneben, “UWB signal propagation at the human head,” *IEEE Trans. Microw. Theory Tech.*, vol. 54, no. 4, pp. 1836-1845, June 2006

[12] S.H. Kvist, J. Thaysen, and K.B. Jakobsen, “Investigation of the ear-to-ear radio propagation channel,” in *Proc. 5th Eur. Conf. Antennas Propagat. (EUCAP’11)*, pp. 3640-3644, April 2011

[13] S.H. Kvist, J. Thaysen, and K.B. Jakobsen, “The effect of the head size on the ear-to-ear radio-propagation channel for body-centric wireless networks,” in *Proc. Loughborough Antennas Propagat. Conf. (LAPC’10)*, pp. 345-348, Nov. 2010

[14] B. Nour and O. Breinbjerg, “Measurement and characterization of the path loss for ear-to-ear wireless communication,” in *Proc. 5th Eur. Conf. Antennas Propagat. (EUCAP’11)*, pp. 1621-1625, April 2011

[15] S.H. Kvist, J. Thaysen, K.B. Jakobsen, “Ear-to-ear on-body channel fading in the ISM-band for tangentially-polarized antennas,” in *Proc. Loughborough Antennas Propagat. Conf. (LAPC’11)*, Loughborough, Nov. 2011

[16] S.H. Kvist, J. Thaysen, K.B. Jakobsen, “Polarization of unbalanced antennas for ear-to-ear on-body communications at 2.45 GHz,” in *Proc. Loughborough Antennas Propagat. Conf. (LAPC’11)*, Loughborough, Nov. 2011

[17] R. Chandra, and A.J Johansson, “Influence on the ear-to-ear link loss from heterogeneous head phantom variations,” in *Proc. 5th European Conf. Antennas Propagat. (EUCAP’11)*, pp. 1612-1615, April 2011

[18] [Online]. Available: http://www.speag.com/products/semcad/solutions/

[19] [Online]. Available: http://www.itis.ethz.ch

[20] A. Christ et al., “The Virtual Family Development of anatomical CAD models of two adults and two children for dosimetric simulations,” *Phy. Med. Bio.*, vol. 55, no. 2, pp. N23-N38, Jan. 2010

[21] [Online]. Available: http://www.niremf.ifac.cnr.it/tissprop/

[22] A. Fort, J. Ryckaert, C. Desset, P. De Doncker, P. Wambacq, and L. Van Biesen, “Ultra-wideband channel model for communication around the human body,” *IEEE J. Sel. Areas Commun.*, vol. 24, no. 4, pp. 927-933, April 2006

[23] Yan Zhao, Yang Hao, A. Alomainy, and C. Parini, “UWB on-body radio channel modeling using ray theory and subband FDTD method,” *IEEE Trans. Microw. Theory Tech*, vol. 54, no. 4, pp. 1827-1835, June 2006

[24] R. Chandra, and A. J Johansson, “An Elliptical Link Loss model for Wireless Propagation around Human Torso,” in *Proc. 6th Eur. Conf. Antennas Propagat. (EUCAP’12)*, April 2011

[25] C. Balanis, and L. Peters, Jr., “Aperture radiation from an axially slotted elliptical conducting cylinder using geometrical theory of diffraction,” *IEEE Trans. Antennas Propagat.*, vol. 17, no. 4, pp. 507-513, Jul. 1969

[26] Andreas F. Molisch, *Wireless Communications*, IEEE Press/John Wiley & Sons, Ltd., 2009

[27] *IEEE Recommended Practice for Determining the Peak Spatial-Average Specific Absorption Rate (SAR) in the Human Head From Wireless Communications Devices: Measurement Techniques*, IEEE Standard 1528-2003, 2003

[28] [Online]. Available: http://www.shapeways.com/

[29] [Online]. Available: http://www.rosenberger.de/

Paper III

An Analytical Link Loss Model for On-Body Propagation Around the Body Based on Elliptical Approximation of the Torso with Arms' Influence Included

An analytical model for estimating the link loss for the on-body wave propagation around the torso is presented. The model is based on the attenuation of the creeping waves over an elliptical approximation of the human torso and includes the influence of the arms. The importance of including the arms' effect for a proper estimation of the link loss is discussed. The model is validated by the full-wave electromagnetic simulations on a numerical phantom.

R. Chandra and A. J Johansson,
"An Analytical Link-Loss Model for On-Body Propagation Around the Body Based on Elliptical Approximation of the Torso With Arms' Influence Included, " in *IEEE Antennas Wireless Propagat. Lett.*, vol. 12, pp. 528-531, 2013

1 Introduction

Wireless Body Area Network (WBAN) has emerged as a key technology in health care and consumer electronics [1]. The devices in WBAN can be broadly divided into two categories: (a) wearable or on-body (b) implantable. The communication between two wearable/on-body devices located on the opposite side of the body is through creeping waves [2]-[5]. Creeping waves undergoes exponential attenuation with the distance [3]. Hence, the estimation of the link loss between the on-body devices is essential for the link budget and deciding the sensitivity for a reliable wireless link. Statistical and deterministic propagation/link loss models for various WBAN scenarios are presented in [3]-[8]. The statistical approach models the link loss in a dynamic scenario when the body is moving [8] and the deterministic approach models the link loss in a stationary environment when the body is static [4]. The deterministic link loss is discussed in this letter.

The importance of the torso shape for correctly quantifying the path-loss around the body is discussed in [9]. An analytical model for the creeping wave propagation around the body based on a circular approximation of the cross-section of the torso is presented in [4] and for an elliptical approximation of the torso is presented in [5]. In [5], it is shown that a circular cross-section under-estimates the link loss. The effects due to the arms are excluded in the models presented in [4] and [5]. However, in [10], we have shown that there is a significant influence on the link loss due to the reflections from the arms. Usually, the arms are present at the side of the torso and will influence the deterministic link loss. Hence, a model which is easier to handle than time consuming simulations is needed to evaluate the effects of the arms on the wave propagation around the torso for designing a reliable link. The goal of this letter is to develop such a model by extending the analytical model presented in [5] to include the effects of the arms. The developed model is validated through the full-wave FDTD simulations done in SEMCAD-X [11] in 2.45 GHz ISM band.

2 Derivation of the Analytical Model

Let us consider a case shown in Fig. 1. The transmitter is fixed at the back side of the torso and the receiver is moved along the front side. The torso is shown by an ellipse and the arms are approximated by circle. In Fig. 1, $\mathcal{L}$ in the subscript is used for the left side of the torso and $\mathcal{R}$ for the right side of the torso. The coordinates and the parameters shown in Fig. 1 are described in Table 1. In the presence of the arms at the side of the torso, the electromagnetic

Parameter	Description
a; b	semi-major axis of the ellipse; semi-minor axis of the ellipse
p	perimeter of the ellipse (not shown in Fig. 1)
O(0,0)	Origin and center of the ellipse
$\mathrm{R}_n(x_{\mathrm{RXn}}, y_{\mathrm{RXn}})$	coordinates of the Rx at nth position
$\mathrm{T}(x_{\mathrm{TX}}, y_{\mathrm{TX}})$	coordinates of the Tx
d_{n}	anti-clockwise distance over ellipse from the Tx to R_n (not shown in Fig. 1)
φ_{n}	angle of the Rx at n^{th} position from the semi-minor axis on front side of body
$\mathrm{C}(x_{\mathrm{AC}}, y_{\mathrm{AC}})$	coordinates of the center of arm
u	distance between center of ellipse and arm
r	radius of the arm
α	angle between semi-major axis of ellipse and line joining center of arm with ellipse'e center
$\mathrm{Q}(x_{\mathrm{CE}}, y_{\mathrm{CE}})$	point of leave on ellipse where creeping ends
t_{TXQ}	distance over ellipse from Tx to the point of leave
φ_{CE}	angle between the TX and the point where creeping ends
$\mathrm{A}(x_{\mathrm{A}}, y_{\mathrm{A}})$	point of reflection on arm
s_{i}	distance between point of leave on ellipse and point of reflection on arm
$\mathrm{P}(x_{\mathrm{CS}}, y_{\mathrm{CS}})$	point of contact on ellipse where creeping again starts
s_{r}	distance between point of reflection on arm and point of contact
θ	angle of incidence/angle of reflection
t_{PRXn}	distance over ellipse from point of contact to Rx at n^{th} position
φ_{CS}	angle of the point of contact from semi-minor axis on front side of body

Table 1: Description of the Parameters for the Analytical Model

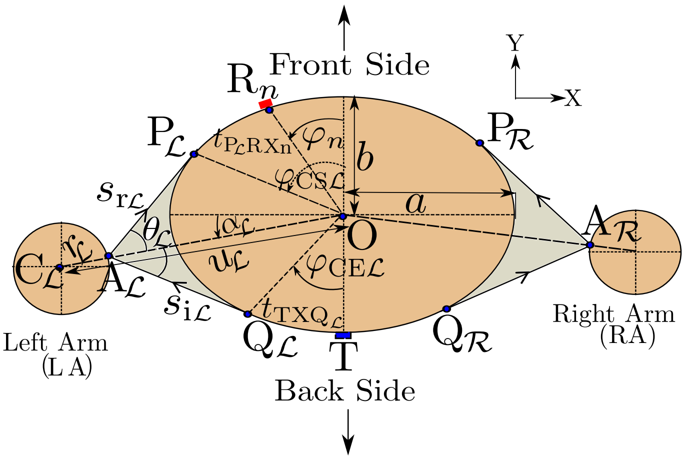

Figure 1: Cross-sectional view of the torso at the level of the antennas showing the parameters and coordinates. The parameters and the coordinates are described in Table 1.

(EM) waves from the transmit antenna (Tx) reaches the receive antenna (Rx) by two ways: (a) creeping wave starting at the Tx and then reaching the Rx through a clockwise and an anti-clockwise path around the torso and (b) waves leaving from the Tx directly or creeping for some distance over the torso and then leaving the torso tangentially at the point of leave (Q), getting reflected by the arms and reaching the Rx directly or after creeping from the point of contact (P).

2.1 Calculation of Parameters and Coordinates

The parameters which should be known are a, b, r, coordinates of the center of the arms and the position of the transmitter. All other parameters and coordinates are calculated from the coordinate geometry using these parameters.

The angle α is calculated as: $\alpha = \tan^{-1}(|y_{\mathrm{AC}}|/|x_{\mathrm{AC}}|)$. The x-coordinate of the point of reflection A is $x_{\mathrm{A}} = (u - r)\cos\alpha$ and the y-coordinate is $y_{\mathrm{A}} = (u - r)\sin\alpha$, where $u = \sqrt{x_{\mathrm{AC}}^2 + y_{\mathrm{AC}}^2}$. It should be noted that proper sign of the coordinates should be considered depending on the quadrant in which the arms are present. The tangents to the ellipse from the point of reflection $\mathrm{A}(x_{\mathrm{A}}, y_{\mathrm{A}})$ will have slopes, $m \in \{m_1, m_2\}$ given by:

$$m = \frac{x_{\mathrm{A}} y_{\mathrm{A}} \pm \sqrt{x_{\mathrm{A}}^2 b^2 + y_{\mathrm{A}}^2 a^2 - a^2 b^2}}{x_{\mathrm{A}}^2 - a^2} \tag{1}$$

The coordinates of the point of leave, $\mathrm{Q}(x_{\mathrm{CE}}, y_{\mathrm{CE}})$ and the point of contact, $\mathrm{P}(x_{\mathrm{CS}}, y_{\mathrm{CS}})$ is calculated by solving the tangents with the ellipse. s_i and s_r can then be calculated by distance formula between two points. With the knowledge of m_1 and m_2, angle between the tangents can be calculated. The angle of incidence/reflection, θ, is half of the angle between the tangents. Any angle φ between a line joining a point with x-coordinate x on an ellipse to the center and the minor axis can be calculated by:

$$\varphi = \tan^{-1}\left(\frac{a}{b}\frac{x}{\sqrt{a^2 - x^2}}\right) \tag{2}$$

From (2), angles φ_{n}, φ_{CS} and φ_{CE} can be calculated. The arc length t of an ellipse between any two angles φ_i and φ_j is given by [12]:

$$t = ab \int_{\varphi_i}^{\varphi_j} \frac{(a^4 \cos^2\varphi + b^4 \sin^2\varphi)^{\frac{1}{2}}}{(a^2 \cos^2\varphi + b^2 \sin^2\varphi)^{\frac{3}{2}}} \mathrm{d}\varphi \tag{3}$$

Using (3) and integrating between proper values of φ_i and φ_j, p, d_{n}, t_{TXQ} and t_{PRXn} can be calculated. For example, p can be calculated by integrating the expression in (3) between 0 and 2π and t_{PRXn} between φ_{n} and φ_{CS}.

2.2 Link Loss Model

The model is applicable for the attenuation of the vertical component of the creeping wave's electric field over a conducting elliptical path as discussed in [5]. The complex attenuation $L(\varphi_i, \varphi_j)$ over a conducting elliptical path between angles, φ_i and φ_j, for the vertical component of the electric field is [12]:

$$\begin{aligned} L(\varphi_1, \varphi_2) &= \frac{(k)^{1/3}}{2}\left(\frac{3\pi ab}{4}\right)^{2/3} e^{\frac{j\pi}{6}} \\ \cdot \int_{\varphi_1}^{\varphi_2} &\frac{ab}{\sqrt{[a^4\cos^2\varphi + b^4\sin^2\varphi][a^2\cos^2\varphi + b^2\sin^2\varphi]}} \mathrm{d}\varphi \end{aligned} \tag{4}$$

where k is the wave number in a free space. With arms at the side of the torso, there will be two additional paths apart from the clockwise and the anti-clockwise creeping path that will contribute to the received power as shown in Fig. 1. The first path $TQ_{\mathcal{L}} \rightarrow Q_{\mathcal{L}}A_{\mathcal{L}} \rightarrow A_{\mathcal{L}}P_{\mathcal{L}} \rightarrow P_{\mathcal{L}}R_n$, is the path of the EM wave which creeps over the left side of the torso for a distance $t_{\mathrm{TXQ}_{\mathcal{L}}}$, then leaves the torso tangentially at the point of leave $Q_{\mathcal{L}}$, travel in a free space for a distance s_{i}, gets reflected by the left arm at the point of reflection $A_{\mathcal{L}}$, travel in a free space for a distance s_{r} and then creeps to the receiver at R_n for a distance $t_{\mathrm{P}_{\mathcal{L}}\mathrm{RXn}}$ from the point of contact $P_{\mathcal{L}}$. The second path is a similar path,

$TQ_{\mathscr{R}} \to Q_{\mathscr{R}}A_{\mathscr{R}} \to A_{\mathscr{R}}P_{\mathscr{R}} \to P_{\mathscr{R}}R_n$ on the right side. The total electric field at the receiver is given by the sum of the electric field of the waves from the four paths: $\mathbf{E} = \mathbf{E}_c + \mathbf{E}_{ac} + \mathbf{E}_{TA_{\mathscr{L}}P_{\mathscr{L}}R_n} + \mathbf{E}_{TA_{\mathscr{R}}P_{\mathscr{R}}R_n}$. For the clockwise (subscript c) and the anti-clockwise (subscript ac) creeping waves, $\mathbf{E}_i = \mathbf{E}_{0i}e^{-L_i}$ where the subscript i can be c or ac. L_i can be calculated from (4) with proper values of φ for different receiver positions. The reference electric field $\mathbf{E}_{0i}$ at a distance z_i from the transmitting antenna on a conducting surface is given by [4]:

$$\mathbf{E}_{0i} = 2\sqrt{\frac{\eta_0}{2\pi}}\frac{\sqrt{P_{TX}G_{TX}}}{z_i}\mathrm{e}^{-jkz_i} \tag{5}$$

where η_0 is the wave-impedance in a free space and $z_i = p - d_\mathrm{n}$ for $i = c$ and $z_i = d_\mathrm{n}$ for $i = ac$. The received electric field for the reflected wave from the arm is modeled as $\mathbf{E}_{TA_{\mathscr{J}}P_{\mathscr{J}}R_n} = \mathbf{E}_{0\mathscr{J}}e^{-L_{\mathrm{TQ}_{\mathscr{J}}}}e^{-L_{\mathrm{P}_{\mathscr{J}}\mathrm{RXn}}}$ for $\mathscr{J} = \mathscr{L}$ or $\mathscr{R}$. $L_{\mathrm{TQ}_{\mathscr{J}}}$ is the attenuation factor from the Tx to the point of leave $Q_{\mathscr{J}}$ and $L_{\mathrm{P}_{\mathscr{J}}\mathrm{RXn}}$ is attenuation factor from the point of contact $\mathrm{P}_{\mathscr{J}}$ to the Rx. The reference electric field for the reflected wave is given by [13]:

$$\mathbf{E}_{0\mathscr{J}} = \rho\frac{1}{\sqrt{2}}\sqrt{\frac{\eta_0}{2\pi}}\frac{\sqrt{P_{TX}G_{TX}}}{z_{\mathscr{J}}}\mathrm{e}^{-jkz_{\mathscr{J}}} \tag{6}$$

where $z_{\mathscr{J}} = t_{\mathrm{TXQ}_{\mathscr{J}}} + s_{\mathrm{i}\mathscr{J}} + s_{\mathrm{r}\mathscr{J}} + t_{\mathrm{P}_{\mathscr{J}}\mathrm{RXn}}$ for $\mathscr{J} = \mathscr{L}$ or $\mathscr{R}$ and ρ is the reflection coefficient of the arm at an angle of incidence θ [14].

The received power is $P_{RX} = \frac{|\mathbf{E}|^2 A_{RX}}{2\eta_0}$ where $A_{RX} = G_{RX}\frac{\lambda^2}{4\pi}$ is the receive antenna aperture (G_{RX} is the gain of the antenna and λ is the wavelength in a free space). Substituting $\mathbf{E} = \mathbf{E}_c + \mathbf{E}_{ac} + \mathbf{E}_{TA_{\mathscr{L}}P_{\mathscr{L}}R_n} + \mathbf{E}_{TA_{\mathscr{R}}P_{\mathscr{R}}R_n}$ in the received power's expression, the link loss, $LL_n|_{\mathrm{dB}}$ at the n^{th} receiver position can be written as:

$$LL_n|_{\mathrm{dB}} = -10\log_{10}\left.\frac{P_{RX}}{P_{TX}}\right|_n \tag{7}$$

The detail equation of the link loss is shown in (8).

$$\begin{aligned} LL_n|_{\mathrm{dB}} \quad = \quad & -10\log_{10}\left[\frac{G_{RX}G_{TX}\lambda^2}{4\pi^2}\left(\left|\frac{e^{-L_{acn}}}{d_n}e^{-jkd_n} + \frac{e^{-L_{cn}}}{p-d_n}e^{-jk(p-d_n)}\right.\right.\right. \\ & + \sum_{\mathscr{J}=\mathscr{L}}^{\mathscr{R}}\frac{\rho}{2\sqrt{2}}\frac{e^{-L_{\mathrm{TQ}_{\mathscr{J}}}}e^{-L_{\mathrm{P}_{\mathscr{J}}\mathrm{RXn}}}\cos\gamma_{\mathscr{J}}}{t_{\mathrm{TXQ}_{\mathscr{J}}} + s_{\mathrm{i}\mathscr{J}} + s_{\mathrm{r}\mathscr{J}} + t_{\mathrm{P}_{\mathscr{J}}\mathrm{RXn}}} \\ & \left.\left.\left.\times e^{-jk(t_{\mathrm{TXQ}_{\mathscr{J}}} + s_{\mathrm{i}\mathscr{J}} + s_{\mathrm{r}\mathscr{J}} + t_{\mathrm{P}_{\mathscr{J}}\mathrm{RXn}})}\right|\right)^2\right] \end{aligned} \tag{8}$$

The positions of the receive antenna which lies between the point of leave, $\mathrm{Q}_{\mathcal{J}}$ and the point of contact $\mathrm{P}_{\mathcal{J}}$ for $\mathcal{J} = \mathcal{L}$ or $\mathcal{R}$, receives the reflected wave from the arm directly. These positions lies on the ellipse within the shaded portion between the arm and the ellipse shown in Fig. 1. However, if the direct received wave is in the direction of the null of the receive antenna, it will not contribute to the received power. This may be a case as the antennas for the on-body propagation are usually designed to minimize the power in the direction away from the body. To take care of such a case, a factor $\cos\gamma$ is multiplied to the received reflected field, where $\gamma = 0$ if R_n lies between $\mathrm{P}_{\mathcal{L}}$ and $\mathrm{P}_{\mathcal{R}}$, else it is equal to the angle between the tangent to the ellipse at the receiver position and the reflected wave. Similarly, if the transmit antenna is placed at a position where $|x_{\mathrm{TX}}| > |x_{\mathrm{CE}\mathcal{J}}|$ for $\mathcal{J} = \mathcal{L}$ or $\mathcal{R}$, the incident wave will be directly received by the arm.

3 Validation of the Analytical Model

The validation of the model is done over a truncated numerical phantom [10] with homogeneous electrical properties of muscle (permittivity = 52, conductivity = 1.7 S/m). The phantom has dimensions of a typical adult male with $a = 144$ mm, $b = 93.6$ mm and $r = 50$ mm. A truncated phantom is used as the whole body has a minimal influence on the link around the torso [10]. The validation is done through the full-wave electromagnetic simulations in SEMCAD-X which uses the FDTD method. If the validation is done through measurement, post processing on the measured data is required because of the effects like leakage current from the cable, ground reflections and change in the path-length due to respiration and body movements. Moreover, due to the finite size of the antenna the detection of fading dips is not possible [4]. Hence, full-wave simulation is chosen.

Six different scenarios are considered for the validation of the analytical model. In all these six scenarios, the receiver antenna is moved along the front side of the abdomen at 21 positions at a spacing of $x = a/10$. Additionally, few more positions are considered between these 21 positions to confirm the fading dips. These scenarios are shown in the inset of Fig. 2 which also shows the plots for the simulated and the analytical S_{21}. The link loss (LL) in (2.2) is the negative of S_{21} in dB. It could be seen that a good agreement between the simulations and the analytical model is obtained. Some differences might occur due to the fact that the torso is not completely elliptical in shape. Variations in the antenna gain at different positions may also contribute to these differences [5]. The antenna used as the receiver and the transmitter is a small monopole antenna matched in 2.45 GHz ISM band [2] which is vertically po-

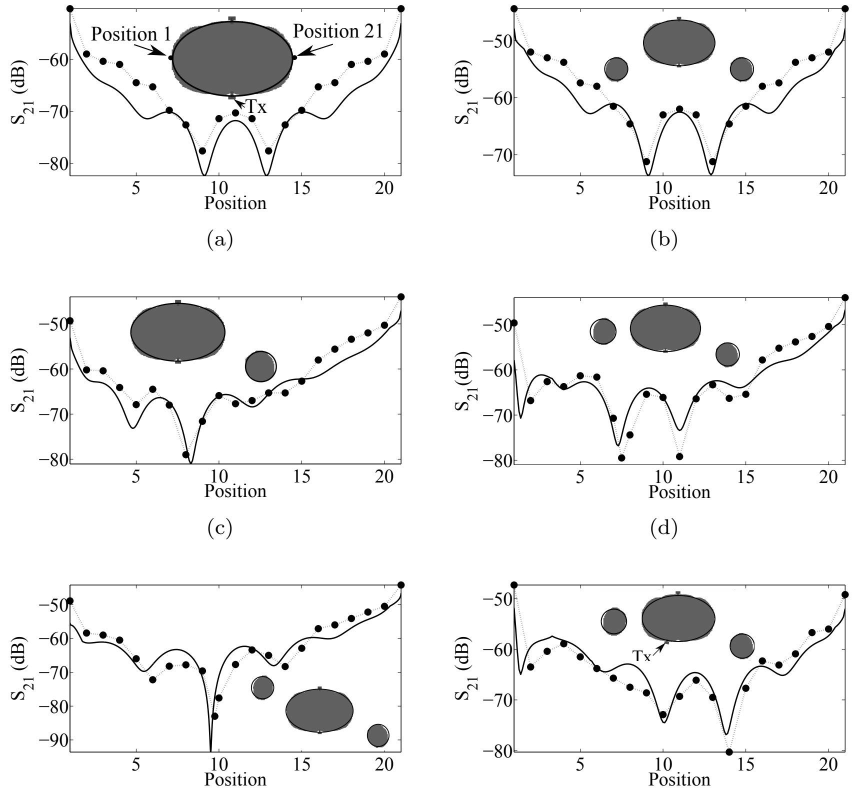

(a) (b)

(c) (d)

(e) (f)

Figure 2: Simulated S_{21} (dotted line) versus Analytical S_{21} (solid line). Arms are not included in (a). In (a)-(e), the transmit antenna is at the central back position whereas in (f) the transmit antenna is shifted from the central back position towards left by 43 mm.

larized (w.r.t. the body). The value of the gain used in the analytical equation is −7.3 dBi which is the gain of the antenna in the direction of the creeping wave at the central abdomen position. More discussion about the usage of the gain of the on-body antenna for the creeping wave can be found in [4], [5].

4 Evaluation of the Arms' Effect

It is critical to include the effect of the arms while estimating the link loss because the reflected waves from the arms at a intended receiver position might interfere destructively with the on-body creeping waves. Hence, the link loss at that receiver position will be higher than the link loss obtained without considering the effect of the arms. For example, let us consider a case when the receiver is placed midway between position 9 and position 10. The link loss is about 78 dB without considering the effects of the arms (Fig. 2(a)) whereas it is about 94 dB for the same receiver position with the arms as in Fig. 2(e). Hence, the signal reception at this position will be poor if the receiver is designed to handle 80 dB of the link loss considering the loss without the arms.

Let us consider another example of the usage of the model at 2.45 GHz for a case when $a = 140$ mm, $b = 93.5$ mm and $r = 40$ mm. The transmitter is fixed at the central back position and −7.3 dBi is used as the antenna gain. The x-coordinate of the center of the left arm is kept fixed at $-(a+2r)$ and at $(a+2r)$ for the right arm. The y-coordinate of the left arm is moved from $-1.5b$ to $1.5b$ and $1.5b$ to $-1.5b$ for the right arm, at an interval of $0.05b$, simultaneously. The position where y-coordinate of the left arm is $-1.5b$ and that of the right arm is $1.5b$, is called arm position 1 and so on. Fig. 3, shows the variation of S_{21} at the different receiver positions for different arm positions calculated using (2.2). The worst case link loss for this case is about 98 dB whereas it is 81 dB without considering the reflections from the arms. Hence, it is important to consider the link loss with the arms for a reliable link.

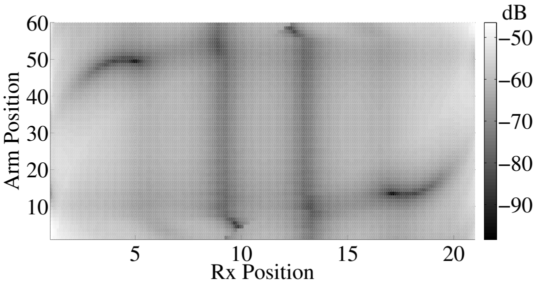

Figure 3: Variation of S_{21} at different Rx positions for different arm positions

5 Usage of the Model in Practice

To calculate the link loss in a practical setting, a, b and r have to be measured. The measured waist-to-waist value will be approximately equal to $2a$ and the measured abdomen-to-back to $2b$. r could be calculated by measuring the perimeter of the arm and equating it with the perimeter of a circle with radius r. Once these values have been measured, $(1)-(6)$ can be used to calculate other parameters as discussed in Section II. On-body antenna gain can be calculated by the method discussed in [4]. Finally, the link loss at any receiver position can be calculated using (2.2) for different arms' and transmitter positions. With the obtained values of the link loss, positioning of the receiver or the worst case link loss that the receiver could handle can be decided for a reliable link.

6 Conclusions

An analytical model for the link loss around the torso which includes the effects of the arms was presented. The model was validated through the full-wave simulations. It was shown that the reflection of the waves from the arms at some receiver positions around the torso resulted in a higher link loss than for a case without the arms. Hence, the effects of the arms have to be considered for a proper estimation of the link loss for a reliable link between the WBAN devices placed around the torso. The input parameters needed for the model are the dimensions of the human torso and the arms. These can be obtained by measurement on the user and the link loss can be estimated for different receiver positions around the torso for any position of the arms and the transmitter.

References

[1] Benoît Latré, and et. al., "A survey on wireless body area networks," *Wireless Netw.*, vol. 1, Issue 17, pp. 1-18, Jan. 2011

[2] R. Chandra, and A. J Johansson, "Miniaturized antennas for link between binaural hearing aids," in *Proc. Annual Int. Conf. IEEE Engg. in Med. Bio. Soc.*, pp. 688-691, Sept. 2010

[3] J. Ryckaert, P. De Doncker, R. Meys; A. de Le Hoye, and S. Donnay, "Channel model for wireless communication around human body," *Electronics Lett.*, vol. 40, no. 9, pp. 543- 544, April 2004

[4] T. Alves, B. Poussot, and J.-M. Laheurte, “Analytical Propagation Modeling of BAN Channels Based on the Creeping-Wave Theory,” *IEEE Trans. Antennas Propagat.*, vol. 59, no. 4, pp. 1269-1274, April 2011

[5] R. Chandra, and A. J Johansson, “An elliptical analytic link loss model for wireless propagation around the human torso,” *Proc. of the sixth European Conf. Antennas Propag.*, pp.3121-3124, March 2012

[6] A. Fort, F. Keshmiri, G.R. Crusats, C. Craeye, and C. Oestges, “A Body Area Propagation Model Derived From Fundamental Principles: Analytical Analysis and Comparison With Measurements,” *IEEE Trans. Antennas Propagat.*, vol. 58, no. 2, pp. 503-514, Feb. 2010

[7] G. Roqueta, A. Fort; C. Craeye, and C. Oestges, “Analytical Propagation Models for Body Area Networks,” in *Proc. IET Seminar Antennas Propagat. for Body-Centric Wireless Commun.*, pp. 90-96, April 2007

[8] S.L. Cotton, G.A. Conway and W.G. Scanlon, “A Time-Domain Approach to the Analysis and Modeling of On-Body Propagation Characteristics Using Synchronized Measurements at 2.45 GHz,” *IEEE Trans. Antennas Propagat.*, vol. 57, no. 4, pp. 943-955, April 2009

[9] Ahmed M. Eid and Jon W. Wallace, “Accurate Modeling of Body Area Network Channels Using Surface-Based Method of Moments,” *IEEE Trans. Antennas Propagat.*, pp. 3022-3030, Vol. 59, No.8, Aug. 2011

[10] R. Chandra, and A. J Johansson, “Effect of Frequency, Body Parts and Surrounding on the On-Body Propagation Channel Around the Torso,” *Proc. Annual Int. Conf. IEEE Engg. in Med. Bio. Soc.*, pp. 4533-4536, Sept. 2012

[11] [Online]. Available: http://www.speag.com/products/semcad/solutions/

[12] C. Balanis, and L. Peters, Jr., “Aperture radiation from an axially slotted elliptical conducting cylinder using geometrical theory of diffraction,” *IEEE Trans. Antennas Propag.*, vol. 17, no. 4, pp. 507-513, Jul. 1969

[13] David A. Hill, *The Measurement, Instrumentation and Sensors Handbook*, CRC Press, Chapter 47, 1999

[14] A.F. Molisch, *Wireless Communications*, West Sussex, England, Wiley, 2007

Paper IV

An Approach to Analyze the Movements of the Arms while Walking using Wearable Wireless Devices

Rhythmic movement of the arms while walking is an important feature of human gait. In this paper, we present an approach to analyze the movements of the arms while walking by using three wearable wireless devices placed around the torso. One of the devices is transmitter placed at the back and the other two are symmetrically placed receivers that record the power variation due to movements of the arms while walking. We show that the power received by the receivers will have symmetrical variation if the arms' swing is symmetrical. An analytical model has been used to calculate the position of the receivers. Full wave simulations on a walking phantom are done to confirm the results.

R. Chandra, and A. J Johansson
"An approach to analyze the movements of the arms while walking using wearable wireless devices," in *Proc. 35th Ann. Int. Conf. IEEE Engg. Med. Bio. Soc.*, EMBC, pp. 3431-3434, Jul. 2013

1 Introduction

Wearable wireless medical devices or sensors have improved the healthcare facilities. They are used for the monitoring of vital health parameters like temperature, blood pressure, glucose level and for ambulatory monitoring [1]. One of the benefits of the wearable medical devices is that they are non-invasive and hence have minimal risk of infection. Wearable devices have been developed for recording human kinematics and posture by using sensing fabrics [2]. Monitoring of human kinematics and analyzing posture is of importance in the field of bioengineering. It is also beneficial in the field of sports biomechanics for improvements in athlete performance. Moreover, they are used for recovery and rehabilitation of people with injuries having movement related problems.

The pattern of movements of the arms, legs and trunk during activities like walking is called gait. Gait is an important health indicator and has been widely studied for treating patients with walking disability arising due to injuries, neurological disorders like Parkinson's disease [3], [4]. Moreover, it can be used for fall prediction and prevention [5]. Arm swing during human gait is an important component for locomotion enhancing gait stability and decreasing the metabolic cost of walking [6]. There is a rhythmic symmetric swing of the arms while walking and a high asymmetry in the arms' swing can be an early sign for Parkinson's disease [7], [8]. In [7], authors have used motion analysis with ultrasound based recordings of limb kinematics for measuring and analyzing the arms' swing. In [8], accelerometer assemblies are affixed to the right and left forearms of each subject to detect the arms' movements. In this paper, we have used a system of three wearable wireless sensors around the torso to observe the movements of the arms while walking. Such a system could be on a belt worn around the waist and hence is different from the previous research where the sensors are placed on the arms. Moreover, the sensors used in this paper are radio-frequency sensors, unlike the previous research where they are inertial or ultrasound sensors. We have shown in [9], that there is a variation in the power received by the wireless sensors placed around the torso from a transmitting sensor at the back, with the variation in the arms' position. This is due to the difference in the reflected power from the arms when they are at different positions. Further, in [10], an analytical model considering the effect of the arms, for signal propagation around the torso is developed. This model has been used to calculate the positions of the receiver sensors when the arms' swing while walking. Simulations have been done on a numerical phantom with different snapshots of one gait cycle to observe the pattern of the power variation recorded by the receivers.

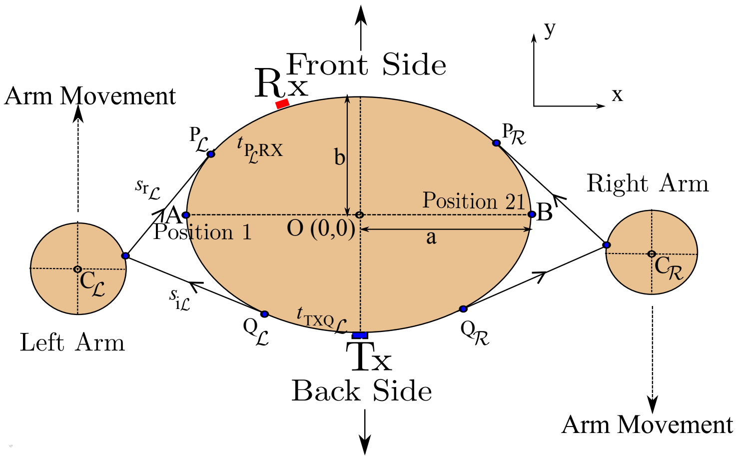

Figure 1: Cross-sectional view of the torso at the level of the antennas. Different path-lengths are also shown.

$$LL_n|_{\text{dB}} = -10\log_{10}\left[\frac{G_{RX}G_{TX}\lambda^2}{4\pi^2}\left(\left|\frac{e^{-L_{acn}}}{d_n}e^{-jkd_n} + \frac{e^{-L_{cn}}}{p-d_n}e^{-jk(p-d_n)} + \sum_{\jmath=\mathcal{L}}^{\mathcal{R}}\frac{\rho}{2\sqrt{2}}\frac{e^{-L_{\text{TQ}_\jmath}}e^{-L_{\text{P}_\jmath\text{RXn}}}\cos\gamma_\jmath}{t_{\text{TXQ}_\jmath}+s_{\text{i}\jmath}+s_{\text{r}\jmath}+t_{\text{P}_\jmath\text{RXn}}} \times e^{-jk(t_{\text{TXQ}_\jmath}+s_{\text{i}\jmath}+s_{\text{r}\jmath}+t_{\text{P}_\jmath\text{RXn}})}\right|\right)^2\right] \quad (1)$$

2 Wave Propagation Around the Torso in Presence of the Arms

In [11], an analytical model for propagation around the torso without considering the effect of the arms was presented. The model was based on the attenuation of creeping waves over an elliptical approximation of the torso. In [10], the model was extended to include the reflections from the arms. The reflected waves from the arms adds up at the receiver with the clockwise and the anti-clockwise creeping waves constructively or destructively depending upon the position of the receiver and the position of the arms. The link loss at the n^{th} position of the receiver (Rx), in the presence of the arms can be modeled as (1) [10], shown at the bottom of the next page. In (1), G is the gain of the antenna for receiver or the transmitter (Tx) denoted by the subscript RX or TX respectively. λ is the wavelength in a free space. L is the complex attenuation over the elliptical path with subscript ac for the anti-clockwise creeping wave path, c for the clockwise creeping wave path, TQ for the path between the transmitter and the point of leave Q and PRX_n for the path between the point of contact P of the reflected wave and the receiver. These paths and other path lengths in (1) are shown in Fig. 1. p is the perimeter of the elliptical fit of the torso and d_n is the length of the anti-clockwise path from the transmitter to the receiver at the n^{th} position. $\mathscr{L}$ is used for the left side of the body and $\mathscr{R}$ for the right side. ρ is the reflection coefficient of the arm. The transmitter is fixed at the central back position. The receiver is moved from position 1 (point A) to position 21 (point B). The on-body antenna working in 2.45 GHz ISM band, described in [12] is used at the transmitter and the two receivers. While walking, the arms will swing back and forth. It is assumed that the arms' centers remain at a fixed distance from the origin along the x-axis. We call this distance x_0. One cycle of the arms' movement during walk is divided into 25 arm positions. The first position is when the left arm's center, $C_{\mathscr{L}} = (-x_0, -2b)$ and right arm's center, $C_{\mathscr{R}} = (x_0, 2b)$ whereas at the 25^{th} position, $C_{\mathscr{L}} = (-x_0, 2b)$ and right arm's center, $C_{\mathscr{R}} = (x_0, -2b)$. Fig. 2 shows S_{21} variation, where $S_{21}|_{dB} = -LL|_{dB}$, for one cycle of the arm swing over all the receiver positions calculated using (1) for $x_0 = a + 2r$ (r is the radius of the arms). A typical human dimension with $a = 144$ mm, $b = 94$ mm and $r = 45$ mm is considered. It should be noted here that while plotting the variation of S_{21} using (1), for simplicity, it is assumed that if right arm moves a step, the left arm moves the same step in reverse direction. However, (1), can be used to plot the variation for other cases when the arm movement is random by using proper values of the parameters.

2.1 Position of the receiver

From Fig. 2 it could be seen that as the arms move, at some receiver positions, there is a large variation of S_{21} whereas at some positions, the variation is not so significant. Additionally, a symmetrical power variation with respect to the position 13, when both the arms are at side of the torso, can be observed from the figure. We propose to place one receiver for each arm at the position where there is a significant influence of the arms' movements. These positions could be found by taking the variance of the difference of S_{21} at each successive arm position for all the receiver positions. The variance at different receiver positions is shown in Fig. 3. The receivers should be placed at the positions where the variance is high. The maximum peak of the variance is around position 3 and position 19. However, we place the receivers at position 1 (for

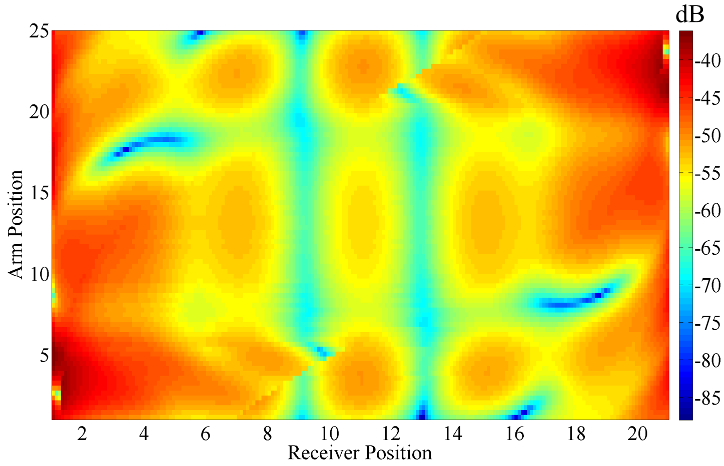

Figure 2: S_{21} (dB) for different receiver position and one cycle of the arm swing

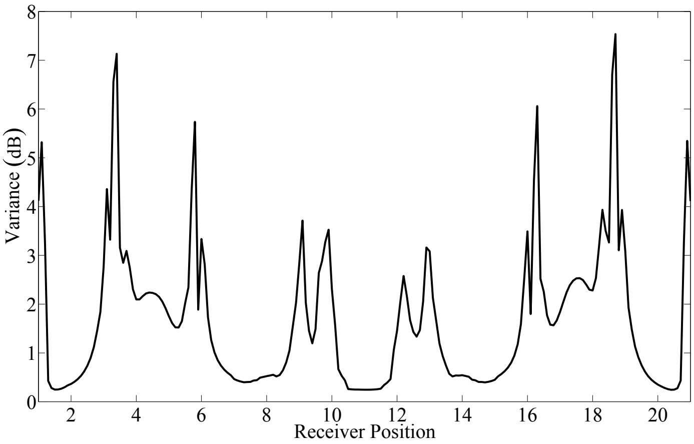

Figure 3: Variance of the difference of S_{21} in dB at successive arm position for different receiver position in one cycle of the arm swing

the left arm) and position 21 (for the right arm) as the variance is still high at these positions and they are easily identifiable on the phantom.

3 Simulations

The simulations have been done on a numerical phantom of an adult human size (height 171 cm) created in a 3D animation software POSER [13] in a commercial full wave simulator SEMCAD-X [14] which uses the FDTD method. The phantom is animated to walk and different frame of the one gait cycle is saved as a separate file and then imported to SEMCAD-X. There is asymmetry in the arms' movement of the phantom. The elliptical fit for the torso of the phantom gave $a = 144$ mm, $b = 94$ mm, $r = 45$ mm approximately. These values change slightly while walking. The electrical properties of human muscle at 2.45 GHz (permittivity = 52 and conductivity = 1.7 S/m) is assigned to the phantom. As mentioned in Section II, the on-body antenna working at 2.45 GHz ISM band, described in [12] is used at the transmitter and the two receivers. The transmitter is kept fixed at the back of the phantom and two receivers, one on the left side of the torso and other on the right side is placed to record the variation in S_{21} between the transmitter and the two receivers when the arms move while walking. The phantom with different arm positions for one gait cycle is shown in Fig. 4.

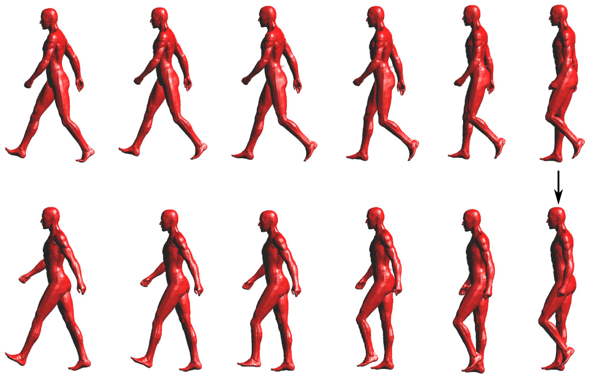

Figure 4: Arm movement in one gait cycle

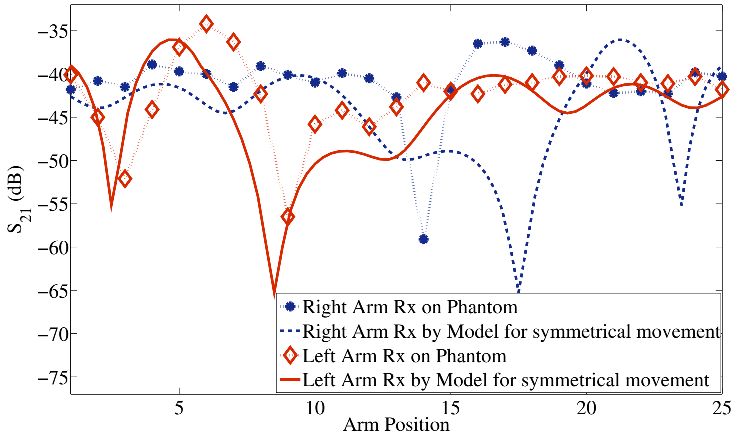

Figure 5: S_{21} between the transmitter and each of the receiver for the analysis of the arm movement

4 Results and Discussions

The S_{21} between the transmitter and the receiver for the left arm and the receiver for the right arm is shown in Fig. 5. It can be seen that the plots for the receivers are not symmetrical as the movements of the arms of the phantom are not symmetrical. It should be noted that the symmetry here is w.r.t. the position when both the arms are exactly at the side of the torso (position 13). Additionally, there is about 22 dB difference between the maximum and the minimum S_{21} for each arm which can be easily detected by the receivers. The figure also shows the plot for the case for a perfect symmetrical swing of the arms estimated by (1). An agreement between the simulated S_{21} for the left arm and S_{21} predicted by (1) can be seen. A difference can be seen for the right arm case as the swing was not symmetrical.

5 Conclusions

An approach to analyze the arms' movements while walking by using three wearable devices attached on the torso was presented. An analytical model was used to determine the placement positions of the devices. The transmitter was placed at the central back position and the two receivers, one for each arm, was placed at the side of the torso. It was found that the rhythmic symmetric movement of the arms while walking will cause symmetrical variation in the received power by the two receivers whereas asymmetry in the arms' movements will result in asymmetrical power variation. The result was confirmed by the simulations done on a walking phantom with asymmetrical arms' swing. Hence, such a wearable system might be a simple solution for the analysis of the movements of the arms. It could comprise of a belt with three 2.45 ISM band transceivers that also record the RSSI and could be worn around the waist. It could be used for detecting asymmetry in the arms' swing while walking.

Future work will consist of doing simulations on walking phantom with different arm movements. The influence in the power variation due to the sensitivity in positioning of the receivers will be investigated in order to find robust placement positions. Measurements on humans subjects will also be done.

References

[1] A. Dittmar, R. Meffre, F. De Oliveira, C. Gehin, and G. Delhomme, "Wearable Medical Devices Using Textile and Flexible Technologies for Ambulatory Monitoring," in *Proc. 27th Annual Int. Conf. Engg. in Med. and Bio. Soc.*, IEEE-EMBS 2005, pp. 7161-7164, 2005

[2] D. De Rossi, F. Lorussi, A. Mazzoldi, P. Orsini, and E.P. Scilingo, "Monitoring body kinematics and gesture through sensing fabrics," in *Proc. 1st Annual Int. Conf. on Microtech. Med. and Bio.*, pp. 587-592, 2000

[3] J. D. O'Sullivan, C. M. Said, L.C. Dillon, M. Hoffman and A. J. Hughes, "Gait analysis in patients with Parkinson's disease and motor fluctuations: Influence of levodopa and comparison with other measures of motor function," *Mov. Disord.*, vol. 13, Issue 6, pp. 900-906, 1998

[4] O. Sofuwa, A. Nieuwboer, K. Desloovere, Anne-Marie Willems, F. Chavret, and I. Jonkers, "Quantitative Gait Analysis in Parkinson's Disease: Comparison With a Healthy Control Group," *Archives of Physical Medicine and Rehabilitation*, vol. 86, Issue 5, pp. 1007-1013, May 2005

[5] S. Jiang, B. Zhang, and D. Wei, "The Elderly Fall Risk Assessment and Prediction Based on Gait Analysis," in *Proc. IEEE 11th Int. Conf. Comp. Info. Tech.*, pp. 176-180, Sept. 2011

[6] S. M. Bruijn, O. G. Meijer, P. J. Beek, and J. H. van Dieen, "The effects of arm swing on human gait stability," *The Jour. Exp. Biology*, pp. 3945-3952, Dec. 2010

[7] J. Roggendorf, S. Chen, S. Baudrexel, S. van de Loo, C. Seifried, and R. Hilker, "Arm swing asymmetry in Parkinson's disease measured with ultrasound based motion analysis during treadmill gait," *Gait & Posture*, Vol. 35, Issue 1, pp. 116-120, Jan. 2012

[8] X. Huang, J. M. Mahoney, M. M. Lewis, G. Du, S. J. Piazza, J. P. Cusumano, "Both coordination and symmetry of arm swing are reduced in Parkinson's disease", *Gait & Posture*, Vol. 35, Issue 3, pp. 373-377, March 2012

[9] R. Chandra, A. J Johansson, "Effect of Frequency, Body Parts and Surrounding on the On-Body Propagation Channel Around the Torso," *Proc. Annual Int. Conf. IEEE Engg. in Med. Bio. Soc.*, pp. 4533-4536, Sept. 2012

[10] R. Chandra, and A. J Johansson, "An Analytical Link Loss Model for On-Body Propagation Around the Body Based on Elliptical Approximation of the Torso with Arms' Influence Included," *IEEE Antennas Wireless Propagat. Lett.*, pp. 528 - 531, 2013

[11] R. Chandra and A. J Johansson, "An elliptical analytic link loss model for wireless propagation around the human torso," in *Proc. 6th European Conf. Antennas Propagat., EUCAP*, pp. 3121-3124, Mar. 2012

[12] G.A. Conway, and W.G. Scanlon, "Antennas for Over-Body-Surface Communication at 2.45 GHz", *IEEE Trans. Antennas Propagat.*, Vol. 4, Issue 4, Part 1, pp. 844-855, Apr. 2009

[13] POSER, Curious Labs Inc. 655 Capitola Road, Suite. 200, Santa Cruz, CA 95062

[14] [Online]. Available: http://www.speag.com/products/semcad/solutions/

Paper V

A Microwave Imaging based Technique to Localize an In-body RF-Source for Biomedical Applications

In some biomedical applications such as wireless capsule endoscopy, the localization of an in-body RF-source is important for the positioning of any abnormality inside the gastro-intestinal tract. With knowledge of the location, therapeutic operations can be performed precisely at the position of the abnormality. Electrical properties (relative permittivity and conductivity) of the tissues and their distribution are needed to estimate the position. This paper presents a method for the localization of an in-body RF-source based on microwave imaging. The electrical properties of the tissues and their distribution at 403.5 MHz are found from microwave imaging and the position of an RF-source is then estimated based on the image. The method is applied on synthetic noisy data, obtained after the addition of white Gaussian noise to simulated data of a simple circular phantom, and a realistic phantom in a two dimensional case. The root-mean-square of the error distance between the actual and the estimated position is found to be within 10 mm and 4 mm for the circular and the realistic phantom respectively, showing the capability of the proposed algorithm to work with a good accuracy even in the presence of noise for the localization of the in-body RF-source.

R. Chandra, A. J Johansson, M. Gustafsson, and F. Tufvesson
"A Microwave Imaging based Technique to Localize an In-body RF-Source for Biomedical Applications," Submitted to *IEEE Trans. Biomed. Engg.*, 2014

1 Introduction

Today there is an increased use of wireless technology for medical diagnosis that is supported by miniaturization of the application specific integrated circuits (ASICs). The technology has led to improved diagnostic tools especially for inspecting diseases inside the human body. Wireless capsule endoscopy is an example of such a medical diagnostic tool which has evolved from the wireless technology and miniaturization of the ASICs.

Endoscopy is a medical procedure used to examine and inspect the interior of the body, e.g. diagnosing gastrointestinal (GI) tract diseases. In conventional endoscopy, a long flexible fiber tube is inserted through the mouth or the rectum to transmit light to illuminate the organ under inspection to view it through a lens system. However, this procedure may cause pain and discomfort due to relatively large diameter of the fiber tube. Furthermore, sedation may be required for the entire period of the endoscopy. Moreover, this method of the endoscopy is incapable of reaching the entire small intestine due to its complex anatomy [1]. These limitations of conventional endoscopy can be overcome by the use of wireless capsule endoscopy (WCE) [1], [2]. A wireless capsule endoscope is a swallowable pill-like wireless device containing an electronic circuitry with a radio-frequency (RF) transmitter, light emitting diodes for illumination, and a miniature camera which captures images while it passes through the GI tract. The images are sent through the body tissues to external sensor antennas located on the body. The sensor data is stored in an external device for off-line analysis.

Once the images are analyzed and the abnormality or any disease is detected, therapeutic operations may be performed at the location of the abnormality which can be identified from the location of the captured image. However, due to the complex tissue environment of the human body in which the capsule is moving, accurate localization is a challenging task. The methods used for the localization of the capsule are usually based on measurements of low frequency magnetic fields or electromagnetic (EM) waves as reviewed in [1]. Both methods have their advantages and challenges. One of the advantages of the localization methods based on the low-frequency magnetic field strength is that the magnetic signal can pass through the body with low attenuation as the tissues are non-magnetic. Challenges include interference from the earth's magnetic field and the magnetic field produced by the magnetic material present in the surrounding. These may require additional equipment for analysis of the magnetic signal for the localization. On the other hand, systems based on EM waves can reuse the EM signal radiated by the capsule without any additional equipment. However, a trade-off has to be made in choosing the right frequency of EM signals as high frequency EM signals, which have high precision of localization, also have higher attenuation than the low frequency EM signals having a low precision of localization.

One of the frequency bands that can be used for capsule localization is the 403.5 MHz MedRadio band. The reason for using the 403.5 MHz MedRadio is that it has relatively low attenuation of the EM waves through the human tissue. However, the bandwidth of 5 MHz assigned to the MedRadio band is not sufficient for resolving the multipath components, occurring due to reflections from the several layers of the tissues. Hence, time based localization methods like time of arrival and time difference of arrival are hard to use. These methods may be used with ultra-wideband due to the large bandwidth [3]. Additionally, methods based on angle of arrival (AoA) is also challenging due to the presence of multipath components. Hence, methods which have been used so far in low frequency are generally based on the received signal strength (RSS) [4]-[15]. Typically, the first step in the RSS based methods is to estimate the distance of the capsule from the receive antennas located on the abdomen [6], [7]. A signal propagation model is used, which relates the RSS with the distance between the in-body RF-source and the receive antennas. After these distances are known, trilateration is employed to calculate the coordinates of the capsule. However, the RSS methods suffer from poor localization accuracy and needs a propagation model that varies from person to person due to the complex radio wave absorption properties of the human tissue. In [8], instead of using the propagation model, Shah et. al. presented an algorithm based on a look-up table where the offline measurements are carried for different positions of the capsule inside a phantom and stored in the look-up table. Later on during the experiment, the RSS is compared with the closest value in the look-up table for the position estimation. This method is specific to the phantom used and thus may not give good accuracy in a practical human measurement scenario.

In [16], we presented a localization method for WCE based on the phase difference of the signal received at different frequencies at the same receive antenna, and a non-linear least square iterative estimation method. A localization error, within 1 cm, was obtained for the noise-free simulated data of different homogeneous and heterogeneous phantoms. The method is suitable for the localization in a case of high signal-to-noise ratio (SNR) but is sensitive to noise. As the method is based on the phase difference at different frequencies, the presence of noise might affect the phase of the received signal, decreasing the accuracy. Moreover, another limitation as pointed out in the paper is that it assumes homogeneous electrical properties of the body in the localization algorithm. For a better localization, the electrical properties of the tissues are required. Furthermore, the distribution of tissues varies from person to person, and different organs of the GI tract have different electrical properties. In general, most of localization algorithms assume that the electrical properties of the body are available which, e.g., can be obtained through magnetic resonance imaging (MRI) as discussed in [15]. However, MRI is not a cost effective method and may be costlier than the WCE. Another method is computed tomography (CT) which is also costly and uses x-rays which are ionizing.

A low risk and a cost efficient solution to image the body is microwave imaging or tomography. Microwave imaging involves solving inverse electromagnetic problems to find the electrical properties of the object of interest by using the scattered electric field data. Microwave imaging of the biological bodies is well studied [17]-[22]. An iterative numerical method for microwave imaging is developed and studied for objects having electrical properties close to that of bone, muscle, and fat in [17]. In [18], an algorithm for microwave imaging is developed and implemented on a numerical human thorax and on measurement data of a human arm at 434 MHz. An iterative microwave imaging algorithm is demonstrated on experimental data of a human arm collected by a 2.33 GHz circular microwave imaging scanner using the two-dimensional (2D) transverse magnetic (TM) polarization. The feasibility of using microwave tomography for whole body imaging is shown in [20] by doing measurements on a dog. A biomedical imaging algorithm is demonstrated on experimental data of a human forearm, and synthetic data of brain and breast models for the 2D-TM polarization in [21]. A pilot study to image the human forearms by collecting scattering data at 0.8 GHz to 1.2 GHz of several person is presented in [22]. These presented research efforts demonstrate the capability of microwave imaging to estimate the electrical properties of the body.

In this paper, we use microwave imaging to estimate the electrical properties (relative permittivity and conductivity) and the distribution of the tissues inside a body at 403.5 MHz using external receive antennas placed close to the body or on-body both as receivers and transmitters in an alternating manner. Once the image of the body is obtained in this calibration step, *a priori* information about the electrical properties of the body and/or the body anatomy is used to find all the possible positions for the in-body RF-source and the signal is recorded from these possible positions by the on-body antennas. After calibration, the root-mean-square-error (RMSE) between these recorded signals and the signal obtained from the in-body RF-source from an unknown location during the measurement is calculated. The position of the RF-source having the minimum RMSE is the estimated position. The algorithm is applied on synthetic data obtained from finite-difference-time-domain (FDTD) simulations of a simple phantom and a realistic phantom where noise has been added to the simulated data.

It should be noted that the objective of using microwave imaging in the algorithm is not to obtain a detailed image of the body but to obtain a rough image with good enough information which could be used in the above described calibration process. The main contributions of the paper are: (a) development of an algorithm using EM waves at 403.5 MHz for the localization of an in-body RF-source (b) using cost-effective microwave imaging in the algorithm for localization and tracking of in-body RF-sources as in WCE which is demonstrated for the first time (to best of our knowledge) and (c) implementing the algorithm on FDTD simulated data of heterogeneous phantoms in the presence of white Gaussian noise in two dimensional cases with a localization error within 10 mm.

The paper is organized as following. Section 2 discusses the three step localization algorithm. The formulation of the microwave imaging problem is re-introduced in Section 2.1. Section 2.2 discusses the solution to the inverse microwave imaging problem. The implementation of the algorithm on the data obtained from the simulation of the numerical phantoms is described in Section 3. The localization results are presented in Section 2. Finally, Section 5 concludes the paper.

2 Localization Algorithm

The localization algorithm is a three step process consisting of: (1) microwave imaging, (2) calculation of the electric field from possible locations inside the imaged body, and (3) measurement and localization. These are described below.

1) *Microwave Imaging* : In the first step, which can be seen as a calibration step, the body is imaged using a microwave imaging technique which is discussed in the subsequent sections. The purpose of microwave imaging is to find a rough image of the internal body which gives an estimate of how different tissues with different electrical properties are distributed.

2.1 Formulation of Microwave Imaging

In this section, a microwave imaging technique based on the Levenberg-Marquardt method developed in [23] is outlined for completeness. Let us consider a case where there are M antennas placed around an inhomogeneous body that is to be imaged. The complete system (antennas and the body to be imaged) is inside a homogeneous medium which acts as a matching medium to reduce the reflections and also as an absorber by reducing the on-body creeping waves. Each antenna transmits one at a time and the electric field is recorded by the other $M-1$ antennas. Let $\mathbf{r}=(x,y)$ denote the coordinates of a spatial point in a 2D plane. For the coordinates $\mathbf{r}'$ of any spatial point in the imaging domain, a contrast function is defined as:

$$s(\mathbf{r}') = \omega^2 \mu_0 \varepsilon(\mathbf{r}') - \omega^2 \mu_0 \varepsilon_{ext}, \tag{1}$$

which is the difference between the squared wave number at a spatial point $\mathbf{r}'$ and the exterior medium. In (1), ε_{ext} is the complex permittivity of the external medium and $\varepsilon(\mathbf{r}')$ is the complex permittivity at $\mathbf{r}'$ given by

$$\varepsilon(\mathbf{r}') = \varepsilon_0 \left(\varepsilon_r(\mathbf{r}') - \mathrm{j} \frac{\sigma_e(\mathbf{r}')}{\omega \varepsilon_0} \right), \tag{2}$$

where $\varepsilon_r(\mathbf{r}')$ is the relative permittivity, $\sigma_e(\mathbf{r}')$ is the conductivity at a position coordinates $\mathbf{r}'$, ε_0 is the permittivity of free space, and ω is the angular frequency.

In the following description, index $t = 1, 2, 3, ..., M$ represents a snapshot when the t^{th} antenna is transmitting and others are receiving. The number of receive antennas per view is $M - 1$. The total electric field in the imaging domain satisfies the following integral equation [23]:

$$e_t(\mathbf{r}) = e_t^i(\mathbf{r}) + \iint_{body} s(\mathbf{r}') e_t(\mathbf{r}') G(\mathbf{r}, \mathbf{r}') d\mathbf{r}', \tag{3}$$

where G is the 2D Green's function for the TM polarization given by $G(\mathbf{r}, \mathbf{r}') = (\mathrm{j}/4) H_0^{(2)}(k_{ext}|\mathbf{r} - \mathbf{r}'|)$ and e_t^i is the incident field. $H_0^{(2)}$ is the Hankel function of zeroth order and second kind and k_{ext} is the wavenumber in the exterior medium. The scattered field on the receive antennas with position coordinates $\mathbf{r}_{\mathrm{rx}_n}$ with $n = 1, 2, ..., M - 1$ is given by

$$e_t^{scatt}(\mathbf{r}_{\mathrm{rx}_n}) = \iint_{body} s(\mathbf{r}') e_t(\mathbf{r}') G(\mathbf{r}_{\mathrm{rx}_n}, \mathbf{r}') d\mathbf{r}'. \tag{4}$$

Equations (3) and (4) define a forward scattering problem when the contrast s of the body and e_t^i are known quantities. The inverse scattering problem consists of solving the unknown contrast s for a set of scattered field measurement, which is a complex problem as it involves solving non-linear and ill-posed equations. For practical purposes, the area under investigation is discretized into N cells where the contrast is assumed to be constant within the cell. In matrix notation, the discretized form of (3) is written as [23]:

$$[\mathbf{I} - \mathbf{G}^r \mathbf{S}] \mathbf{e}_t = \mathbf{e}_t^i \tag{5}$$

and for the scattered field (4) on the receive antenna locations

$$\mathbf{e}_t^{scatt} = \mathbf{G}_t^{scatt} \mathbf{E}_t \mathbf{s}, \tag{6}$$

where $\mathbf{s} = [s_1, ...s_N]^T$ is a vector containing the contrast of N cells, $\mathbf{e}_t = [e_{t,1}, ..., e_{t,N}]^T$ is the vector of unknown total field in the N cells when the t^{th} transmit antenna is active, $\mathbf{e}_t^i = [e_{t,1}^i, ..., e_{t,N}^i]^T$ is the vector of incident field on N cells for the t^{th} transmit antenna, and $\mathbf{e}_t^{scatt} = [e_t^{scatt}(\mathbf{r}_{\mathrm{rx}_1}), ..., e_t^{scatt}(\mathbf{r}_{\mathrm{rx}_{M-1}})]^T$ is the receive field vector at the $M-1$ receive antennas for the t^{th} transmit antenna. $[.]^T$ denotes the transpose operation, $\mathbf{G}^r$ is $N \times N$ integrated Green's functions, and $\mathbf{G}_t^{scatt}$ is $(M-1) \times N$ integrated Green's functions. Integration of the Green's function is performed over a disk instead of a square as the analytical expression for the disk is available [24]. $\mathbf{S}$ and $\mathbf{E}_t$ are diagonal matrices with $[\mathbf{S}]_{jj} = s_j$ and $[\mathbf{E}_t]_{jj} = \mathbf{e}_{t,j}^i$ for $j = 1$ to N. As the electric field is used in the algorithm, in the rest of the paper *field* refers to the electric field.

2.2 Solution to the inverse problem

With the measured scattered field available, an estimate of the contrast $\hat{\mathbf{s}}$ for all the cells can be found by minimizing the error between the measured scattered field and the scattered field obtained from (6). In the least square sense it is:

$$\hat{\mathbf{s}} = \min_{\mathbf{s}} ||\mathbf{F}(\mathbf{s}) - \mathbf{e}^{scatt}||^2, \tag{7}$$

where $\mathbf{F}(\mathbf{s})$ is a complex non-linear vector function of the scattered field for contrast s and $\mathbf{e}^{scatt}$ is a vector formed by combining the measured vectors of the scattered field from all the transmit antennas. The error is minimized iteratively by finding the contrast for the next iteration from the current iteration k as discussed below:

$$\mathbf{D}^*\mathbf{D}\Delta\mathbf{s}_k = \mathbf{D}^*\Delta\mathbf{e}_k^{scatt}, \tag{8}$$

where $[.]^*$ denote conjugate transpose. $\mathbf{D}$ is the $M(M-1) \times N$ derivative matrix of $\mathbf{F}(\mathbf{s})$ with respect to $\mathbf{s}$ and is formed by gathering the $\mathbf{D}_t$ for each of the transmit antenna where $\mathbf{D}_t$ is given by

$$\mathbf{D}_t = \mathbf{G}_t^{scatt}[\mathbf{I} - \mathbf{S}\mathbf{G}^r]^{-1}\mathbf{E}_t. \tag{9}$$

Moreover, $\Delta\mathbf{s}_k = \mathbf{s}_{k+1} - \mathbf{s}_k$ and $\Delta\mathbf{e}_k^{scatt} = \mathbf{e}_k^{scatt} - \mathbf{F}(\mathbf{s})_k$ where $\Delta\mathbf{s}_k$ is used to denote the step length.

Equation (8) is ill-posed due to large condition number of the matrix $\mathbf{D}^*\mathbf{D}$ which needs to be inverted in order to find $\Delta\mathbf{s}_k$. Hence, the problem is regularized using Tikhonov regularization as [23]:

$$[\mathbf{D}^*\mathbf{D} + g_k\mathbf{I}]\Delta\mathbf{s}_k = \mathbf{D}^*\Delta\mathbf{e}_k^{scatt}. \tag{10}$$

The regularization enhances the convergence as the step length $\Delta\mathbf{s}_k$ shortens with an increase in g_k. Further, it controls the condition number of $\mathbf{D}^*\mathbf{D}$. The weight g_k is chosen empirically as [23]:

$$g_k = \alpha_k \frac{\mathrm{trace}[\mathbf{D}^*\mathbf{D}]}{N} \frac{||\mathbf{F}(\mathbf{s})_k - \mathbf{e}_k^{scatt}||^2}{||\mathbf{e}_k^{scatt}||^2}, \tag{11}$$

where the initial value of the weight α_k is empirically chosen. α_k is updated at each iteration depending upon the normalized field error $\mathcal{E}_k = (||\mathbf{F}(\mathbf{s})_k - \mathbf{e}_k^{scatt}||^2)/||\mathbf{e}_k^{scatt}||^2$ as [23]:

$$\begin{aligned} \alpha_{k+1} &= \alpha_k \text{ if } \mathcal{E}_k - \mathcal{E}_{k-1} < -0.1\mathcal{E}_k \\ \alpha_{k+1} &= \alpha_k/2 \text{ if } -0.1\mathcal{E}_k \leq \mathcal{E}_k - \mathcal{E}_{k-1} \leq 0.1\mathcal{E}_k \\ \alpha_{k+1} &= 2\alpha_k \text{ if } \mathcal{E}_k - \mathcal{E}_{k-1} > 0.1\mathcal{E}_k. \end{aligned} \tag{12}$$

The initial value of α_k influences the convergence speed. Further, at each step the contrast is checked such that $\varepsilon_{r_{min}} \leq \varepsilon_r(\mathbf{r}') \leq \varepsilon_{r_{max}}$ and $\sigma_{r_{min}} \leq \sigma_e(\mathbf{r}') \leq \sigma_{r_{max}}$, where $\varepsilon_{r_{min}}$ and $\varepsilon_{r_{max}}$ are the minimum and the maximum values of the relative permittivity of the tissues at the used frequency, respectively. Similarly, $\sigma_{r_{min}}$ and $\sigma_{r_{max}}$ are the minimum and the maximum values of the conductivity of the tissues. These values are known for the tissues of the body and used as *a priori* information. If the relative permittivity or the conductivity of any spatial position $\mathbf{r}'$ goes outside these bounds, they are overwritten with the maximum value if they are greater than the maximum value, or with the minimum value if they are below the minimum values. The iteration is stopped either if the minimum acceptable error is achieved or the difference between the errors of two iterations is below a threshold.

2) *Calculation of field from possible locations inside the imaged body*: Once the image of the body is obtained, in the second step, two types of *a priori* information can be used to find the possible positions of an RF-source depending upon the quality of the image. The first *a priori* information is the electrical properties of the tissues. For example, in the capsule endoscopy case, the capsule can only be in the gastro-intestinal tract (small intestine, large intestine, etc.) whose electrical properties are different from that of fat, bone or any other tissues. This *a priori* information can be used if the tissues are clearly distinguishable in the image. However, usually the presence of noise and low difference between the electrical properties of the certain tissues can make it difficult to distinguish them in the image. In such cases, *a priori* information of the human anatomy can be used. For example, at certain parts of the human body, a large proportion is occupied by muscle tissue and it might become difficult to distinguish between the muscle and the small intestine lumen having almost identical electrical properties. In such cases, the information about the human anatomy can be used to find the possible location of the small intestine

in the image. Once these locations are identified in the image, a virtual RF-source is placed at all the possible cell positions in the image and the received signal is calculated at the external on-body receive antennas. The *a priori* information is used to reduce the computational complexity of the algorithm. The placement of the virtual RF-source could be done at all the cell positions but at a cost of increased computational complexity. The placement of the virtual RF-source is done at the center of P cells, where $P \leq N$ is the number of cells calculated from the *a priori* information.

3) *Measurement and Localization*: In the third step, using the same setup as in the imaging step, the field is recorded by the external M antennas when the in-body RF-source is located at an unknown location inside the actual body. The root-mean-square-error $\tilde{\mathfrak{E}}_j$ between these received field values and the field received by the M antennas when the virtual RF-source is at the P cells is calculated as:

$$\tilde{\mathfrak{E}}_j = \sqrt{\frac{1}{M}\sum_{i=1}^{M} ||\mathbf{R}_{i_{actual}} - \mathbf{R}_{(j,i)_{imaged}}||^2}, \tag{13}$$

where $j = 1$ to P, $\mathbf{R}_{i_{actual}}$ is the received field at the i^{th} receive antenna from the unknown location of the RF-source inside the actual body, and $\mathbf{R}_{(j,i)_{imaged}}$ is the received field at the i^{th} receive antenna when the virtual RF-source is placed at the j^{th} cell in the imaged body. The estimated position is the center of the n^{th} cell such that $\tilde{\mathfrak{E}}_{n\in[1,P]} = \min(\tilde{\mathfrak{E}}_j|_{j=1 \text{ to } P})$. Note that it is not just the field amplitude which is compared but also the phase as $\mathbf{R}_{i_{actual}}$ and $\mathbf{R}_{(j,i)_{imaged}}$ are complex field values.

3 Algorithm Implementation

This section presents the numerical phantoms, simulation setup and other parts in the implementation of the localization algorithm developed in the previous section. The algorithm is implemented for a 2D TM illumination case.

3.1 Numerical Phantoms

The localization algorithm is tested on synthetic field data generated by FDTD simulations [26] of a simple heterogeneous phantom, and a realistic heterogeneous phantom named Billie of a 11 year old female from the virtual family project [27]. The simple phantom (Fig. 1(a)) is a circular cylinder placed in the xy-plane with the electrical properties constant along the z-axis. The radius of the phantom is 13 cm with two more circular cylinders embedded in the

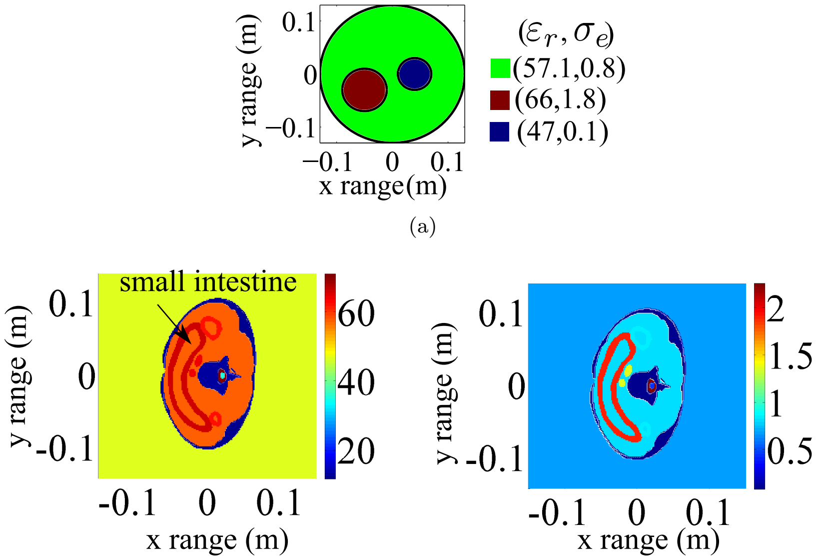

(a)

(b)

(c)

Figure 1: Phantoms with electrical properties: (a) circular phantom where different colors illustrate the different tissues with different electrical properties (b) the relative permittivity in the Billie phantom (c) conductivity in the Billie phantom.

bigger cylinder to make it heterogeneous. The radius of these small cylinders are 4 cm (shown with brown color in Fig. 1(a)) and 3 cm (shown with blue color in Fig. 1(a)). The electrical properties of the 4 cm cylinder are $\varepsilon_r = 66$ and $\sigma_e = 1.8$ S/m representing small intestine and the electrical properties of the 3 cm cylinder is $\varepsilon_r = 47$, close to that of skin at 403.5 MHz. The rest of the phantom has electrical properties of the muscle ($\varepsilon_r = 57.1$ and $\sigma_e = 0.8$ S/m). The electrical properties of the different tissues for Billie are assigned at 403.5 MHz as shown in Fig. 1(b) for ε_r and in Fig. 1(c) for σ_e at the level of the antennas.

3.2 Simulation Setup

The simulations are done in SEMCAD-X [25] which is based on the FDTD method. Electrical properties of muscle tissue is assigned to the external matching medium for the circular phantom. For Billie, electrical properties of skin is assigned to the external medium to match with the outermost tissue. In practical cases, the matching medium can be in the form of a belt or a vest with sufficient thickness where the external antennas can be embedded. However, the actual design of such medium is out of the scope of this paper. For making the imaging problem close to a 2D problem, a 1 mm thick slice of the phantom along the z-axis is considered. The simulation boundary along the z-axis is terminated with a perfect electrical conductor (PEC) boundary condition whereas along the other axes it is terminated by an uni-axial perfectly matched layer (UPML) with the absorbing boundary conditions. A sinusoidal signal at 403.5 MHz from a current source oriented along the z-axis with current amplitude $I_c = 1$ A is considered as a transmitted signal. A 2D field sensor is considered as a receive antenna. The source and the sensor antennas are located around the body at an equal interval of 5° in a circle for the circular phantom, and in an ellipse close to the body for Billie. Hence, the total number of antennas is $M = 72$. One at a time, the current source located at one of the sensor positions is active and the field is recorded by the other 71 sensors. The number of antennas is chosen to be large, and antenna optimization is out of scope of this paper as we here aim for a proof of concept only.

3.3 Microwave Imaging

A recorded scattered field by an object is required for microwave imaging. However, any measurement setups can only record the total field. To get the scattered field, the field values are recorded in the presence and in the absence of the phantom. The field values recorded in the presence of the phantom is the total field whereas the field values recorded in the absence of the phantom but with the matching medium is the total incident field. To these field values, white Gaussian noise is added for making the data more realistic, as following. The noise level is set so that the mean signal-to-noise ratio (SNR) of all sensors is 20 dB when a source is located at the center of the phantom. To calculate noise the noise power, an additional simulation is done by placing the source at the center of the phantom and calculating the field at the receive sensors. The noise power is then calculated as:

$$N_s = \frac{\frac{1}{M}\sum_{i=1}^{M}|\mathbf{R}_i|^2}{10^{SNR/10}} \tag{14}$$

where $\mathbf{R}_i$ is the received field at the i^{th} sensor when the source is placed at the center of the phantom. The additive white Gaussian noise is:

$$n = \sqrt{\frac{N_s}{2}}(r_1 + \mathrm{j}r_2) \tag{15}$$

where r_1 and r_2 are random numbers with the Gaussian distribution. Two different matrices of the noise of size $(M-1) \times M$ are created using (15) and added to the simulated total field and the simulated total incident field to create noisy field values. The scattered field is calculated by subtracting the noisy total incident field from the noisy total field as:

$$\mathbf{e}_{i,j}^{scatt}|_{noisy} = \mathbf{e}_{i,j}^{total}|_{noisy} - \mathbf{e}_{i,j}^{inc}|_{noisy} \tag{16}$$

where $i = 1$ to $M-1 = 71$, $j = 1$ to $M = 72$, $\mathbf{e}^{total}$ is the total field calculated in the presence of the phantom, and $\mathbf{e}^{inc}$ is the total incident field calculated in the absence of the phantom. Using these noisy scattered field values $\mathbf{e}_{i,j}^{scatt}|_{noisy}$, the measured scattered vector $\mathbf{e}^{scatt}$ used in (7) is formed.

For the imaging problem, the circular phantom is discretized in $N = 349$ cells and Billie in $N = 1091$ cells. The initial values of the relative permittivity and the conductivity for all the cells are taken as that of the matching medium ($\varepsilon_r = 57.1$ and $\sigma_e = 0.8$ S/m for circular phantom and $\varepsilon_r = 46.7$ and $\sigma_e = 0.7$ S/m for Billie). The cell size at 403.5 MHz in the exterior medium is $\simeq \lambda_{ext}/8 \times \lambda_{ext}/8$ for the circular phantom, and $\lambda_{ext}/19 \times \lambda_{ext}/19$ for Billie. A finer resolution for Billie is chosen due to several thin tissue layers. Further, the cell size provides a trade-off between the convergence time and the resolution of the image. The objective of the imaging problem is to find ε_r and σ_e for each of the cells such that (7) is satisfied. The incident field is modeled by a 2D current line source having the current amplitude $I_c = 1$ A (same as that used for the simulations) to calculate the total field value in N cells as [29]

$$e_t^i(\mathbf{r}) = -\frac{(\omega\mu_0 I_c)}{4} H_0^{(2)}(k_{ext}|\mathbf{r} - \mathbf{r}_t|), \tag{17}$$

where $\mathbf{r}$ is the coordinates of the center of the cell and $\mathbf{r}_t$ is the coordinates of the transmit antennas for $t = 1$ to 72. The initial value of α_k in (11) is chosen as 100. Convergence for the circular phantom is achieved in the 9th iteration and for the Billie in the 4th iteration. The image obtained is shown in Fig. 2. The values of $\varepsilon_{r_{min}} = 47$, $\varepsilon_{r_{max}} = 66$, $\sigma_{r_{min}} = 0.1$, and $\sigma_{r_{max}} = 1.8$ are used for the circular phantom. For the Billie phantom, $\varepsilon_{r_{min}} = 11.6$, $\varepsilon_{r_{max}} = 71$, $\sigma_{r_{min}} = 0.08$, and $\sigma_{r_{max}} = 1.9$ are used. It can be seen that the relative permittivity of the imaged body is in close agreement with the original phantom. However, there is an error in the conductivity which is higher at the cells having low conductivity. This is explained by the larger magnitude of the real part than the imaginary part of the complex permittivity [30], [31]. Hence, during the estimation, the noise affects the imaginary part (from which σ_e is extracted) to a greater extent than the real part (from which ε_r is extracted) resulting in higher error in the conductivity than the relative permittivity. However, as

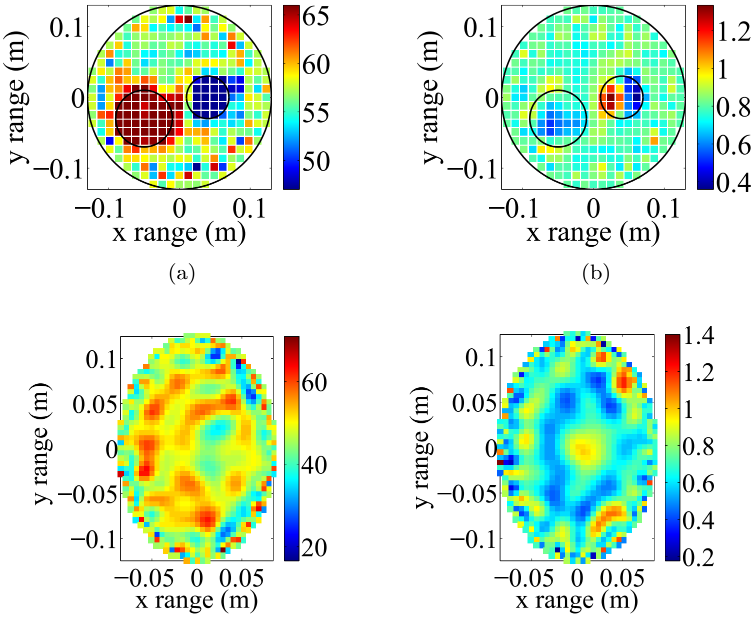

(a) (b) (c) (d)

Figure 2: The imaged body showing (a) the estimated relative permittivity of the circular phantom, and (b) the estimated conductivity (in S/m) of the circular phantom, (c) the estimated relative permittivity of Billie, and (d) the estimated conductivity (in S/m) of Billie. The image has been obtained with $SNR = 20$ dB level of noise.

mentioned earlier, the objective is not to get an enhanced image but to get an approximate estimate of the electrical properties of the body. Moreover, it is indicated in Section 4 that a good localization accuracy is obtained with the estimated electrical properties. Hence, no further investigations were done to improve the conductivity.

Once the image with the approximate electrical properties of each cells is obtained, *a priori* information about the tissues and/or human anatomy can be used for placing the virtual RF-source. For example, *a priori* information about the relative permittivity is used for the simple circular phantom. In this case, we consider that the RF-source can only be located in the tissues with $\varepsilon_r = 66$, which is that of the small intestine. Since there will always be some error in the imaged body for the estimation of the electrical properties, the RF-source should be positioned at all the locations within a permittivity range to provide some margin. We chose this range to be $62 \leq \varepsilon_r \leq 66$. Doing a search for all cells within this range of the relative permittivity, it is found that there are $P = 61$ cells out of 349 cells within it. The imaged body is re-constructed in SEMCAD-X with the exterior medium. The source is then placed at the center of all these 61 cells, one at a time, and the field values are recorded by the 72 sensors located on the body. These recorded field values are stored to be compared with the field values from the RF-source at an unknown location. The importance of the *a priori* information in reducing the computational complexity can be seen as the scan has to be done in only 61 cells out of 349 cells. For Billie, the small intestine has lumen whose electrical properties are close to muscle tissue which occupies most of the portion as seen in Fig. 1(b). Thus, for Billie, the *a priori* information about the human anatomy, that the small intestine will be mostly at the front part of the abdomen, is considered. Hence, the virtual RF-source is placed in about 341 cells at the front portion of the body and the received field values are recorded.

In the circular phantom, the current source is placed at a random position inside the circle with $\varepsilon_r = 66$ and $\sigma_e = 1.8$ S/m and the field values by the 72 external sensors are recorded. In Billie, the current source is placed in the small intestine lumen and the field values are recorded. Noise is added according to (15) to these field values recorded by the external sensors to make the field data noisy and more realistic. The RMSE is calculated between these noisy field values and the field values calculated by the placement of the current source at the 61 cell positions in the reconstructed imaged body for the circular phantom, and at the 341 cell positions for the imaged Billie, for all the receive sensors according to (13). To generate the statistics, the process is repeated for 46 positions of the source inside the circular phantom and 75 positions for Billie phantom. Furthermore, for each of these source positions, the search algorithm is run for 100 realizations of the noisy field data. The complete localization algorithm is summarized in Fig. 3.

4 Results and Discussions

Fig. 4 shows the plots for the magnitude and the phase of the noisy received field by all the on-body sensors from a particular location inside the original phantoms (Fig. 4(a) and Fig. 4(b) for the circular phantom, and Fig. 4(c) and Fig. 4(d) for Billie. The figure also shows the magnitude and the phase of the received field values by the external sensors from the cell having the least RMSE. As can be seen in the figure, the two field values are in good agreement

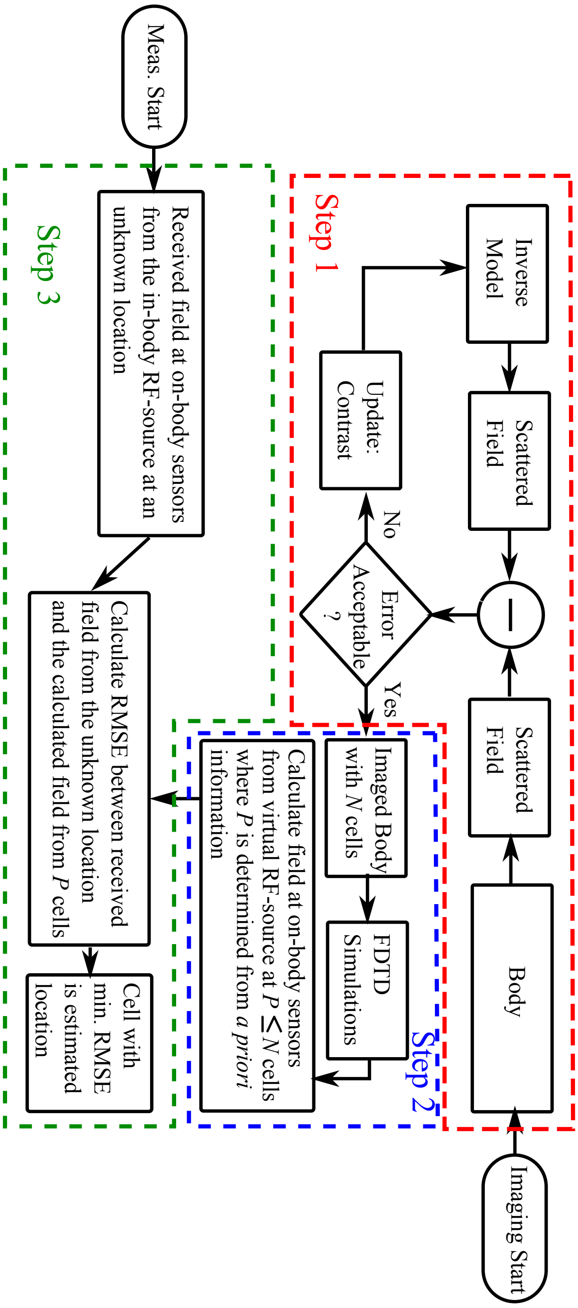

Figure 3: Summary of the localization algorithm. N is the total cells in the reconstructed phantom and P is the cells in which the virtual source is placed after using *a priori* information. Different steps of the algorithm are shown inside the dash boxes.

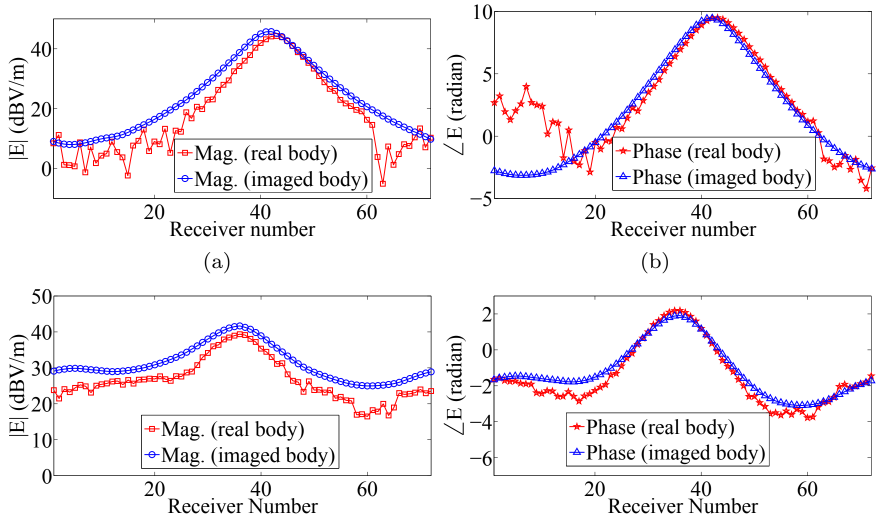

(a) (b)

(c) (d)

Figure 4: Field from the source at the 30th position inside the circular phantom: (a) magnitude and (b) phase. Field from the source at the 40th position inside the Billie phantom: (c) magnitude and (d) phase. The values shown have noise added to them with $SNR = 20$ dB. The magnitude and the phase of the calculated field by the entire on-body sensors from the virtual RF-source located in the cell having minimum RMSE is also shown.

resulting in a low RMSE.

To evaluate the performance of the localization error, the error distance d_{err} for the different locations of the source is calculated as:

$$d_{err} = \sqrt{(x_{true} - \hat{x})^2 + (y_{true} - \hat{y})^2}, \tag{18}$$

where (x_{true}, y_{true}) are the coordinates of the true position of the RF-source, and $(\hat{x}, \hat{y})$ are the coordinates of the estimated position which is the same as the coordinates of the center of the cell with the minimum RMSE $\tilde{\mathcal{E}}$. d_{err} for 46 positions of the RF-source for the circular phantom is shown in Fig. 5(a) and that for 75 positions of the RF-source inside Billie is shown in Fig. 5(b). It can be seen that the maximum error distance is about 1.8 cm for the circular phantom and about 0.8 cm for Billie. The smaller cell size results in a low error for Billie. Furthermore, the root-mean-square of the error distances $(RMS_{d_{err}})$ for all the source positions $Q = 46$ for the circular phantom and $Q = 75$ for

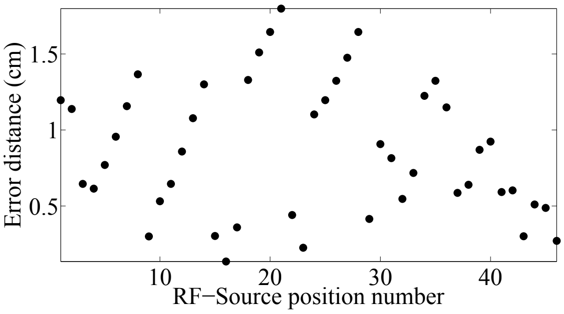

(a)

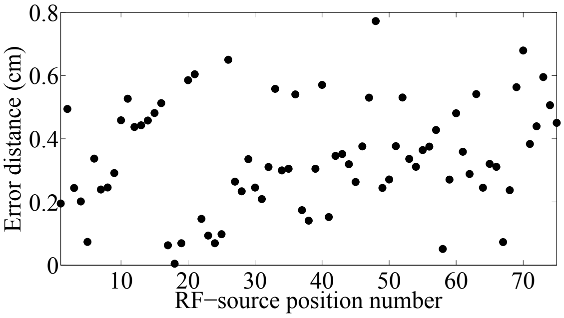

(b)

Figure 5: The error distance between the true position and the estimated position for different source positions for (a) the circular phantom, and (b) Billie.

Billie is also calculated for 100 realization of the noisy data as:

$$RMS_{d_{err}} = \sqrt{\frac{1}{Q}\sum_{i=1}^{Q} {d_{err_i}}^2}. \tag{19}$$

$RMS_{d_{err}}$ for 100 realizations of the noisy data is shown in Fig. 6. The $RMS_{d_{err}}$ lies in the range of 0.93 to 1.01 cm for the circular phantom whereas it is in the range of 0.37 to 0.4 cm for Billie.

The values of $RMS_{d_{err}}$ indicate that the proposed algorithm is capable of localizing the in-body RF-source within millimeter range accuracy even in the presence of noise. Further, smaller cell size increases the accuracy but at the cost of increased computational complexity. Though the algorithm is

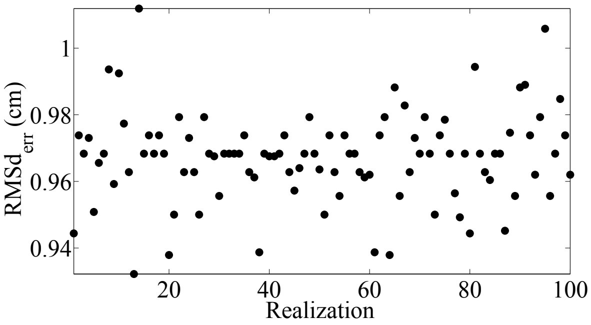

(a)

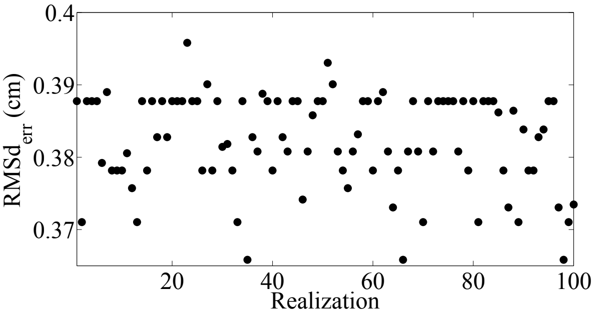

(b)

Figure 6: The root mean square of the distance error for different source positions calculated on 100 realizations of the noisy data. for (a) the circular phantom, and (b) Billie.

implemented for a two dimensional (2D) case, a three dimensional (3D) implementation can be extended by series of a 2D measurement or using a 3D microwave imaging algorithm.

To test the tracking ability of the algorithm, the source is moved inside the Billie intestine at 32 positions along a random path and the field values are recorded by the sensors. To these recorded field values, noise is added and the algorithm is used to estimate the path. The true path and the estimated path is shown in Fig. 7. A good agreement between the true path and the estimated path is obtained indicating the possibility of the algorithm to track the moving capsule.

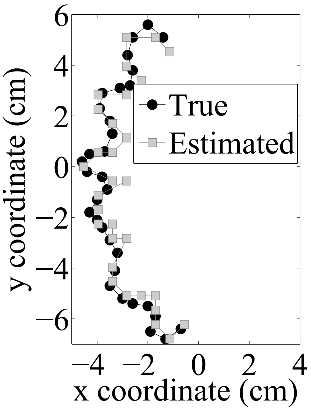

Figure 7: The true path and the estimated path for the source inside the small intestine of Billie.

5 Conclusions

A localization algorithm based on microwave imaging for an in-body RF source at 403.5 MHz was presented. The developed algorithm is a three step process. In the first step the body was imaged to obtain the approximate electrical properties and the distribution of the tissues. In the second step, *a priori* information regarding the electrical properties of the different tissues and/or anatomy of the body was used to find all the possible placement positions of the RF-source. The *a priori* information was used to reduce the computational complexity. A virtual RF-source was then placed at these positions and the electric field recorded by the external sensors was stored to be used in the third step. In the third step, the same setup was used which was used for the imaging. The RMSE between the field received by all the external sensors and the field recorded in the second step was calculated. The position of the RF-source having the least RMSE was the estimated position. The algorithm was tested on the FDTD simulated data of two phantoms, a simple circular phantom and a realistic phantom for the 2D TM polarization after addition of white Gaussian noise and using $SNR = 20$ dB. The error distance between the actual position and the estimated position of the RF-source was found to be within 1.5 cm for the circular phantom, and 0.8 cm for the realistic phantom. Furthermore, the calculated root-mean-square of the error distance for 100 realizations of the noisy field data was within 1 cm for the circular phantom, and 0.4 cm for the realistic phantom. These values of the error distance indicate that the proposed algorithm could be useful for localization of the in-body RF-source in biomedical applications like wireless capsule endoscopy.

The main advantages of the algorithm can be summarized as follows: (a) it does not use a predefined signal propagation model, which is difficult to standardize due to different anatomy and tissue thickness of different people (b) through microwave imaging it eliminates the need for costly MRI scans or ionizing CT-scans to estimate the tissue electrical properties (c) it is not user specific as imaging the body is a part of the algorithm and (d) the same setup used for receiving the signal from the capsule can be used for microwave imaging to determine the electrical properties.

References

[1] T. D. Than, G. Alici, H. Zhou, and Weihua Li, "A Review of Localization Systems for Robotic Endoscopic Capsules," *IEEE Transactions on Biomed. Engg*, vol. 59, no. 9, pp. 2387-2399, Sept. 2012

[2] G. Ciuti, A. Menciassi, and P. Dario, "Capsule Endoscopy: From Current Achievements to Open Challenges," *IEEE Reviews in Biomed. Engg.*, vol. 4, pp. 59-72, 2011

[3] D. Manteuffel, M. Grimm, "Localization of a functional capsule for wireless neuro-endoscopy," in *Proc. Biomed. Wireless Tech., Net., Sensing Sys.*, BioWireleSS, pp. 61-64, Jan. 2012

[4] K. Pahlavan, and et. al., "RF Localization for Wireless Video Capsule Endoscopy", *Int. Journal Wireless Inf. Net.*, Vol. 19, pp. 326-340, 2012

[5] K. Arshak, F. Adepoju, and D. Waldron, "A review and adaptation of methods of object tracking to telemetry capsules," *Int. J. Intell. Comput. Med. Sci. Image Process*, vol. 1, pp. 35-46, 2007

[6] K. Arshak and F. Adepoju, "Adaptive linearized methods for tracking a moving telemetry capsule," in *Proc. IEEE Int. Symp. Ind. Electron*, pp. 2703-2708, 2007

[7] D. Fischer, R. Shreiber , G. Meron, M. Frisch, H. Jacob, A. Glukhovsky, and A. Engel, "Localization of the wireless capsule endoscope in its passage through the GI tract," *Gastrointestinal Endoscopy*, vol. 53, p. AB126, 2001

[8] T. Shah, S. M. Aziz and T. Vaithianathan, "Development of a tracking algorithm for an in-vivo RF capsule prototype," in *Proc. Int. Conf. Electr. Comput. Eng.*, pp. 173-176, 2006

[9] W. Lujia , H. Chao , T. Longqiang , L. Mao, and M. Q. H. Meng, "A novel radio propagation radiation model for location of the capsule in GI tract," *Proc. IEEE Int. Conf. Rob. Biomimetics*, pp. 2332-2337, 2009

[10] W. Lujia , L. Li , H. Chao, and M. Q. H. Meng, "A novel RF-based propagation model with tissue absorption for location of the GI tract", *Proc. Annu. Int. Conf. IEEE Eng. Med. Biol. Soc.*, pp. 654-657, 2010

[11] W. Yi, F. Ruijun, Y. Yunxing, U. Khan, and K. Pahlavan, "Performance bounds for RF positioning of endoscopy camera capsules," *Proc. IEEE Top. Conf. Biomed. Wireless Technol.*, Netw., Sens. Syst., pp. 71-74, 2011

[12] H. Jinlong, et. al., "Design and implementation of a high resolution localization system for In-vivo capsule endoscopy", in *Proc. 8th Int. conf. Dependable Auton. Secure Comput.*, pp. 209-214, 2009

[13] Z. Le , Z. Yongxin , M. Tingting , H. Jinlong, and H. Hao, "Design of 3D positioning algorithm based on RFID receiver array for in vivo microrobot," in *Proc. 8th IEEE Int. Conf. Dependable, Auton. Secure Comput.*, pp. 749-753, 2009

[14] L. Zhang, Y. Zhu, T. Mo, J. Hou, and G. Rong, "Design and implementation of 3D positioning algorithms based on RF signal radiation patterns for in vivo micro-robot," in *Proc. Int. Conf. Body Sens. Netw.*, pp. 255-260, 2010

[15] M. Pourhomayoun, Z. Jin, and M. Fowler, "Accurate Localization of In-Body Medical Implants Based on Spatial Sparsity," *IEEE Trans. of Biomed. Engg.*, Accepted, 2013

[16] R. Chandra, A. Johansson, and F. Tufvesson, "Localization of an RF source inside the Human body for Wireless Capsule Endoscopy," in *Proc. 8th Int. Conf. Body Area Net., BodyNets*, pp. 48-54, Sept. 2013,

[17] N. Joachimowicz, C. Pichot, J-P. Hugonin, "Inverse scattering: an iterative numerical method for electromagnetic imaging," *IEEE Trans. Antennas Propagat.*, vol. 39, no. 12, pp. 1742-1753, Dec. 1991

[18] J.J. Mallorqui, N. Joachimowicz, A. Broquetas, and J. Bolomey, "Quantitative images of large biological bodies in microwave tomography by using numerical and real data," *Electronics Letters*, vol. 32, no. 23, pp. 2138-2140, 1996

[19] A. Abubakar, P.M. van den Berg, and J.J Mallorqui, “Imaging of biomedical data using a multiplicative regularized contrast source inversion method,” *IEEE Trans. Microwave Theory and Techniques*, vol. 50, no. 7, pp. 1761-1771, Jul. 2002

[20] S.Y. Semenov, R.H. Svenson, A.E. Bulyshev, and et. al., “Three-dimensional microwave tomography: initial experimental imaging of animals,” *IEEE Trans. Biomed. Engg.*, vol. 49, no. 1, pp. 55-63, Jan. 2002

[21] P. Mojabi, and J. LoVetri, “Microwave Biomedical Imaging Using the Multiplicative Regularized Gauss-Newton Inversion,” *IEEE Antennas Wireless Propag. Lett.*, vol. 8, pp. 645-648, 2009

[22] C. Gilmore, Am. Zakaria, S. Pistorius, and J. Lo Vetri, “Microwave Imaging of Human Forearms: Pilot Study and Image Enhancement,” *Int. Jour. Biomed. Imaging*, vol. 2013, Article ID 673027, 2013

[23] A. Franchois and C. Pichot, “Microwave imaging-complex permittivity reconstruction with a Levenberg-Marquardt method,” *IEEE Trans. Antennas Propagat.*, vol. 45, no. 2, pp. 203-215, Feb. 1997

[24] J. Richmond, “Scattering by a dielectric cylinder of arbitrary cross section shape,” *IEEE Trans. Antennas Propagat.*, vol. 13, no. 3, pp. 334-341, May 1965

[25] Schmid & Partner Engineering AG, Zeughausstrasse 43, 8004 Zurich Switzerland

[26] K. Yee, “Numerical solution of initial boundary value problems involving Maxwell’s equations in isotropic media,” *IEEE Trans. Antennas Propagat.*, vol. 14, no. 3, pp. 302-307, May 1966

[27] A. Christ et al., “The Virtual Family Development of anatomical CAD models of two adults and two children for dosimetric simulations”, *Phy. Med. Bio.*, vol.55, no.2, pp. N23-N38, Jan. 2010

[28] A. Abubakar, P.M. van den Berg, and S. Y. Semenov, “A robust iterative method for Born inversion,” *IEEE Trans. Geoscience Remote Sens.*, vol. 42, no. 2, pp. 342-354, Feb. 2004

[29] R. F. Harrington, *Field Computation by Moment Methods*, New York, MacMillan, 1968.

[30] P. M Meaney, N. K Yagnamurthy, and K. D Paulsen, “Pre-scaled two-parameter Gauss Newton image reconstruction to reduce property recovery imbalance,” *Phys. Med. Biol.*, vol. 47, pp. 1101-1119, 2002

[31] P. Mojabi, and J. LoVetri, "A Prescaled Multiplicative Regularized Gauss-Newton Inversion," *IEEE Trans. on Antennas Propagat.*, vol. 59, no. 8, pp. 2954,2963, Aug. 2011